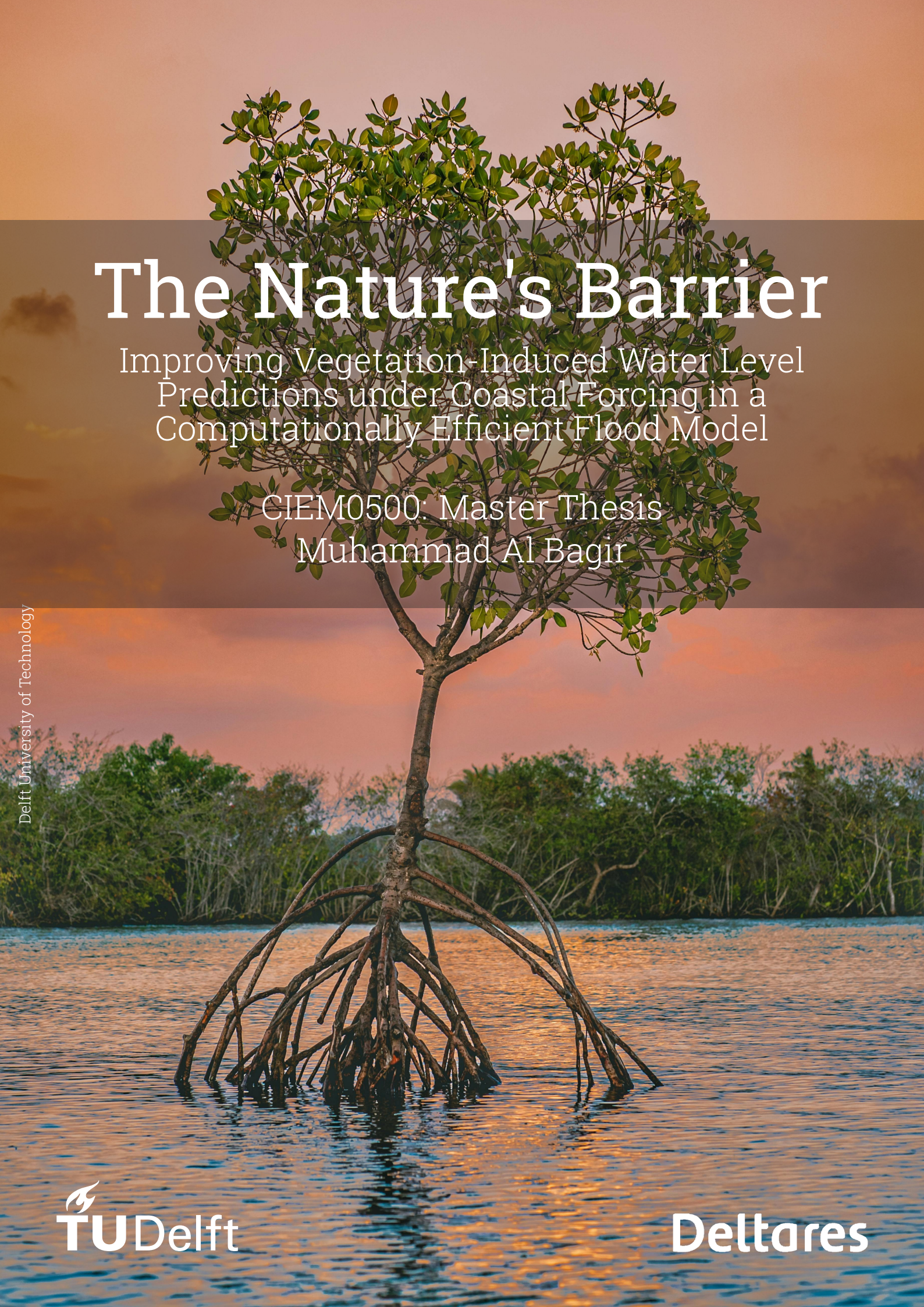

The Nature's Barrier

Improving Vegetation-Induced Water Level Predictions under Coastal Forcing in a Computationally Efficient Flood Model

CIEM0500: Master Thesis

Muhammad Al Bagir

Delft University of Technology

TU Delft

Deltares

The Nature's Barrier

Improving Vegetation-Induced Water Level Predictions under Coastal Forcing in a Computationally Efficient Flood Model

by

Muhammad Al Bagir

Student number

5915775

Responsible Supervisor:	Dr. Bregje van Wesenbeeck
Supervisor:	Prof.dr.ir. A.J.H.M. Reniers
Supervisor:	Ir. Vincent van Zelst
Date:	9 September 2025
Faculty:	Civil Engineering and Geosciences, Delft

Cover: Photo by Nandhu Kumar: https://www.pexels.com/photo/single-tree-on-backwater-sunset-background-13790858/

Style: TU Delft Report Style, with modifications by Daan Zwaneveld

TU Delft Deltares

Acknowledgment

"Let yourself be silently drawn by the strange pull of what you really love.
It will not lead you astray." — Rumi

It is never easy to make big decisions in life. One of mine was to pursue a master's degree in Hydraulic Engineering abroad. Not because it was unconvincing — quite the opposite. I loved it from the start. What made it hard was the fact that I had to pivot and leave behind five years of work in the structural–geotechnical field. My only reason for taking this risk was simple: I felt drawn to this discipline. Not many people understood this seemingly absurd reasoning. I was simply curious — curious about how waves are generated, or why sand grains differ in size from one place to another. My curiosity about nature locked me in, that was all. The Rumi quote above expresses exactly what I believe. With little prior knowledge in this field, I took the leap. And with this thesis, I can finally say that I have completed one of the most amazing chapters of my life.

I am deeply grateful for the unwavering support of my family, who encouraged me to follow what I love. My wife, Amirah, has been there through every up and down of this chapter, and I was blessed to gain another cheerleader — my daughter, Syifa — who was born while I was drafting this thesis idea. This journey kept us physically apart for a while, but I believe we were always together at heart. My parents, Mama and Abah, and my sister, Kakak, have also been there for me, supporting every decision I made and sharing weekly calls full of news and warmth. This thesis is not only an academic milestone but also a testament to my pursuit of curiosity, supported perfectly by my family. The freedom to seek knowledge is a privilege, and I am grateful to experience it here at TU Delft.

This thesis would not have been possible without the excellent guidance of my supervisory team. Ir. Vincent van Zelst, my day-to-day mentor from day one, patiently guided me in exploring my curiosity and gave me the opportunity to intern at Deltares. Bridging from a research internship to a graduation internship at Deltares, I initially brought quite an unusual idea on compound flooding and mangroves. After countless rounds of sharpening, we arrived at the idea of improving the model. Dr. Bregje van Wesenbeeck, who kindly agreed to supervise me from the very beginning, continuously challenged me to deliver this research in a proper and meaningful way. Without her guidance, I would not have reached this point. Prof. Ad Reniers always brought fresh insights in our meetings, patiently revisiting fundamentals with me, and generously sharing his expertise in wave-related modelling. I would also like to thank Dr. Tim Leijnse, though not formally part of the team, for his great help in implementing and understanding the `SFINCS-SnapWave` model, and Dr. Arnold van Rooijen, for sharing flume experiment data and `XBeach` model files.

Finally, I express my sincere gratitude to the Indonesia Endowment Fund for Education (LPDP) for sponsoring my studies. I am also thankful to my Indonesian colleagues, who stuck together through every high and low, supporting one another while far from home. I am grateful to have shared this experience with all of you. I hope we all achieve success in our own paths and contribute to a greater mission in Indonesia.

Through this thesis, I proudly claim that I chose the harder path — and it was worth every effort. For the first time in my life, I have done what I truly love, and I hope this journey continues into the future.

Muhammad Al Bagir
Delft, September 2025

Abstract

Coastal flooding is often driven by the combined action of storm surges and waves, which co-occur along more than half of the world's coastlines. Vegetation such as mangroves and salt marshes provides natural protection in these events by attenuating surges, dissipating wave energy, and reducing wave setup. While advanced process-based models (e.g. `XBeach`) can capture such interactions, their high computational demands limit their use for large-scale or scenario-based simulations. In contrast, reduced-physics models (e.g. `SFINCS-SnapWave`) enable efficient simulations under combined coastal forcing, but their ability to represent vegetation–hydrodynamic interactions remains limited. This thesis improves the `SFINCS-SnapWave` model by incorporating vegetation-induced drag due to nonlinear wave shape ($F_{v,w}$). Model performance was evaluated against laboratory flume data and benchmarked with the process-based `XBeach` surfbeat model (`XBeach-SB`). Results show that adding $F_{v,w}$ substantially improves predictions of mean water levels in vegetated foreshores, reducing setup errors at the landward end by an average of a factor of six compared to the baseline model across all scenarios. This improvement arises because $F_{v,w}$ represents a vegetation drag component that counteracts wave-breaking forcing, thereby correcting the excessive setup otherwise produced by dissipation-only formulations. Significant wave height predictions remained accurate, and computational efficiency was preserved due to the empirical wave-shape approach. These findings underline the importance of vegetation in wave-driven flooding. Further improvements—such as incorporating mean-flow vegetation drag and validating against field-scale data—are recommended to extend model reliability. With these extensions, the enhanced `SFINCS-SnapWave` has the potential to serve as a robust and efficient tool for simulating multi-driver flooding in vegetated coasts.

Keywords: coastal flooding, compound events, vegetation, mangroves, wave setup, flood modelling, `SFINCS`, `SnapWave`, `XBeach-SB`

Contents

1

Introduction

1.1. Background

Over half of the world's population currently resides within 100 km of the coastline, and this population is expected to grow further. However, these coastal areas are particularly vulnerable to flooding (Sebastian 2022). It is estimated that 0.8- 1.1 million people are impacted by coastal flooding globally per year, which has a considerable impact on society (Sanne Muis et al. 2016). In economic terms, global average annual losses were estimated at $6 billion in 2005, and it was projected that the figure could rise to $52 billion by 2050 solely due to socio-economic changes (Hallegatte et al. 2013).

Coastal flooding can be driven by coastal drivers (i.e., storm surges, waves, tides) as well as inland drivers (i.e., river discharge and rainfall). When these drivers occur simultaneously, their combined effects may exacerbate flood severity, a phenomenon commonly referred to as compound flooding. Such co-occurrence often results from shared physical forcing mechanisms, such as synoptic weather systems like tropical cyclones. Tropical cyclones can generate high storm surges and waves, together with extreme rainfall that increases river discharge (Couasnon et al. 2020). This physical dependency raises the likelihood of multiple extremes occurring at the same time, thereby contributing to compound flooding.

Focusing on the coastal driver contribution, extreme water levels depend not only on the intensity of forcing but also on the local coastal settings. In regions not influenced by river discharge, extremes are primarily driven by coastal processes (i.e., tides, storm surges, and wave setup). Storm surges elevate water levels through reduced atmospheric pressure and wind-driven piling, in addition to the regular tidal oscillation. Waves can further contribute by inducing a mean water level increase, known as wave setup. While open coasts are often more exposed to incoming waves (Marcos et al. 2019), this is not always the case; many mangrove coasts are associated with low wave energy, but wave effects can become more prominent during tropical cyclones.

Coastal vegetation, such as mangroves and tidal marshes, serves as a natural defence against coastal flood drivers by attenuating waves and storm surges. Wave energy is reduced through increased drag and bottom friction (Temmerman et al. 2023). Vegetation can also lower wave setup—or even cause setdown—and modify infragravity (IG) wave propagation (van Rooijen et al. 2016). In addition, vegetation influences storm surge dynamics: as surges propagate, vegetation and elevated bed levels exert drag on the flow, slowing propagation and reducing peak water levels both within and behind vegetated areas (Temmerman et al. 2023).

Despite the known mitigation role of vegetation in coastal flooding, most studies often focus on its effects on a single flood driver (i.e wave or storm surge-only). However, in reality, there is a clear spatial overlap between mangrove ecosystems and tropical cyclone tracks (Figure 1.1), which highlights the relevance of these ecosystems in regions exposed to multiple flood drivers. Incorporating vegetation effects into multi-driver flooding simulations is therefore an important step toward understanding and rightly accounting for the protective role of natural ecosystems in such events.

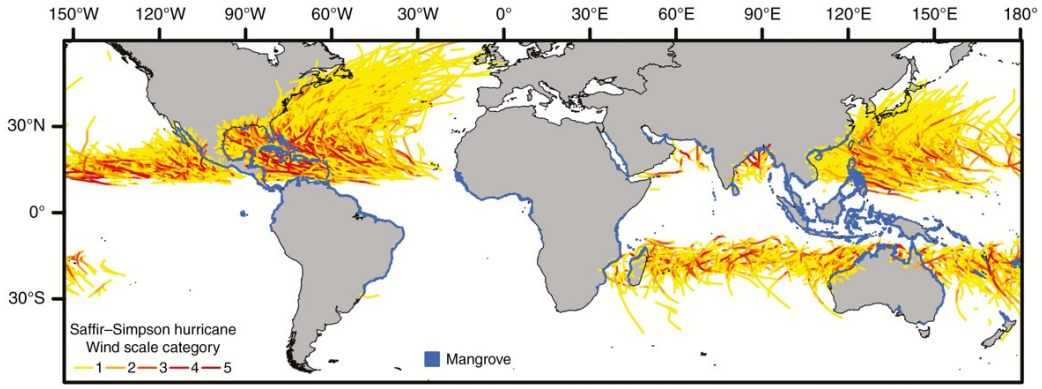

Figure 1.1: Global distribution of tropical cyclone storm tracks categorised by the Saffir–Simpson scale Knapp et al. (2010). Mangrove distribution is shown in blue shading (Giri et al. 2010). Figure originally from Krauss and Osland (2020).

1.2. Problem statement

To date, limited studies have considered the influence of coastal vegetation under the combined action of multiple flood drivers. While some research has explored the role of mangroves in surge–river compound flooding (Pelckmans et al. 2024), studies addressing co-occurring coastal-driven components—specifically storm surge and waves—remain scarce. However, such events are relatively common: Marcos et al. (2019) found that extreme waves and storm surges tend to co-occur along 55% of the global coastline. This highlights the need to assess the flood mitigation potential of vegetation under combined coastal forcing.

Vegetation provides coastal flood mitigation benefits by attenuating storm surges, dissipating wave energy, and reducing wave setup (Temmerman et al. 2023; van Rooijen et al. 2016). To adequately reproduce these processes, flood models should include the combined effects of multiple flood drivers and vegetation interactions. Advanced models such as `XBeach` can represent detailed hydrodynamic and vegetation processes; however, their high computational demands make them less suitable for large-scale or scenario-based simulations covering domains of hundreds to thousands of kilometres.

In contrast, reduced-physics models such as `SFINCS` offer the computational efficiency needed for large-scale flood simulations involving multiple flood drivers (T. Leijnse et al. 2021). However, vegetation effects in `SFINCS` are typically represented using a simplified bed roughness formulations, which may not adequately capture key vegetation characteristics and associated drag forces. To include wave-induced processes, `SFINCS` could be coupled with a wave-resolving module, such as `SnapWave` (D. Roelvink et al. 2025). While the coupled `SFINCS-SnapWave` model enables efficient large-scale simulations under combined coastal forcing, its ability to represent vegetation–hydrodynamic interactions under these conditions has not been thoroughly evaluated.

Therefore, this study explores how well a reduced-physics flood model, such as `SFINCS-SnapWave`, captures vegetation-influenced water levels under coastal-driven forcing. By evaluating its current capabilities and implementing improvements, this research aims to enhance the water level prediction by incorporating key vegetation processes in the model.

1.3. Research objectives

This study aims to improve the accuracy of a computationally efficient flood model by incorporating essential vegetation effects, thereby enhancing predictions of water levels under coastal forcing. To achieve this, the following objectives are formulated:

1. Evaluate the capability and limitations of the model in predicting vegetation-influenced water levels under coastal forcing.
2. Implement and validate improvements to incorporate key vegetation-related physical processes while maintaining computational efficiency.

1.4. Research questions

To achieve the objectives, several key questions will guide the research:

Main Research Question:

To what extent can vegetation-hydrodynamic interactions be accurately represented in a computationally efficient flood model under coastal forcing?

To address this main question, five sub-research questions are formulated:

1. What are the essential physical processes in vegetation–hydrodynamic interactions that influence water level predictions?
2. How well does the initial model reproduce wave transformation and water levels in vegetated conditions?
3. Which limitations in vegetation representation affect the accuracy of the model prediction on water levels?
4. To what extent does the improved model enhance the accuracy of water level and wave transformation predictions?
5. What is the impact of the model improvements on computational time?

1.5. Scope

This research consists of two main components: (i) model evaluation and (ii) model improvement. The model used to perform this study is the coupled `SFINCS-SnapWave` model.

First, the initial model is evaluated to assess its ability to represent vegetation-induced hydrodynamic processes. The evaluation focuses on key variables, including significant wave height, infragravity (IG) wave, and water levels. Second, the model is improved to better capture the influence of vegetation, particularly by enhancing the representation of vegetation-induced forces. Both evaluation and improvement steps are performed by validating the model results against laboratory measurements and a benchmark model.

Several simplifications and assumptions are adopted to keep focus on hydrodynamics. The simulations are conducted under morphostatic conditions (i.e., fixed bed levels), and vegetation is represented as rigid cylinders. Vegetation growth, flexibility, and sediment–vegetation feedbacks are not included. Additionally, the scope is limited to laboratory-scale validation, and no field-scale application is performed in this study.

1.6. Report Outline

This thesis is structured comprising literature review, methods, results, discussion, and conclusion with recommendations. Table 1.1 summarises the structure and provides a brief chapter description.

Chapter	Title	Description
Chapter 2	Literature review	Overview of multi-driver flooding and vegetation relevance, global mangrove characteristics, vegetation–hydrodynamic interactions, and hydrodynamic models with vegetation effects.
Chapter 3	Methods	Present the model selection and approach of the study in order to achieve the objectives.
Chapter 4	Model evaluation and improvement	Present the model evaluation and improvement results by validating them with laboratory measurement data and a benchmark model.
Chapter 5	Discussion	Discuss the limitations and uncertainties of the improved model, as well as assess real-world applicability.
Chapter 6	Conclusion and recommendations	Summarises the main findings and provides recommendations for future research.

Table 1.1: Thesis reporting structure

2

Literature review

This chapter begins by discussing the relevance of multi-driver flooding and coastal vegetation, using a specific example of the mangrove ecosystem. Next, the global mangrove characteristics are described, including their distribution and classification. Then, the influence of vegetation on individual flood drivers, focusing on wave height attenuation, storm surge reduction, and wave setup modification, is explained. Lastly, the chapter then reviews approaches for hydrodynamic–vegetation interactions in computational models and closes with a comparison between `XBeach-SB` and `SFINCS-SnapWave` in implementing vegetation effects.

2.1. Multi-driver flooding and coastal vegetation influence

Coastal flooding can arise from multiple flood drivers, including coastal drivers (storm surges, wave action, and high tides) and inland drivers (river discharge, rainfall). When these drivers co-occur, often called compound flooding, their combined impact can be more severe than the sum of individual effects (Gori et al. 2020; Radfar et al. 2024). For example, the interactions between the coastal drive and inland flood drivers can slow down water drainage into the sea, leading to a piling up of water levels along the coast (Bevacqua et al. 2019). Such events are often triggered by the same meteorological system, such as a tropical cyclone, which can produce both intense rainfall and extreme sea levels. Although there are various definitions of compound flooding (Green et al. 2025), this study adopts the commonly used definition involving the co-occurrence of coastal and inland flood drivers. Figure 2.1 shows the illustration of compound flooding events.

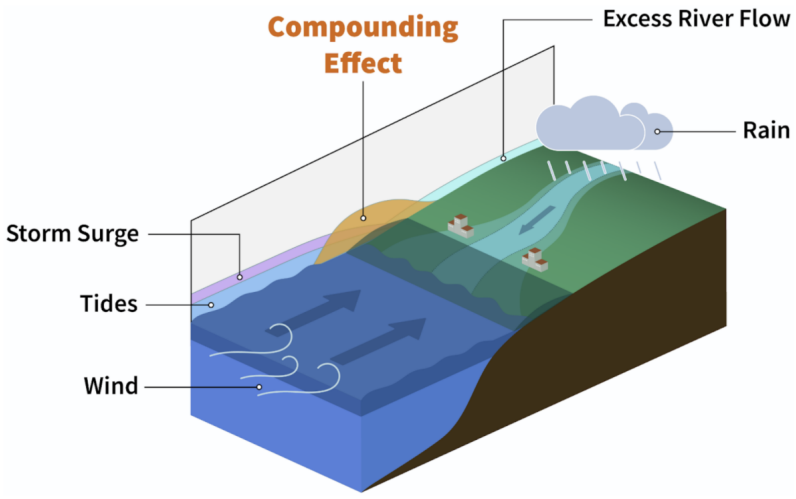

Figure 2.1: Compound flooding due to inland flood drivers (rain and river discharge) and coastal flood drivers (storm surge, wind wave, and tides). Picture adapted from Cascadia CoPes Hub (2025).

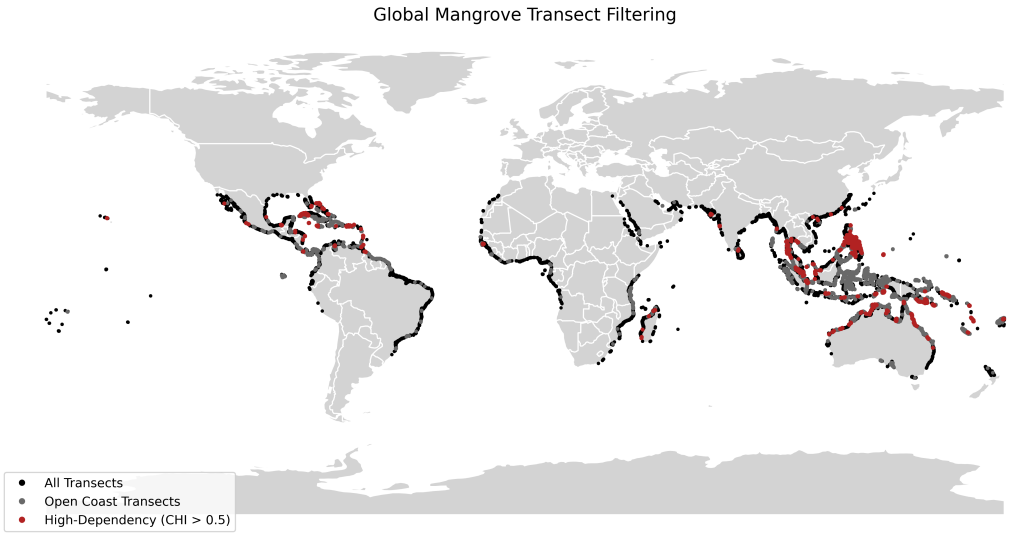

Figure 2.2: Map showing the spatial filtering steps for selecting representative mangrove transects. The black dots indicate all transects in the global dataset. Grey dots represent transects located along open coast typologies, and red dots indicate transects with a high wave–surge dependency ($\chi > 0.5$). This layered visualisation demonstrates the progressive refinement toward physically relevant locations for wave-surge multi-driver flood analysis.

The mechanism of compound flooding and drivers' dominance depends strongly on the coastal setting. In estuaries and deltas, inland drivers such as river discharge often dominate. In contrast, open-coast environments, with limited or no river influence, are more strongly governed by coastal drivers such as tides, storm surges, and wave action. Local factors such as topography, bathymetry, morphology, and land use can further modulate this dominance and severity of the flooding (Green et al. 2025).

Natural ecosystems, particularly coastal vegetation, form important local factors influencing flooding processes. Vegetation such as mangroves can increase flow resistance, dissipate wave energy, and attenuate storm surges (Temmerman et al. 2023). While these effects on individual flood drivers are widely explored, their role in compound flooding events or even multi-driver coastal flooding—particularly the combined effects of waves and storm surges—remains less explored. One reason is that hydrodynamic models often simplify vegetation effects (e.g., as spatially varying bed roughness) to keep computational costs low (Radfar et al. 2024). Identifying where such multi-driver coastal flooding coincides with vegetated regions is therefore important toward understanding their protective role.

Potential regions of multi-driver coastal flooding in vegetated settings can be identified using available global datasets. For example, offshore hydrodynamic conditions (H_s, T_p, and storm tide) along global mangrove coasts are provided by van Zelst et al. (2021). These transects can be further refined based on mangrove typology (Worthington et al. 2020) and on wave–surge extreme dependency (Marcos et al. 2019). Filtering for open-coast transects relevant to wave–surge flooding, and retaining only those with high dependency between extremes ($\chi > 0.5$), highlights the global hotspots where wave–surge multi-driver flooding is most relevant in mangrove regions (Figure 2.2).

Real-world cases

Compound flooding has been observed in several real-world situations. In southern and eastern Africa, countries such as South Africa, Mozambique, and Madagascar experience compound flooding due to tropical cyclones, particularly during the austral summer. Similarly, in Asia, compound flooding tends to be most frequent in the south, southeast, and east regions, such as India and Bangladesh (Bay of Bengal), Indonesia (North Natuna Sea), and China. Co-occurring extremes are most prominent in the wet monsoon season in East Asia, while in general, most compound flooding in Asia occurs from summer to late autumn, corresponding with tropical cyclone seasonality (Green et al. 2025).

The previously mentioned global regions, such as some parts of Africa and Asia, which are prone to tropical cyclones and compound flooding, also possess abundant natural ecosystems, such as mangrove forests, that can be utilised for flood mitigation. Mangroves are well known for providing natural

flood protection and can directly influence the physical processes of flooding, by attenuating wave and surge (Temmerman et al. 2023). Furthermore, many regions worldwide share similar conditions: high exposure to tropical cyclones, which can lead to compound flooding, and the presence of mangrove belts as natural defences. As shown in Figure 1.1, mangrove belts frequently overlap with areas of intense tropical cyclone activity, positioning them as valuable natural assets in regions vulnerable to compound flooding.

However, most studies on vegetation–hydrodynamic interactions focus on single flood drivers (e.g., waves or surges) rather than their combined action in multi-driver or compound flooding events (Radfar et al. 2024). This gap underscores the importance of advancing research on how vegetation influences flooding under multiple coastal drivers, and ultimately in compound flooding, to fully capture the protective role of natural ecosystems.

2.2. Global mangrove characteristics

This section discusses the global distribution of mangroves, the ecosystems in which they are found, and the general classification of mangrove species, including the typical bed slopes where mangroves thrive. Mangroves are highly relevant to this study's simulation scope, in which vegetation is represented as rigid structures. Understanding global mangrove characteristics is crucial as the basis for examining the vegetation-hydrodynamic interaction that leads to flooding.

2.2.1. Mangrove distribution and ecosystem

Mangroves are coastal habitats found in tropical and subtropical regions, in contrast to salt marshes, which typically occur in temperate climate zones along mid-latitude coasts. Mangroves are primarily distributed between 25° north and south latitude, with the largest extent located in Asia (42%), followed by Africa (20%), North and Central America (15%), Oceania (12%), and South America (11%). Indonesia has the largest mangrove area in the world, accounting for about 22% of the global total, followed by Australia and Brazil, each with around 7% (Giri et al. 2011). Figure 2.3 shows the global distribution of mangroves around the world.

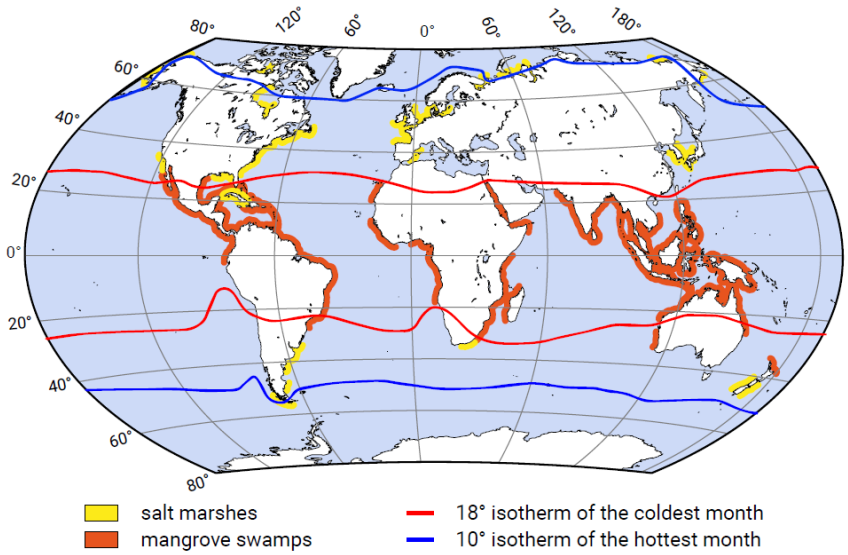

Figure 2.3: Global distribution of mangrove swamps and salt marshes (Bosboom and Stive 2023).

Mangroves can grow in certain abiotic conditions, and one of them is that the vegetation requires calm and silty conditions. Those variables are closely related - the silty conditions can only be established in a calm, sheltered area that allows the finer particles to settle. In contrast, the vegetation finds it difficult to colonise areas with high wave energy (Bosboom and Stive 2023; Kathiresan 2021). As mangroves do occur in low day-to-day wave energy environments, they are typically found in a variety of coastal settings, such as deltas, estuarine deltas, estuaries, estuarine lagoons, lagoons, and coastal

fringes. The deltas and estuaries that were formed by the deposition of fine sediment from the river mouth could be colonised by mangroves. In this coastal setting, the coastal environment is often tide-dominated, where mangroves are often frequently formed by tidal washing and grow on over-washed small islands in front of the delta. Further upstream, riverine mangrove forests can be found along rivers and creeks. They can get flooded daily by floods and are influenced by a large amount of freshwater and nutrients. Mangroves can also thrive along coastal fringes with low wave energy. This type of mangrove is sensitive to erosion and exposure to waves and tides. Lastly, lagoons typically formed behind barrier islands also allow less wave action in the area and could be a suitable place for mangrove growth (Kathiresan 2021). Moreover, Worthington et al. (2020) present the global mangrove biophysical typology based on the 2016 extent, which is distributed as follows: Deltaic (40.5%), estuarine (27.5%), open coast (21%), and lagoon (11%). Figure 2.4 illustrates the typical coastal settings of mangrove forests and their detailed types.

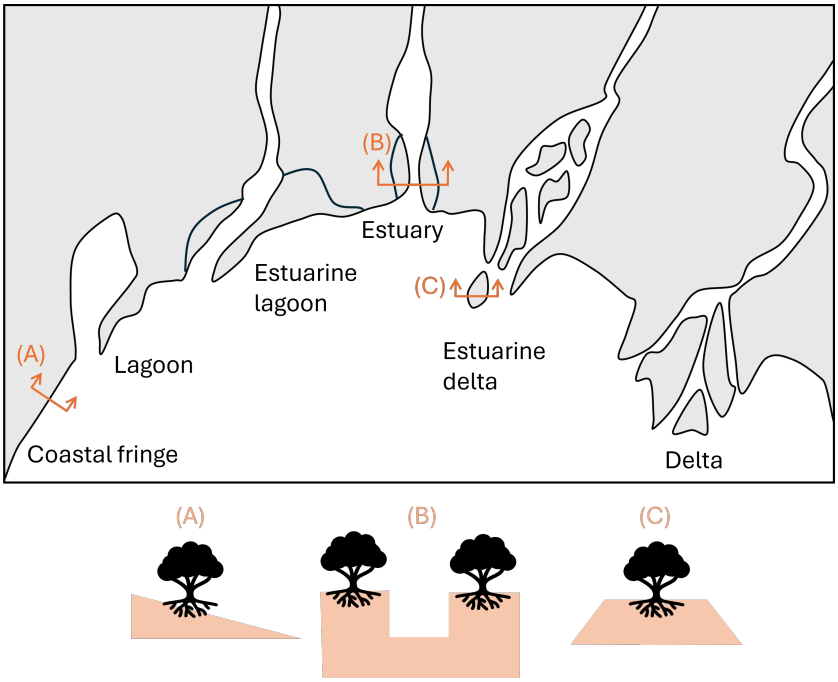

Figure 2.4: Coastal settings of mangrove forests and functional types of mangrove forests. Cross section (A): Fringe ecosystem, (B): Riverine ecosystem, and (C): Over-wash ecosystem. Picture adapted from Kathiresan (2021).

2.2.2. Mangrove classification and zonation

Global mangrove habitats are highly diverse. The Eastern Hemisphere (Indo-West Pacific region), which contains 57% of the global mangrove area, is rich in biodiversity with 63 species. In contrast, the Western Hemisphere (Atlantic East Pacific region) holds 43% of the global mangrove area but has only 19 species (Kathiresan 2021). Here, we focus only on two common mangrove species groups based on their root structure: red mangroves (i.e. *Rhizophora sp.*) and black mangroves (i.e. *Avicennia sp. and Sonneratia Alba sp.*) (Romañach et al. 2018). This selection is based on the nature of the physical obstacles these root systems present to incoming waves.

Mangrove classification

Red mangroves. Red mangrove species (i.e. *Rhizophora sp.*) have distinctive prop roots that form a dense network above the ground. These roots offer considerable resistance to water flow, especially in shallow water. Above the root zone, the tree trunks present fewer obstacles, allowing waves to pass more easily. As a result, wave attenuation is highest at shallow depths where roots are concentrated, and decreases in deeper water where the wave interacts more with a trunk and less with the roots (McIvor et al. 2012).

Black mangroves. Black mangrove species (i.e. *Avicennia sp. and Sonneratia Alba sp.*) possess pneumatophores, which are the narrow roots that project vertically from the ground to support gas exchange. These roots typically reach heights 20 to 30 cm. Like prop roots of *Rhizophora sp.*, these aerial roots function as physical obstacles to water movement at shallow depths, enhancing wave attenuation. As water levels increased and rose above the root structures, the attenuation effect decreased until wave interaction with branches and leaves became more substantial (McIvor et al. 2012). Figure 2.5 below shows the different root structures of these species.

Figure 2.5: Root structures of different mangrove species. Left: Prop roots of red mangroves *(Rhizophora sp.)*, which form dense networks above the substrate and cause strong wave attenuation at shallow depths. Right: Pneumatophores of black mangroves *(Sonneratia Alba sp.)*, which also act as obstacles to wave motion at low water levels. Picture from Wikipedia contributors (2024).

Mangroves zonation

Mangroves are salt-resistant vegetation which thrives in the intertidal zones, typically between Mean Sea Level (MSL) and Mean High Water Spring (MHWS). Seaward of mangroves, mudflats are commonly found, usually with gentle slopes of 1:1000. Landward, the slope typically becomes steeper where mangroves are found. They exhibit characteristic zonation, with different species occupying distinct elevation ranges (Bosboom and Stive 2023). Figure 2.6 illustrates a schematic cross-section of a typical mangrove forest, showing species zonation across elevation gradients (Bosboom and Stive 2023). Comparable patterns, with *Avicennia/Sonneratia*, *Excoecaria*, and *Ceriops* occurring at different tidal elevations, have also been documented by J. C. Ellison (2000).

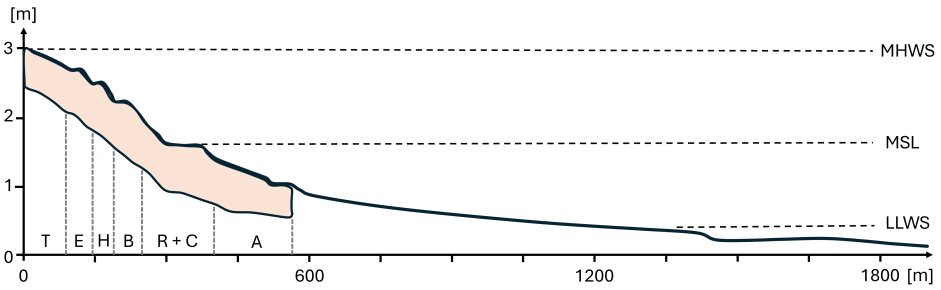

Figure 2.6: Schematic cross-section of a typical mangrove forest illustrating species zonation along an elevation gradient. Species abbreviations: (T): Thespesia, (E): Excoecaria, (H): Heritiera, (B): Bruguiera, (R): Rhizophora, (C): Ceriops, (A): Avicennia. Tidal datums: (MHWS): Mean High Water Spring, (MSL): Mean Sea Level, (LLWS): Lowest Low Water Spring. Picture adapted from Bosboom and Stive (2023).

Local factors, such as flood regimes, tidal amplitude, sediment composition, salinity, and nutrient availability, jointly shape mangrove distribution, often in interdependent ways. Spier et al. (2016) study the impact of flood regime on the distribution of mangrove species and salt marshes in the subtropical coast of Brazil, called Paranaguá Estuarine Complex (PEC). In this particular case study, it is presented that the flood regime is the most important factor in the distribution of mangrove ecosystems. Mangrove-associated species were subject to a similar pattern of submergence and emergence, despite the variability in tide amplitude, salinity, and sediment composition. It is found that mangroves grow between

the mean sea level and slightly above the mean high tide, so they are flooded less than 50% of the time on average. Limited flooding is important because too much water reduces oxygen around the roots, which harms mangrove growth and functions. If tidal flows are altered, such as by dikes, mangroves can become stressed. Therefore, effective management and restoration should keep or restore the natural flooding cycle.

Typical bed slopes. E.M. Horstman et al. (2014) reported bed slopes of approximately 1:150 and 1:300 at the seaward edge of the mangrove transects in Kantang and Palian, Thailand, where the vegetation is dominated by *Avicennia sp.* and *Sonneratia sp.*. In contrast, *Rhizophora sp.* were more commonly found toward the landward side of the transects. Additionally, Das et al. (2011) identified a typical range of bed slopes between 1:100 and 1:500 at the mangrove forest fringe that were used in their study. Furthermore, van Wesenbeeck, van Zelst, et al. (2025) used three representative foreshore slopes, 1:500, 1:750, and 1:1000, in their recent study, based on a review of relevant literature.

Study	Location / Context	Bed Slope Range
E.M. Horstman et al. (2014)	Study site: Kantang and Palian, Thailand	1:150 to 1:300
Das et al. (2011)	Representative coastal topography for numerical simulations	1:100 to 1:500
van Wesenbeeck, van Zelst, et al. (2025)	Representative foreshore bed slope for numerical experiment	1:500 to 1:1000

Table 2.1: Reported bed slopes at mangrove transects from the literature.

2.2.3. Mangrove loss and recovery

Global mangrove coverage has declined significantly. In the past 50 years, between 20–35% of mangrove areas have been lost worldwide (Polidoro et al. 2010). This decline is driven by both human activities and natural events. According to Goldberg et al. (2020), from 2000 to 2016, anthropogenic drivers accounted for about 62% of global mangrove loss, while natural factors contributed the remaining 38%.

Mangrove loss

The primary human-driven cause of mangrove loss is the conversion of mangrove areas into aquaculture and agriculture, with Southeast Asia identified as a major hotspot. A well-known example is Demak, North Java, Indonesia, where large-scale mangrove deforestation and conversion to aquaculture triggered severe coastal erosion, with shoreline retreat rates reaching 100 m/yr (Winterwerp, Albers, et al. 2020) and even reaching a maximum of 250 m/yr (Gijón Mancheño 2022). Mangrove loss disrupted the balance between natural erosion and sediment deposition. Once mangroves were removed, the coast became exposed to greater wave and current action, intensifying sediment resuspension. As erosion deepened the nearshore zone, larger waves were able to propagate further inland, creating a positive (self-reinforcing) feedback loop of coastal retreat (Gijón Mancheño 2022). This indeed results in worse coastal flooding in the area. Figure 2.7 presents the degradation of mangrove triggered by changes of land use to aquaculture, leading to worse coastal flooding.

Extreme weather events, such as cyclones, droughts, heatwaves, and extreme floods, are one of the main causes of mangrove loss due to natural factors (Goldberg et al. 2020). In particular, tropical cyclones (TC) represent a substantial threat to mangroves, responsible for 97% of the storm-related risk of damage to these ecosystems, particularly the most intense storms (Category 4–5) (Mo et al. 2023). Referencing the report Herrera-Silveira et al. (2022), mangrove storm damage can be classified into two main categories:

Direct damage: Changes in structure, composition and biomass of mangroves. Strong storm winds can cause direct damage to mangroves by stripping leaves (defoliation), breaking branches, and uprooting trees. The severity of these impacts depends on the age and size of the tree community. Mature, larger trees often suffer from broken branches or trunks due to reduced flexibility, while uprooting can lead to either partial or complete tree mortality. Changes in environmental conditions, such as flooding duration, salinity, and sediment deposition, also affect tree survival post-storm. Structural changes may reduce forest complexity, shifting species dominance or creating clearings, as mature trees decline and younger, more resilient ones take hold.

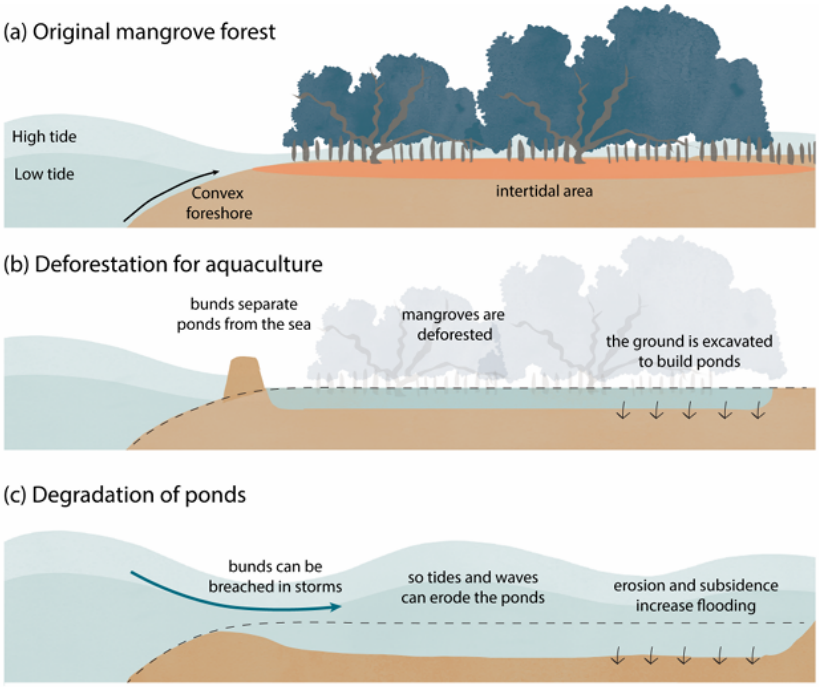

Figure 2.7: Stages of mangrove degradation in Demak: (a) healthy mangroves, (b) mangroves are cleared for shrimp ponds, (c) breached bunds expose ponds to tidal and wave erosion, worsened by subsidence. Picture from Gijón Mancheño (2022).

Indirect damage: Changes in topography, hydrology, and sediment characteristics. Coastal storms can deposit large amounts of sediment, reshaping the landscape and altering the natural hydroperiod of mangroves. Storm surges and currents transport sediment along coasts, while intense rainfall may erode inland areas, depositing sediment downstream. This reshaping may result in new outlets, barrier breaches, and blocked channels, impacting mangroves by:

- Raising elevation, which reduces water flow and can alter salt and nutrient exchange, leading to changes in sediment chemical characteristics. Disruptions in water flow due to sediment changes may lead to hypoxia (oxygen deficiency). Additionally, storm-induced sediment deposition can raise soil elevation, potentially burying propagules and hindering mangrove recolonisation.
- Lowering elevation, which increases flood depth and frequency, potentially hindering seedling survival. Greater inundation frequency also leads to increased salt stress that affects mangrove health.
- Creating new outlets alters salinity levels, water flows, and sediment transport within mangrove forests, further impacting their resilience.

This highlights that during real-life tropical cyclone-induced flooding, including compound flooding, the presence and condition of mangroves can change dynamically, leading to more complex interactions between hydrodynamics and vegetation that alter flooding outcomes.

Mangrove recovery

Mangroves can regenerate naturally after hurricane impacts, but this process may take several years, leaving forests vulnerable to further storm damage. Active restoration can accelerate recovery and enhance resilience (Herrera-Silveira et al. 2022). In contrast, mangrove loss from human activities—such as aquaculture conversion in Demak—requires more intensive interventions. Yet, replanting often shows low success rates, making large-scale rehabilitation difficult (Friess et al. 2019).

To address these challenges, nature-based solutions are increasingly promoted. Winterwerp, Bayney, et al. (2025) highlight that effective recovery often depends on restoring the physical and hydrodynamic conditions that support mangroves, rather than planting alone. For example, restoring hydrology

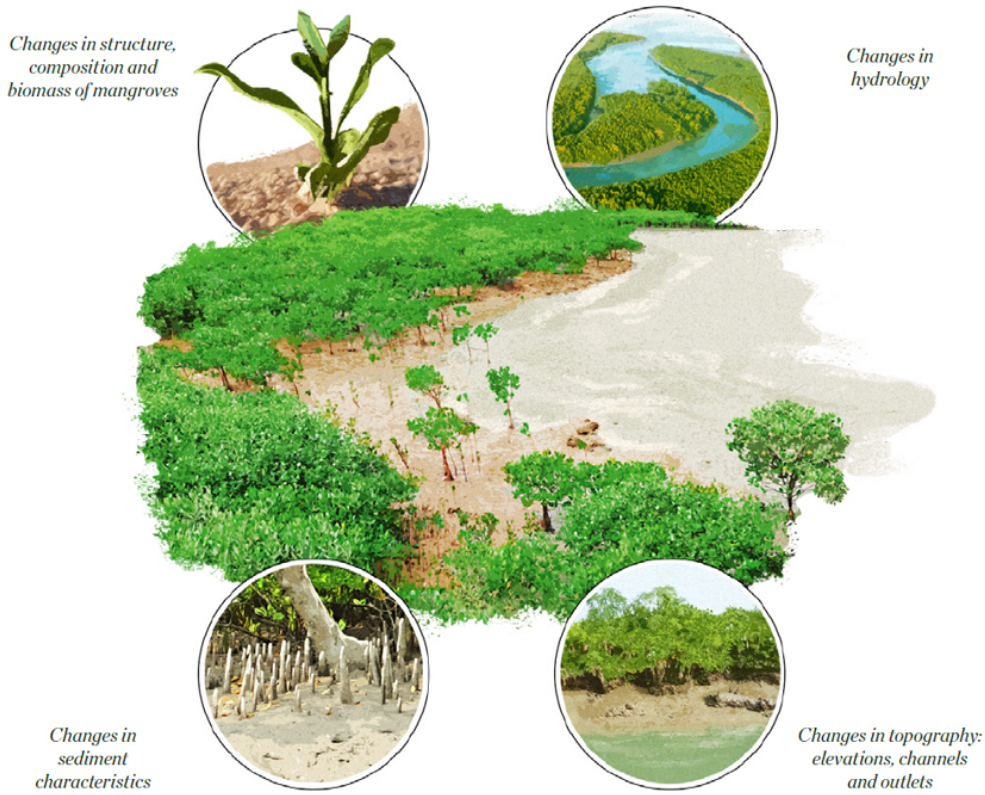

Figure 2.8: Types of mangrove damage. Picture from Herrera-Silveira et al. (2022)

through the reopening of tidal channels can improve flushing and reduce salinity stress, allowing natural seedling recruitment. In other cases, mangrove habitat can be created in combination with coastal defence structures, such as groynes or permeable breakwaters, which trap sediments and build intertidal mudflats suitable for colonisation. Offshore sand ridges, or artificial cheniers, may also be constructed to attenuate wave energy and promote mud deposition behind them, providing a stable substrate for mangroves. Finally, managed coastal setbacks—where dykes are relocated inland—can create new intertidal areas that quickly fill with mud and are naturally recolonised. Together, these approaches show that enabling the right environmental conditions is often more effective for mangrove recovery than direct replanting.

2.3. Coastal vegetation influence on flood drivers

Coastal vegetation interacts with waves, surges, and water levels in multiple processes. Vegetation attenuates incoming wave energy through drag, reduces storm surge peaks by impeding large-scale water motion, and modifies wave setup and setdown through local momentum exchanges. These processes operate through different mechanisms, but together they contribute to the role of vegetation as natural flood defences. This section reviews how vegetation influences wave height reduction, storm surge attenuation, and wave setup, followed by a concluding discussion on the importance of mangrove forest width. To support the fundamental understanding of these processes, the basic theory of ocean waves is provided separately in Appendix A.

2.3.1. Wave height reduction

Vegetation reduces wave height primarily by exerting drag on its structures, which dissipates wave energy as waves propagate through wetlands. A large body of experimental and field evidence demonstrates that coastal vegetation substantially reduces wave heights as they propagate inland. For salt marshes, Möller et al. (2014) showed in large-scale flume experiments that submerged vegetation reduced wave heights by up to 60% under storm surge conditions. Field observations confirm this effect: Jadhav et al. (2013) and Vincent Vuik et al. (2016) reported that short wind waves were re-

duced by about 50% within the first 30–50 m of marsh vegetation, even during energetic conditions. For mangrove systems, attenuation has also been observed at larger scales. E. M. Horstman (2014) showed strong attenuation within mangrove fringes in Southeast Asia. More recently, van Wesenbeeck, Wolters, et al. (2022) demonstrated in large-scale experiments that emergent trees reduced wave heights by 5–25% over a 40 m transect for significant wave heights of 1.5 m. Across different environments, reported attenuation rates generally range between 0.1 and 4% per meter (Gedan et al. 2011; Narayan et al. 2016). These attenuation rates are illustrated in Figure 2.9 transect 1. Variation of wave attenuation depends on vegetation properties, hydrodynamic conditions, and their interactions.

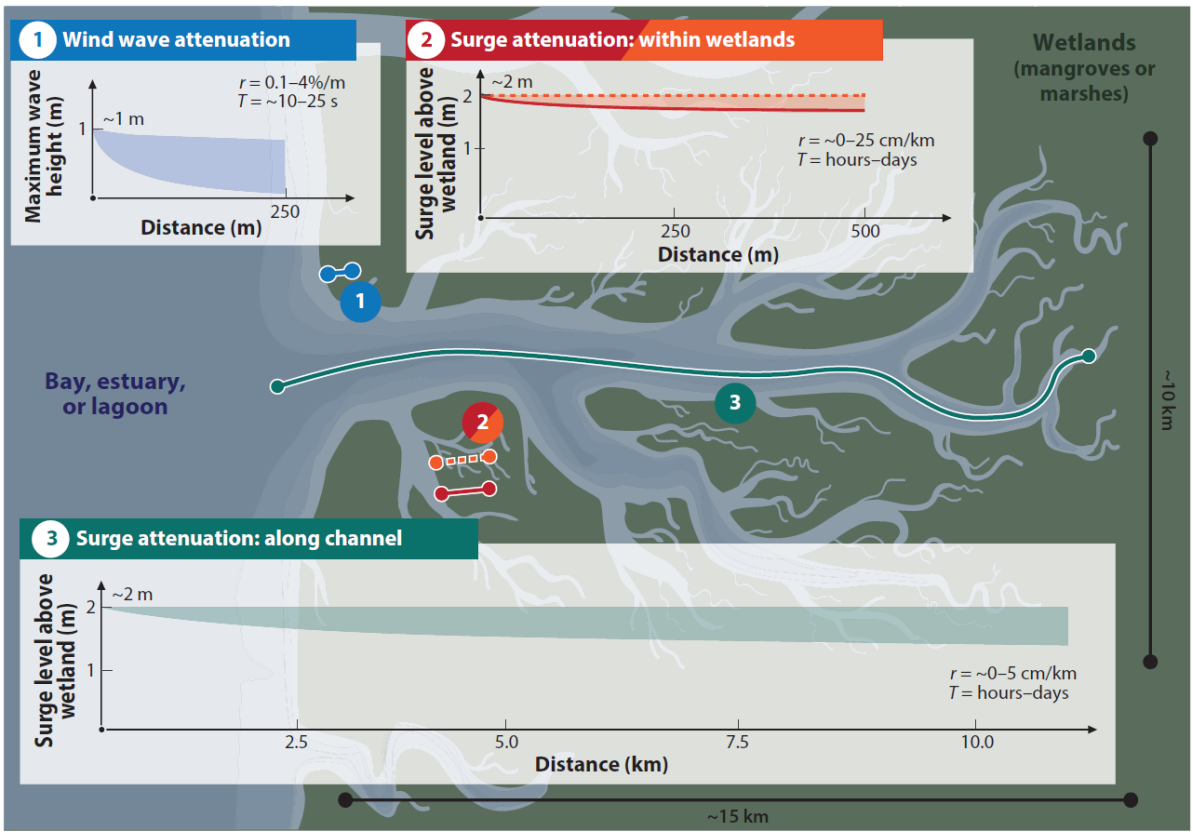

Figure 2.9: Schematic of contrasting length, timescales, and attenuation rates of wind wave (transect 1) vs. storm surge attenuation (transects 2 and 3). Here, r denotes wave attenuation rate and T the wave period. Picture from Temmerman et al. (2023)

Vegetation properties effects. Vegetation dissipation depends on structural parameters such as frontal area and canopy density. For woody species, Kalloe et al. (2022) showed that the projected frontal area (A_v), which accounts for complex branch structures, provides a more reliable predictor of wave attenuation than a single representative stem diameter and density. Similarly, Etminan et al. (2019) demonstrated that canopy density influences drag primarily through blockage effects, with dense canopies enhancing resistance and sparse canopies behaving more like isolated stems. Beyond these structural parameters, wave dissipation rates are known to depend on vegetation properties, hydrodynamic conditions, and their interactions, which can vary significantly across environments (Temmerman et al. 2023). For example, in mangrove forests, Mazda et al. (2006) and Quartel et al. (2007) observed that attenuation rates increased with water depth as denser canopy sections became submerged. In contrast, for fully submerged marsh vegetation, lower attenuation rates have been reported at increasing water depths due to reduced drag from both stems and the bed (Garzon et al. 2019; Schoutens et al. 2019). These studies highlight that frontal area, canopy density, and water depth-biomass distribution collectively shape the effective wave dissipation capacity of vegetated foreshores.

Frequency-dependent dissipation. Vegetation dissipates different wave components unevenly. Short waves are rapidly attenuated within relatively narrow belts, while long-period infragravity waves penetrate much further into the forest (Phan et al. 2015; van Rooijen et al. 2016). Consequently, the protective function of mangroves depends on forest width relative to the dominant wave frequencies during extreme events. Observations also show that dissipation patterns vary across the frequency spectrum: Anderson and J. M. Smith (2014) found that high-frequency wind waves (above the spectral peak) were preferentially dissipated. In contrast, Riffe et al. (2011) demonstrated that both high and low frequencies were more strongly dissipated by vegetation. Much less is known about vegetation effects on infragravity waves (periods 25–250 s), although Norris et al. (2021) showed that infragravity waves in mangroves are substantially less attenuated than shorter-period waves, consistent with theoretical predictions of Henderson, Norris, et al. (2017). These findings highlight that frequency-dependent dissipation is complex and site-specific, and that attenuation rates depend on both vegetation characteristics and the spectral composition of incident waves (Temmerman et al. 2023).

2.3.2. Storm surge reduction

Storm surges are large-scale elevations of the sea surface caused by intense storm systems. They result from a combination of low atmospheric pressure and strong winds, with spatial and temporal scales similar to those of the storm itself (Resio and Westerink 2008; Bosboom and Stive 2023). Typically, storm surges have slightly shorter periods and wavelengths than tides. As they move toward the coast, the water accumulates, potentially leading to severe coastal flooding (Temmerman et al. 2023).

As storm surge propagates through a vegetated area, the water motion experiences drag, which limits the water exchange and reduces the peak water level reached within and often behind the wetland, depending on local geomorphology. This process is called storm surge attenuation. Some models of surge propagation are typically based on the shallow-water equations, where the vegetation drag is implemented in the momentum equation. The drag force by vegetation due to storm surge propagation is similar to that stated in equation 2.9 (Temmerman et al. 2023).

Mechanisms. There are two general mechanisms of storm surge attenuation by vegetation (or wetlands): The within-wetland attenuation (e.g Montgomery et al. (2019)) and the along-channel attenuation (e.g Smolders et al. (2015)), as reviewed by (Temmerman et al. 2023). The within-wetland attenuation is surge attenuation within vegetation in the wetland, basically driven by pressure difference balance with friction by the vegetation. Therefore, this mechanism is also known as the friction effect. The along-channel attenuation is the mechanism by which storm surge propagates through the channel, and the water spreads laterally through the wetland, causing attenuation. This mechanism is called the storage effect due to the water stored in the wetland as it propagates along the channel. Figure 2.9 illustrates the difference in the within-wetland attenuation and along-channel attenuation, as well as the wind wave attenuation.

Study evidence. Model studies consistently show that storm surge attenuation depends strongly on larger-scale landscape settings (Temmerman et al. 2023). Wide, continuous marshes and mangroves—extending tens of kilometres—can induce significant within-wetland attenuation, with simulated rates ranging from 2–16 cm/km in the Mississippi Delta (Resio and Westerink 2008; Wamsley et al. 2010). In addition, along-channel attenuation has been found to be especially effective when wetlands are located farther inland along narrow, funnel-shaped estuaries (Fairchild et al. 2021; Smolders et al. 2015). By contrast, wetlands adjacent to wide open bays or back-barrier lagoons contribute much less to surge reduction (Marsooli et al. 2017). These results highlight that the contribution of vegetation to storm surge attenuation, and thus to reducing flooding in the hinterland, depends not only on vegetation drag processes but also on the width, continuity, and setting of the wetland landscape.

2.3.3. Wave setup reduction

Besides attenuating wave heights, vegetation also influences mean water levels at the coast by modifying wave setup. Wave setup arises from gradients in radiation stress as waves shoal and break, leading to an onshore increase of the mean water level. When vegetation dissipates wave energy, these cross-shore radiation stress gradients are altered, generally resulting in a reduction of wave setup (Buckley et al. 2016).

Additionally, Dean and Bender (2006) demonstrated that vegetation can generate a net opposing force on the water column due to two mechanisms: (i) variation in the submerged vegetation height over a wave cycle in the case of emergent vegetation, and (ii) nonlinear intrawave drag forces under skewed waves. Both effects produce a wave-averaged drag that counteracts the radiation stress gradient, thereby reducing setup. These findings were later confirmed experimentally by Wu et al. (2011), who observed reduced wave setup up to eight times, and even led to set-down, in flume experiments with vegetation on both flat and sloping bottoms compared to scenarios without vegetation (see Appendix D). Moreover, other studies have also identified mean drag forces components associated with mean flow (Sigrid M. Løvås and Tørum 2001; Luhar et al. 2010) as contributing to vegetation–setup interactions.

Overall, while the effect of vegetation on wave setup has been less frequently quantified than wave attenuation, existing evidence suggests that it can significantly reduce coastal water levels during energetic wave events. This mechanism is therefore relevant for flood risk assessments, yet it is often overlooked in current practice.

2.3.4. Influence of forest width: Mangrove case studies

The extent to which vegetation can influence waves, surges, and setup depends strongly on forest width. Narrow belts may attenuate short waves but generally have a limited impact on surges or infragravity waves, while wide forests can substantially reduce multiple flood drivers simultaneously. However, the definition of “effective” width varies across studies depending on the target outcome—whether shoreline stability, wave attenuation, surge reduction, or economic loss mitigation. This subsection reviews reported thresholds of effective mangrove widths and their implications for coastal defence. Here, we focus on mangrove forest width as the core of the discussion.

Global mangrove forest width. van Wesenbeeck, van Zelst, et al. (2025) study provides the global map of mangrove width based on a global dataset. Figure 2.10 shows the global map of mangrove width, with mangrove width classes represented in different colours: purple indicates widths of 0–100 meters, yellow represents 100–500 meters, and green corresponds to widths greater than 500 meters. Pie charts illustrate the distribution of these width classes across each IPCC AR6 region. The legend includes the total number of transects within each class.

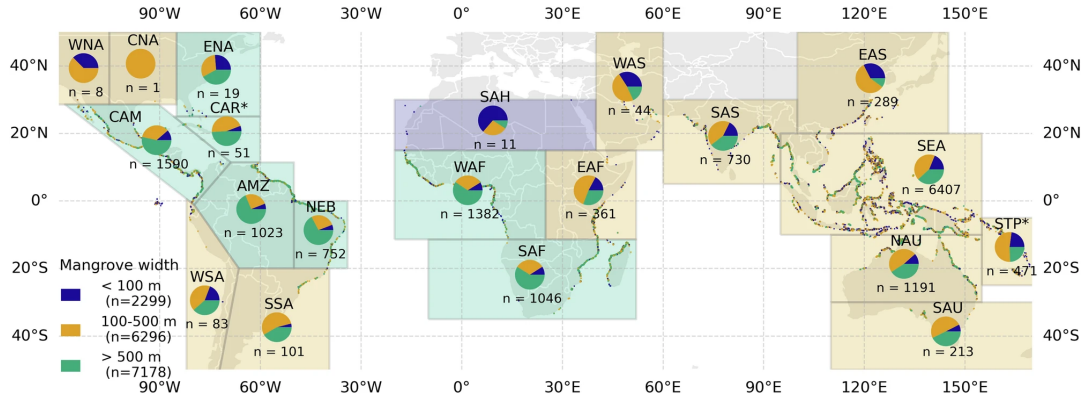

Figure 2.10: Global distribution of mangrove forest widths, based on the dataset from van Wesenbeeck, van Zelst, et al. (2025). Mangrove width classes are shown in purple (0–100 m), yellow (100–500 m), and green (>500 m). Pie charts indicate the proportion of each class within IPCC AR6 regions. The legend presents the total number of transects per class.

Economic impact. A large-scale assessment using remote sensing of nighttime luminosity shows that wider mangrove belts are associated with lower economic losses from cyclones (Hochard et al. 2019). Additionally, a full mitigation effect has been observed for mangrove belts wider than 1000 m (Valle et al. 2020). Related to hydrodynamics, different mangrove widths correspond to different capacities for flood risk reduction, particularly through mechanisms such as wave attenuation and storm surge reduction.

Wave attenuation. A recent study by van Wesenbeeck, van Zelst, et al. (2025) assessed the wave attenuation capacity by running 216,000 numerical models under realistic conditions. The results show

that mangrove forests wider than 500 meters dissipate approximately 75% of incoming wave energy regardless of the local conditions. In contrast, wave attenuation in forests narrower than 500 meters is strongly dependent on local water levels, wave characteristics, and forest density. These findings suggest that the recommended mangrove belt width, which is currently set between 50 and 200 m in several countries, should be increased to at least 500 m. Furthermore, Maza et al. (2019) shows that the front-edge trees often bear the highest loads, due to wave shoaling at the seaward slope, which increases wave steepness and forces at the forest front, before significant decay occurs inside the forest. This explains the mechanism of the vegetation force exerted in the mangrove forest.

Shoreline stability. In addition, Phan et al. (2015) analysed the Mekong Delta, where mangrove forests are increasingly squeezed into narrow strips, sometimes as narrow as 100 m, due to sea-dike construction and land reclamation. In such settings, dikes prevent inland migration of mangroves while shoreline erosion reduces the seaward edge, leaving only a narrow band of vegetation. Their study demonstrated a critical minimum width of around 140 m, not in terms of coastal defence efficiency, but as an ecological threshold to sustain healthy mangroves capable of promoting sedimentation and supporting seedling survival. They also highlighted that while short wind waves are attenuated rapidly, long infragravity waves penetrate much deeper into the forest, which may disturb sediment deposition and seedling establishment, thereby linking mangrove width directly to ecosystem stability. Complementary experimental work by Austin (2021) also demonstrated that wider mangrove stands provide greater shoreline stabilisation under varying tidal water levels, with minimal forest widths still offering some erosion protection, but wider root systems being required to resist retreat during extreme high-water conditions. Together, these studies underscore the critical role of mangrove width in maintaining both ecological functioning and shoreline stability.

Storm surge attenuation. In the context of the storm surge attenuation, wider wetland widths are required compared to those needed by the waves (Temmerman et al. 2023). A numerical modelling study by De Dominicis et al. (2023) shows the effectiveness of mangrove forests as coastal defences in the Pearl River Delta, China. During Typhoon Hato (2017), a mangrove belt 600 meters wide reduced the maximum coastal surge level by half. A belt width of 900 meters effectively eliminated the surge at the coast. However, a narrower width of 300 meters had a limited or negligible impact on peak surge levels. These results are influenced by the vegetation drag, with higher-drag vegetation leading to more effective reduction of surge peaks.

Table 2.2 presents a summary of critical or effective mangrove widths and their associated key findings, highlighting that different studies define width thresholds based on different indicators.

Study	Effective Width	Indicator / Focus	Key Findings
Temmerman et al. (2023)	$>$1000 m	Economic impact	Remote-sensing analysis shows full mitigation of cyclone losses when belts exceed 1000 m; narrower belts provide only partial protection.
van Wesenbeeck, van Zelst, et al. (2025)	$>$500 m	Wave attenuation	Global modelling (216,000 runs) indicates forests wider than 500 m dissipate $\sim$75% of incoming wave energy regardless of local conditions.
Phan et al. (2015)	$\sim$140 m	Ecological stability	Minimum width needed to sustain healthy mangroves in the Mekong Delta. Narrow strips (< 100 m) fail to maintain sedimentation or seedling survival.
De Dominicis et al. (2023)	600–900 m	Surge attenuation	Modelling of Typhoon Hato (2017) in the Pearl River Delta: 600 m belt halves surge; 900 m eliminates surge. Narrow belts ($\sim$300 m) have negligible impact.

Table 2.2: Summary of effective mangrove widths reported in recent studies, based on different indicators (ecological stability, wave attenuation, surge reduction, economic impact).

2.4. Modelling of hydrodynamics-vegetation interactions

Flood models can generally be grouped into three categories: simple, full-physics, and reduced-physics. Simple models, such as the static bathtub approach, overlay extreme water levels onto a Digital Elevation Model (DEM) and neglect processes like flow routing, tidal amplification, and vegetation-induced friction. They are computationally cheap but oversimplified and therefore not relevant for this study (Sanders et al. 2024). Full-physics models, such as `XBeach` and `Delft3D-FLOW`, solve detailed hydrodynamic equations (e.g., nonlinear shallow-water or Reynolds-averaged Navier–Stokes), capture multiple flood drivers, and explicitly represent vegetation, but at high computational cost (T. Leijnse et al. 2021). Reduced-physics models offer a middle ground by retaining the essential hydrodynamics while remaining computationally efficient, making them well-suited for large-scale flood scenarios. We therefore focus on full-physics and reduced-physics models, which can represent the relevant physical processes with different levels of detail and computational demand.

In this context, coastal flood drivers are typically modelled with two complementary equations: (i) a wave energy balance for sea–swell waves (with dissipation by breaking, bottom friction, and vegetation), and (ii) the depth-averaged momentum and continuity equations for mean flows (tide/surge, return flow/undertow) and mean water levels (setup/setdown). Vegetation consistently enters these formulations as a quadratic drag term that depends on plant geometry and flow velocity.

2.4.1. Wave dissipation by vegetation

Wave dissipation due to vegetation has been explored by many studies. Some studies approach the wave dissipation by representing vegetation as an increased bottom friction coefficient, such as Hasselmann and J. Collins (1968). In contrast, other studies represent vegetation as vertical cylinders, considering its force on the structures, such as Dalrymple et al. (1984). The structure approach is then preferred because of its relation of wave attenuation to plant geometry (height, diameter, and density).

Dalrymple et al. (1984) presented an analytical solution for wave height evolution through a vegetation field on a flat bottom subject to regular waves. Using the time-averaged energy balance, wave energy dissipation due to vegetation (D_v) is defined by the work done by waves on the vegetation integrated over the submerged vegetation height. By incorporating wave dissipation due to breaking (D_b) as well (Thornton and Guza 1983), the wave dissipation formula is defined as:

$$\frac{\partial}{\partial x}(E\, c_g) = -\langle D_b \rangle - \langle D_v \rangle \tag{2.1}$$

$$D_b = \frac{\sqrt{3\pi}}{16}\, \rho g\, \frac{B^3 f_p}{\gamma_b^4\, h^5}\, H_{\mathrm{rms}}^7 \tag{2.2}$$

$$D_v = \overline{\int_{-h}^{-h+h_v} F_x\, dz}, \tag{2.3}$$

where E is wave energy per unit area, c_g is wave group velocity, B and γ_b are adjusting parameters, f_p is average frequency corresponding to the peak period (T_p), H_{rms} is root-mean square wave height, ρ is fluid density, g is gravity acceleration, h is water depth, h_v' is submerged vegetation height, and F_x is force on vegetation.

The Morison equation gives the force on the vegetation (F_x) (Morison et al. 1950), which is actually composed of two components: drag force and internal force. For vegetation, the Morison equation is commonly reduced to the drag term only, since slender stems in drag-dominated flow contribute little inertia; the inertia force is out of phase with velocity and therefore negligible compared to the drag component (Kalloe et al. 2022). Furthermore, if the water level reaches the canopy, the densities are usually low enough that porosity effects (blockage and sheltering) can be neglected as well (Etminan et al. 2019). Thus, the vegetation drag force (F_x) is defined as a function of flow velocity (u) and vegetation parameters as follows:

$$F_x \approx F_D = \tfrac{1}{2}\rho C_D b_v N u|u|. \tag{2.4}$$

Two decades later, Mendez and Losada (2004) extend the application of Dalrymple et al. (1984) to take into account sloping beds and irregular waves. The wave dissipation term (D_v) thus defined as:

$$D_v = \frac{1}{2\sqrt{\pi}} \rho C_D b_v N \left(\frac{kg}{2\sigma}\right)^3 \frac{\sinh^3(kh'_v) + 3\sinh(kh'_v)}{3k\cosh^3(kh)} H^3_{\text{rms}}, \tag{2.5}$$

where k is the wave number. Lately, Suzuki et al. (2012) further adapted Mendez and Losada (2004) wave dissipation term to take into account varying vegetation parameters along the vertical structure, as illustrated in Figure 2.11. This layering approach has been used in some phase-averaged wave models, such as SWAN.

Layering vegetation structure parameters

Vegetation can be represented as a vertical layering schematization to simplify its real form, as has been done by Suzuki et al. (2012) to quantify wave dissipation by vegetation. Additionally, van Wesenbeeck, van Zelst, et al. (2025) also used the same approach on mangrove schematization for numerical modelling to determine the representative mangrove frontal surface area (f_v). Because of its variability along the heights, mangroves are often schematized as three vertical layers: root (layer 1), trunk (layer 2), and canopy (layer 3). Figure 2.11 shows this simplified representation, which allows for the integration of vegetation effects in numerical wave models.

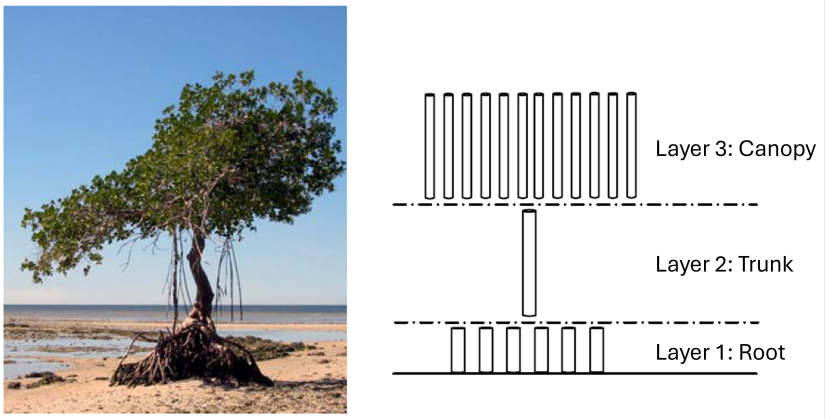

Figure 2.11: Schematization of mangrove vegetation using three vertical layers: root, trunk, and canopy, as used in wave dissipation models. Picture adapted from Burger (2005).

Based on this schematisation, Janssen (2016) summarised key physical parameters of mangrove structures for each vertical layer. Aligned with the mangrove classification discussed earlier, the focus is on red and black mangrove species. The primary structural parameters include N_v (vegetation density), b_v (vegetation width), and h_v (vegetation height). Lastly, a commonly used parameter is the frontal surface area (f_v), defined as the product of vegetation width and density for each layer:

$$f_{v,i} = b_{v,i} \cdot N_{v,i} \quad \text{(where } i \text{ is the layer number).}$$

Table 2.3 provides a detailed overview of these parameters for varying forest densities. Due to a lack of data, the canopy layer only contains the f_v and h_v parameters.

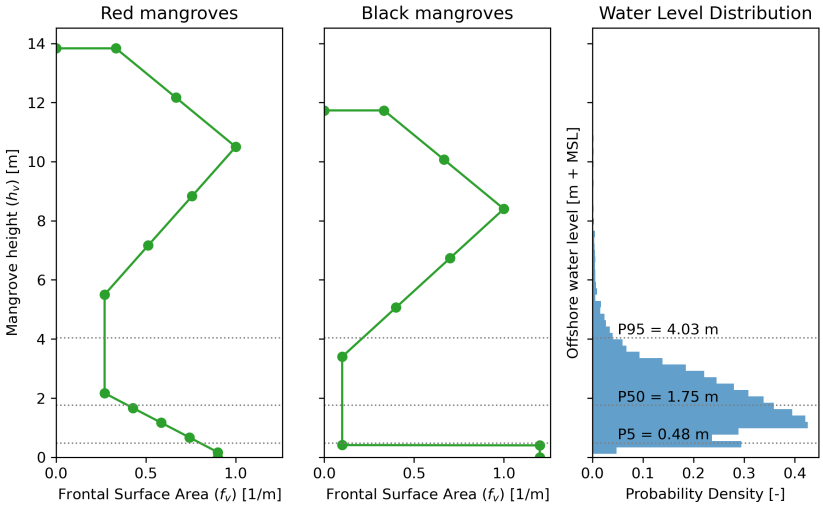

Figure 2.12: Frontal surface area (f_v) along plant height (h_v) for red and black mangroves based on datasets from van Wesenbeeck, van Zelst, et al. (2025). The right panel shows offshore water level in the mangrove environment (van Zelst et al. 2021).

Type	Density	Layer 1: Root				Layer 2: Trunk				Layer 3: Canopy	
		N_v (r/m^2)	b_v (cm)	f_v (m^{-1})	h_v (m)	N_v (s/m^2)	b_v (cm)	f_v (m^{-1})	h_v (m)	f_v (m^{-1})	h_v (m)
Red	S	15	1	0.2	0.30	0.3	20	0.06	2	0.1	10
	M	45	2	0.9	0.50	0.6	45	0.27	5	1.1	12
	D	70	3	2.1	1.00	0.9	75	0.68	8	4.5	12
Black	S	45	0.5	0.2	0.15	0.1	10	0.01	1	0.5	9
	M	120	1	1.2	0.40	0.4	25	0.10	3	0.5	11
	D	240	4	9.6	0.80	1.1	70	0.77	8	7.7	13

Table 2.3: Physical mangrove parameters for different vegetation densities (S = sparse, M = medium, D = dense), including root (r) and stem (s) characteristics. Data from Janssen (2016).

Moreover, van Wesenbeeck, van Zelst, et al. (2025) established a graph that links mangrove structural parameters and hydrodynamic exposure using global data (n=15,773). In their extreme value analysis, they used return periods of 2, 5, 10, and 25 years to fit a probability distribution of offshore water levels. From this distribution, they derived key percentile values (P5, P50, and P95), which were visualised to represent typical and extreme water level conditions. Figure 2.12 presents the mangrove structural parameters alongside the global distribution of offshore water levels.

Bulk drag coefficient C_D

The bulk drag coefficient (C_D) is a key parameter describing vegetation-induced resistance under varying hydraulic conditions. It captures complex hydrodynamic–vegetation interactions such as skin friction, pressure differences, and stem swaying. Because of this complexity, many studies calibrate C_D against laboratory or field measurements, often by relating it to hydraulic dimensionless numbers. The Reynolds number ($Re = U_c d/\nu$) expresses the ratio of inertial to viscous forces and indicates whether flow around vegetation is laminar or turbulent, while the Keulegan–Carpenter number ($KC = U_c T/d$) represents the ratio of fluid particle excursion length over a wave cycle to obstacle size, distinguishing drag-dominated from inertia-dominated regimes. A decrease in bulk drag coefficient with increasing KC has been consistently observed (Kalloe et al. 2022): at low KC, flow separation around stems is limited and the vegetation exerts relatively stronger resistance, leading to higher C_D; whereas at high KC, larger particle excursions promote more complete vortex shedding and a reduced bulk C_D.

For mangroves, Maza et al. (2019) experimentally analysed wave attenuation and drag forces in a realistic fringe *Rhizophora* forest at scale 1:6, reporting C_D values between 0.5 and 1.5. They found that C_D derived from wave attenuation formulations can overestimate drag forces if other dissipation sources (e.g., bed or sidewall friction) are not excluded, underscoring the need for careful calibration. Similarly,

Hendriks (2014) derived parameterisations for mangroves using field data collected in Thailand by E. Horstman et al. (2012) and E. M. Horstman (2014), yielding empirical relations between C_D and KC. Under extreme hydraulic conditions, van Wesenbeeck, Wolters, et al. (2022) investigated rigid woody vegetation (willow), offering relevant analogies for mangroves due to their structural similarities.

Flexibility effects. Vegetation flexibility plays a critical role in wave dissipation, primarily through its effect on the bulk drag coefficient (C_D). Flexible stems bend and sway with the flow, reducing their effective frontal area compared to rigid vegetation. Consequently, both drag forces and energy dissipation are typically lower under the same hydraulic conditions (Sumer and Fredsøe 1998). Experimental work by van Veelen et al. (2020) showed that wave damping by flexible vegetation can be up to 70% lower than for rigid vegetation due to this swaying motion. Moreover, rigid vegetation was observed to modify the velocity structure by generating a mean current in the direction of wave propagation and amplifying horizontal particle velocities directly above the canopy, while flexible vegetation did not exhibit such effects. These findings highlight flexibility as a key parameter in wave–vegetation interactions, suggesting that dissipation rates derived from rigid-vegetation formulations may overestimate energy losses for flexible species such as salt marsh grasses. The difference in C_D values between rigid and flexible vegetation, as observed by van Veelen et al. (2020), is shown in Figure 2.13.

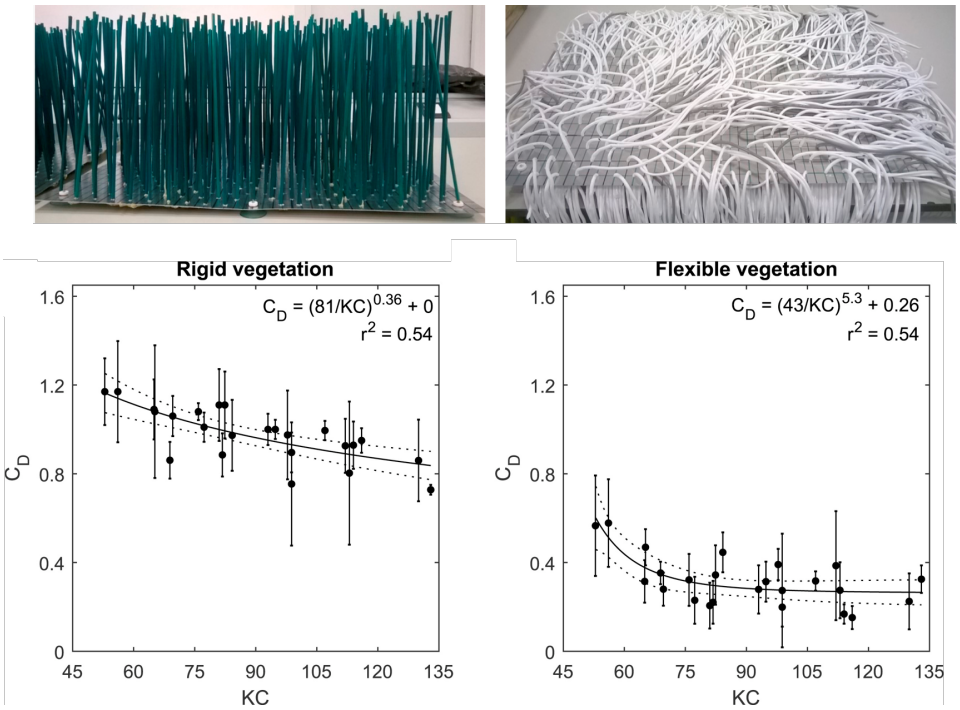

Figure 2.13: Comparison of drag coefficient (C_D) values between rigid and flexible vegetation based on the experiments of van Veelen et al. (2020).

Storm condition uncertainty. Most relationships for the bulk drag coefficient (C_D) are derived from laboratory experiments or field observations under mild wave conditions. These results cannot be directly extrapolated to storm conditions, where larger wave heights, greater water depths, and enhanced turbulence happen (Temmerman et al. 2023). For example, Pinsky et al. (2013) noted that extending Re-based parameterisations of C_D to storm conditions may lead to significant overestimations of wave attenuation. Only a limited number of studies have explored vegetation performance under such extreme conditions. In addition to the work of van Wesenbeeck, Wolters, et al. (2022) in willow trees, flume experiments by Möller et al. (2014) showed that submerged salt marsh vegetation reduced wave heights effectively during storm surge conditions (water depths of 2 m and incident waves of $H = 0.9$ m), with approximately 60% of the attenuation attributed to the vegetation. Another key source of uncertainty is the potential for vegetation breakage and uprooting during storms, for which empirical data remain scarce and limited to very few species (V. Vuik et al. 2018).

2.4.2. Mean water level influenced by vegetation

This subsection addresses the increase (set-up) and decrease (set-down) of the mean water level induced by waves and currents. These processes result from the momentum carried by the waves, the associated radiation stress, and the resulting wave-induced forces. Additionally, storm surges might also add flow that alters the mean flow velocity. A detailed discussion of the underlying wave theory is provided in Appendix A; here we focus on how vegetation modifies these processes through cross-shore momentum balance and mass balance.

Cross-shore momentum balance

We consider a simplified case of an alongshore-uniform coast, consistent with the assumptions in Appendix A. In the cross-shore direction, the shoaling of waves increases the radiation stress (positive gradient), resulting in offshore-directed forces that lower the mean water level (set-down). After wave breaking, radiation stress decreases (negative gradient), producing onshore-directed forces that raise the mean water level (set-up). This behaviour can be described with a 1D momentum balance (Eq. A.18). Under stationary conditions, neglecting surface stress, velocity gradients, and horizontal mixing, the simplified momentum equation becomes

$$\underbrace{g\frac{\partial \eta}{\partial x}}_{\text{Water level slope}} = \underbrace{\frac{F_x}{\rho h}}_{\text{External force}} + \underbrace{\frac{\tau_{bx}}{\rho h}}_{\text{Bed shear stress}}, \tag{2.6}$$

where F_x here represents only the wave-induced force. Following van Rooijen et al. (2016), it is convenient to decompose the external forces into wave-induced and vegetation-induced contributions, $F_x = F_w + F_v$. The cross-shore momentum balance can then be written as:

$$\underbrace{g\frac{\partial \eta}{\partial x}}_{\text{Water level slope}} = \frac{1}{\rho h}\Big(\underbrace{F_w}_{\text{Wave-induced force}} + \underbrace{F_v}_{\text{Vegetation drag force}} + \underbrace{\tau_{bx}}_{\text{Bed shear stress}} \Big) \tag{2.7}$$

In the following, we discuss how vegetation influences each force component and thereby modifies wave-induced set-up and set-down.

Wave-induced force (F_w) influenced by vegetation drag. Vegetation alters wave transformation processes such as shoaling and breaking, thereby modifying the cross-shore radiation stress gradient profile, resulting in reduced wave force (F_w). Without vegetation, the radiation stress gradient is balanced by bed shear stress and pressure gradient. With the presence of vegetation, radiation stress gradients often get larger in relatively deep water and smaller in shallow water. This typically results in a reduced wave force (F_w) and hence a reduction in wave setup (van Rooijen et al. 2016). Similar effects have been reported in other rough coastal systems; for instance, Buckley et al. (2016) found that large bottom roughness elements on fringing reefs modified radiation stress gradients and consequently influenced setup dynamics, consistent with the principle that additional roughness alters the force balance driving wave setup.

Vegetation drag force (F_v). Besides the alteration of wave-induced force F_w, the vegetation also introduces its own drag force acting in the water column. The vegetation force can be divided into two components: $F_{v,m}$ and $F_{v,w}$. The term $F_{v,m}$ represents the vegetation force related to mean (undertow) and unsteady (IG wave) currents. On the other hand, $F_{v,w}$ denotes the intrawave vegetation force.

$$F_v = F_{v,m} + F_{v,w} \tag{2.8}$$

1. **Mean drag force due to mean flow ($F_{v,m}$)**: The vegetation presence has an effect on the mean flow, resulting in a vegetation drag force. The mean current is typically directed offshore (undertow) for a wave-dominated case, which causes the force acting on the vegetation stems, resulting in the opposite (onshore). Consequently, due to the vegetation force onshore directed, the wave setup could be expected to increase due to an increase in this force component. Additionally, it is

also appropriate to include IG waves in the vegetation force because their orbital motion is usually much larger than the distance between vegetation stems, so they act like unsteady currents.

In contrast, for surge- or tide-dominated cases, this component is expected to produce offshore forcing due to surge currents propagating onshore. Thus, in this case, the water level is expected to be lower (set-down) due to the decrease of this forcing component. Equation 2.9 presents the formulation of this component, where ρ is water density, C_D is the drag coefficient, and b_v, N_v, and h'_v are stem diameter, density and height of the submerged vegetation, and u_E is the Eulerian velocity. Figure 2.14 panel A illustrate the process of this vegetation force.

$$F_{v,m} = \frac{1}{2}\rho C_D b_v N_v h'_v \, u_E \, |u_E| \tag{2.9}$$

2. **Wave-induced force due to emergent vegetation and wave skewness ($F_{v,w}$)**: The intrawave-related vegetation force components have two main causes: wave-induced force due to emergent vegetation and due to skewed waves. First, in fully emergent vegetation, the submerged vegetation height (h'_v) is varied over a wave cycle, equal to the instantaneous water depth. In case of partly emergent vegetation, the submerged vegetation height is determined by the minimum of the vegetation height itself and the local water depth. In case of fully submerged vegetation, the submerged vegetation height is simply equal to the vegetation height itself. Thus, over one wave cycle, the emergent vegetation has the variation of the (h'_v) and thus contributes to the $F_{v,w}$ formula in equation 2.10 below. However, the fully submerged vegetation does not give any variation of h'_v over a wave cycle, thus, no contribution to $F_{v,w}$.

   Second, due to nonlinear (skewed) waves, even for fully submerged vegetation, there is an additional effect that contributes to the $F_{v,w}$. In skewed waves, the depth-averaged velocity profile over one wave cycle shows a sharper peak in the propagation direction and a flatter trough. Thus, due to this nonlinearity, the variation of orbital velocity u_w over a wave period contributes to the vegetation force $F_{v,w}$ in equation 2.10. In the equation, T_{rep} is the representative wave period and u_w is the depth-averaged orbital velocity over one wave cycle. In practice, the nonlinearity effect of u_w is often estimated by a separate empirical model, called the wave shape model (Rienecker and Fenton 1981). The description of this model can be found in Appendix B.

$$F_{v,w} = \int_0^{T_{\mathrm{rep}}} \frac{1}{2}\rho C_D b_v N_v h'_v \, u_w \, |u_w| \, dt \tag{2.10}$$

   Figure 2.14 panel B-D shows the illustration of $F_{v,w}$ generation due to emergent vegetation (variation of h'_v over a wave cycle) and nonlinearity of the waves (skewed profile of u_w over a wave cycle).

Cross-shore mass balance

In an alongshore-uniform coast, the cross-shore mass balance requires that the net depth-integrated flow is conserved. In stationary conditions, this implies that the depth-averaged cross-shore current must vanish, since water cannot continuously pile up against the coast or drain seaward. The onshore-directed mass flux in the upper part of the water column is therefore compensated by an offshore-directed return flow at lower elevations, such that the net transport across any cross-shore section is zero.

$$\underbrace{\frac{\partial \eta}{\partial t}}_{\text{Local change of surface}} + \underbrace{\frac{\partial (Uh)}{\partial x}}_{\text{Advection of volume}} = 0 \tag{2.11}$$

Equation 2.11 represents the classical continuity relation for an unobstructed water column, where the full cross-sectional area h is available for flow. In vegetated systems, however, part of this cross-section is occupied by stems and roots. This can be expressed by introducing a porosity factor ϕ (the ratio of open flow area to total area), leading to an effective term (ϕh) instead of h in the continuity equation. As stem density increases, ϕ decreases and pore velocities ($U_p = U/\phi$) rise for the same

discharge. These elevated velocities amplify vegetation drag forces, meaning that resistance depends not only on stem-scale geometry but also on canopy density. Laboratory experiments with emergent rigid cylinders by Tanino and Nepf (2008) confirmed that the bulk drag coefficient (C_D) decreases with increasing Reynolds number but increases with vegetation density (ϕ). This highlights that drag formulations based solely on stem geometry, such as the Morison equation, may underestimate resistance in dense canopies. Moreover, under extreme conditions, additional processes such as stem breakage, uprooting, flexibility, and debris transport further affect the effective drag, underscoring the need for careful parameterisation in flood models.

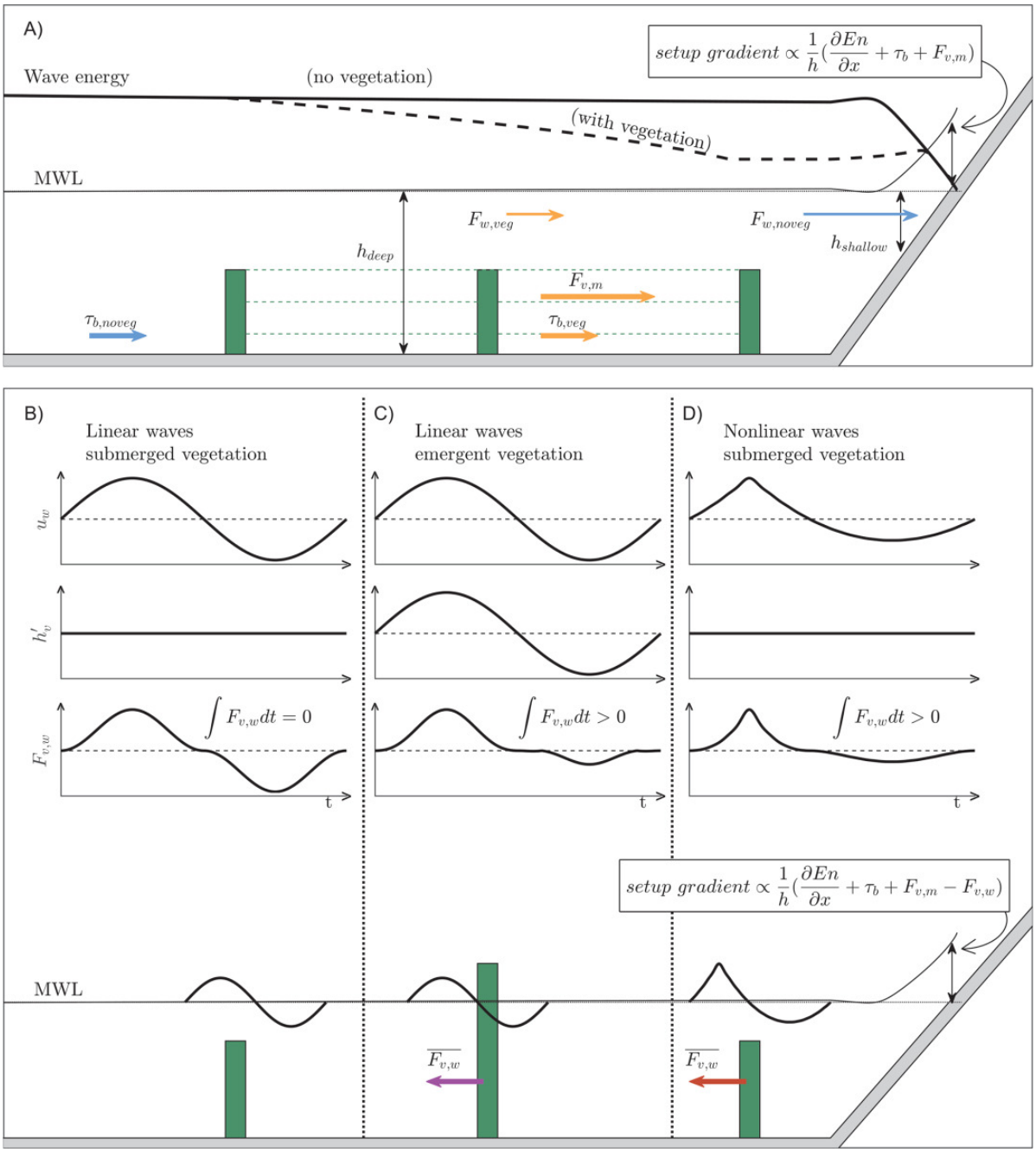

Figure 2.14: Illustration of wave-vegetation interaction and resulting forces on the water column. (a) Vegetation reduces wave force (F_w) through radiation stress gradients and introduces a mean vegetation drag force ($F_{v,m}$). Panels (b–d) show intrawave velocity (u_w), submerged height ($h'v$), and vegetation force (Fv, w) for linear and nonlinear waves with submerged or emergent vegetation. Net vegetation forces ($\overline{F_{v,w}}$) are shown by colored arrows. Figure from van Rooijen et al. (2016).

2.5. XBeach vs. SFINCS-SnapWave

Hydrodynamic models simulate flooding by capturing the physics of hydrodynamic processes and their interactions with vegetation. In this section, we discuss two models: XBeach, which serves as a full-physics benchmark, and SFINCS-SnapWave, a reduced-physics model that will be used in this study. This comparison is useful because XBeach provides detailed, process-based simulations, while SFINCS-SnapWave offers computational efficiency for large-scale flood scenarios.

XBeach is a full-physics model capable of simulating both hydrodynamic and morphodynamic processes, with extensions that explicitly include vegetation effects. It can be run in three hydrodynamic modes: stationary wave, surfbeat (phase-averaged), and non-hydrostatic (wave-resolving) (J. A. Roelvink et al. 2009; XBeach Manual 2025). The stationary mode efficiently solves wave-averaged equations but neglects infragravity (IG) waves. The surfbeat mode includes short-wave group variations, resolving IG waves associated with groupiness. The non-hydrostatic mode combines the nonlinear shallow-water equations with a pressure-correction term, enabling the resolution of individual waves.

SFINCS (Super-Fast INundation of CoastS) is a reduced-physics hydrodynamic model developed for efficient simulation of compound flooding from fluvial, pluvial, tidal, wind-, and wave-driven processes (T. Leijnse et al. 2021). SnapWave is a stationary spectral wave model designed to propagate offshore conditions to the nearshore, capturing refraction, shoaling, and dissipation on unstructured grids (D. Roelvink et al. 2025), and infragravity wave energy balance formulations (T. W. B. Leijnse et al. 2024). Recently, SnapWave has been extended with a vegetation module to provide vegetation dissipation terms. The coupled SFINCS-SnapWave model can therefore reproduce nearshore flooding dynamics, including wave transformation and vegetation-induced dissipation.

While the stationary mode of XBeach is conceptually closer to the wave-averaged formulation of SFINCS-SnapWave, we use the surfbeat mode (XBeach-SB) as a benchmark, since its inclusion of time-varying infragravity motions and phase-averaged hydrodynamics provides a more detailed process reference for assessing the performance of SFINCS-SnapWave.

2.5.1. XBeach-SB mode

The XBeach-SB mode describes hydrodynamics based on three main processes: wave transformation, infragravity and mean flow dynamics, and vegetation effects. These are briefly explained below, followed by a description of the source code implementation of vegetation processes. Version that is used in this thesis is XBeach v1.24 Halloween.

Wave transformation

The XBeach-SB mode solves the time-dependent sea-swell wave action balance on the scale of wave groups. These wave groups generate both steady (mean flow) and unsteady (IG wave) motions through radiation stress gradients in the nonlinear shallow-water equations (NLSWE). The wave action balance equation is given by Phillips (1977):

$$\frac{\partial A}{\partial t} + \frac{\partial c_g A}{\partial s} + \frac{\partial c_g A}{\partial \theta} = -\frac{D_w + D_v}{\sigma}, \tag{2.12}$$

where $A = \frac{E_w}{\sigma}$ is the wave action, E_w the sea-swell wave energy, σ the intrinsic wave frequency, and $c_{g,x}$ the wave group velocity in the x-direction. D_w and D_v represent energy dissipation due to wave breaking and vegetation, respectively. Wave breaking dissipation (D_w) follows J. A. Roelvink (1993), while vegetation dissipation (D_v) builds on the formulations of Mendez and Losada (2004) and the vertical layering scheme of Suzuki et al. (2012):

$$D_v = \sum_{i=1}^{n_v} D_{v,i}, \tag{2.13}$$

$$D_{v,i} = A_v \cdot \frac{\rho\, C_{D,i}\, b_{v,i}\, N_{v,i}}{2\sqrt{\pi}} \left(\frac{kg}{2\sigma}\right)^3 H_{\mathrm{rms}}^3, \tag{2.14}$$

$$A_v = \frac{\sinh^3(k\alpha_i h) - \sinh^3(k\alpha_{i-1} h) + 3\left(\sinh(k\alpha_i h) - \sinh(k\alpha_{i-1} h)\right)}{3k\cosh^3(kh)}, \tag{2.15}$$

where $C_{D,i}$ is the bulk drag coefficient, $b_{v,i}$ is stem diameter, $N_{v,i}$ the stem density, and α_i the relative vegetation height (h_v/h) for layer i. This approach links wave dissipation explicitly to vegetation geometry.

IG waves and water levels

The steady (mean setup, undertow, longshore currents) and unsteady (IG waves) motions on the scale of wave groups are solved using the depth-averaged NLSWE:

$$\frac{\partial \eta}{\partial t} + \frac{\partial (u_L h)}{\partial x} = 0 \tag{2.16}$$

$$\frac{\partial u_L}{\partial t} + u_L \frac{\partial u_L}{\partial x} = -g\frac{\partial \eta}{\partial x} + \frac{\tau_{b,x} + F_w + F_v}{\rho h}, \tag{2.17}$$

where η is water surface elevation, u_L the depth-averaged Lagrangian velocity, h the total water depth, $\tau_{b,x}$ the bed shear stress, F_w the radiation-stress-driven wave force, and F_v the vegetation force. These are consistent with the mechanisms of wave setup and vegetation drag described in Section 2.4.2, here embedded within the XBeach-SB framework.

It is noted that in the standard XBeach-SB formulation, porosity effects are ignored in the continuity and momentum equation. An optional porous in-canopy flow module is available, where porosity modifies in-canopy velocities and thus the drag force.

Vegetation influence on water level

Vegetation effects on water level are captured through two pathways: modification of the wave-induced force (F_w) via vegetation dissipation (D_v), and direct vegetation drag forces (F_v). The latter includes both the mean-flow drag ($F_{v,m}$) and the wave-related force ($F_{v,w}$). The orbital velocity u_w used in $F_{v,w}$ is reconstructed using an empirical wave shape model. XBeach also offers formulations for porous canopy flow, broadening its application for more complex cases.

Source code implementation. In the XBeach source code, vegetation processes are implemented in the module `vegetation.f90`, which contains seven subroutines (Figure 2.15). The mean-flow drag force ($F_{v,m}$) and nonlinear wave drag force ($F_{v,w}$) are computed in the `momeqveg` subroutine, with nonlinear orbital velocity u_w provided by the `swvegnonlin` routine implementing the wave shape model. Both forces are then passed to the momentum solver to update water levels.

2.5.2. SFINCS-SnapWave coupling model

This subsection describes three main processes in the SFINCS-SnapWave framework: wave transformation, infragravity (IG) and mean flow dynamics, and vegetation effects, followed by an overview of the source code implementation. The version applied in this thesis is `v2.2.1-alpha col d'Eze-branch:143`.

Wave transformation

SnapWave solves the stationary wave energy balance, a simplified form of the wave action balance under negligible currents. The model uses a single representative frequency near the spectral peak, with a fixed directional resolution and sector, to ensure computational efficiency. This allows SnapWave to simulate nearshore wave transformation processes such as shoaling, refraction, breaking, and dissipation at low cost, while providing wave forcing for SFINCS.

$$\frac{\partial E}{\partial t} + C_g \frac{\partial E}{\partial s} = -D, \tag{2.18}$$

where E is the wave energy density, C_g the group velocity, and D the total dissipation. The dissipation consists of wave breaking (D_w) (Baldock et al. 1998), bottom friction (D_b), and vegetation-induced

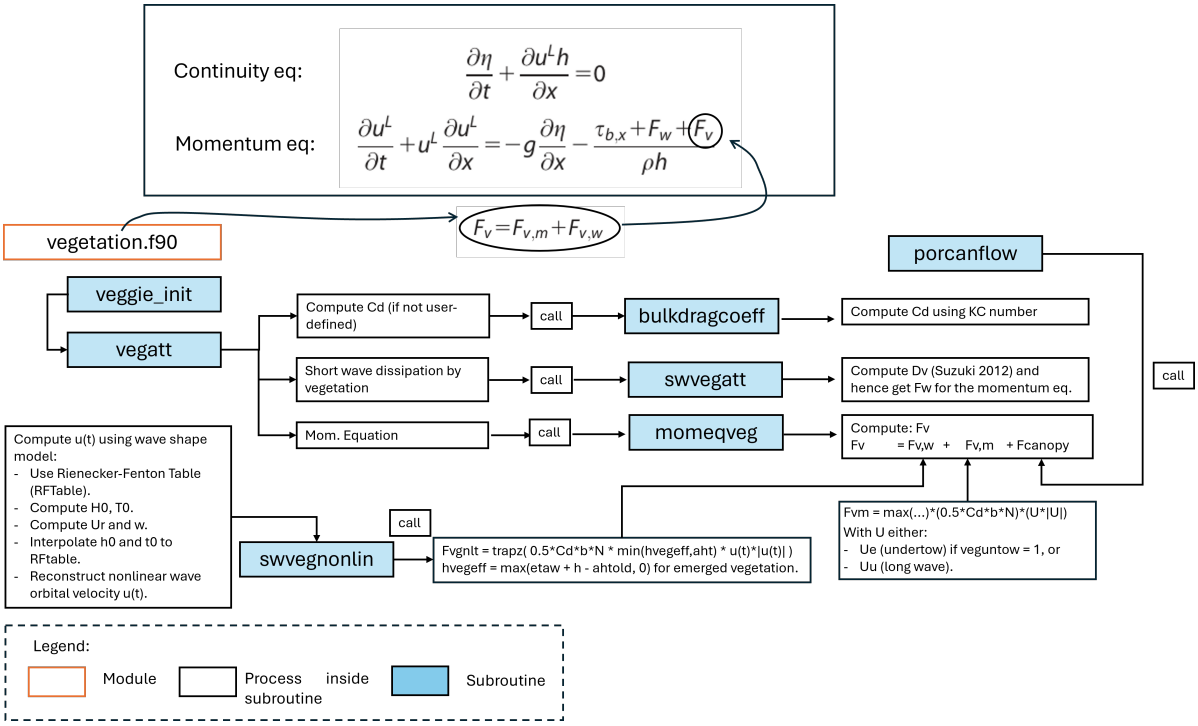

Figure 2.15: Implementation of vegetation processes in `XBeach` through the `vegetation.f90` module.

dissipation (D_v). In this latest version, vegetation dissipation is computed using the vertical layering approach of Suzuki et al. (2012), consistent with the implementation in `XBeach` (see equations 2.13–2.15).

IG waves and water levels

After resolving incident-band energy, `SnapWave` estimates IG wave evolution through a separate IG wave energy balance. Energy transfer is represented by a source term S_{ig}, acting as a sink in the incident-band balance and a source in the IG balance (T. W. B. Leijnse et al. 2024):

$$\frac{\partial c_g E_{\mathrm{inc}}}{\partial x} + \frac{\partial c_\theta E_{\mathrm{inc}}}{\partial \theta} + D_{w,\mathrm{inc}} + D_{b,\mathrm{inc}} - S_{ig} = 0, \tag{2.19}$$

$$\frac{\partial c_g E_{\mathrm{ig}}}{\partial x} + \frac{\partial c_\theta E_{\mathrm{ig}}}{\partial \theta} + D_{w,\mathrm{ig}} + D_{b,\mathrm{ig}} + S_{ig} = 0, \tag{2.20}$$

where E_{inc} and E_{ig} are the incident and IG wave energy densities, and D_w, D_b represent breaking and bottom friction dissipation. The transfer term is parameterised through a shoaling coefficient a_{ig}:

$$S_{ig} = a_{ig}\sqrt{E_{\mathrm{ig}}}\,\frac{c_g}{h}\,\frac{\partial S_{xx}}{\partial x}, \tag{2.21}$$

with $S_{xx} = (2n - \frac{1}{2})E_{\mathrm{inc}}$ the incident wave radiation stress. The coefficient a_{ig} depends on local bed slope b and relative wave height $\gamma = H_{\mathrm{rms,inc}}/h$, calibrated against `XBeach` datasets (T. W. B. Leijnse et al. 2024). The corresponding IG wave height is given by

$$H_{ig} = \sqrt{\frac{8E_{\mathrm{ig}}}{\rho g}}. \tag{2.22}$$

Water levels. For water levels and flooding, the wave forcing terms (D_w, D_b, D_v) computed in SnapWave are passed to the SFINCS momentum equations. Importantly, setup in SFINCS is based only on dissipation-derived forcing, not on radiation stress gradients. This means wave setup is represented, but set-down is not explicitly captured.

The governing depth-averaged continuity and momentum equations in SFINCS are:

$$\zeta_m^{t+\Delta t} = \zeta_m^t + \left[\frac{q_{x,m+1}^{t+\Delta t} - q_{x,m}^{t+\Delta t}}{\Delta x} + S_m \right] \Delta t, \tag{2.23}$$

$$q_x^{t+\Delta t} = \frac{q_x^t - \left(g h_x^t \frac{\Delta \zeta}{\Delta x} + adv_x - \frac{\tau_{w,x}}{\rho_w} - F_w \right) \Delta t}{1 + g \Delta t n^2 q_x^t / h_x^{7/3}}, \tag{2.24}$$

where h_x is water depth, $\tau_{w,x}$ wind stress, adv_x nonlinear advection, F_w wave forcing from SnapWave, and n Manning's coefficient.

Vegetation influence on water level

Vegetation influences wave setup in SFINCS-SnapWave only through D_v in SnapWave. Hence, vegetation alters the dissipation-derived wave forcing (F_w), but does not exert a direct drag force on the mean flow (F_v). This limitation means vegetation's effect on setup is represented, while its role in mean-flow drag remains absent.

Source code implementation. In the current version, vegetation dissipation is implemented in snapwave_solver.f90, following Suzuki et al. (2012). The resulting wave force, computed from dissipation rather than radiation stress divergence, is passed via sfincs_snapwave.f90 into the SFINCS momentum equations. This framework, illustrated in Figure 2.16, allows vegetation-modified setup to be captured but omits direct F_v contributions.

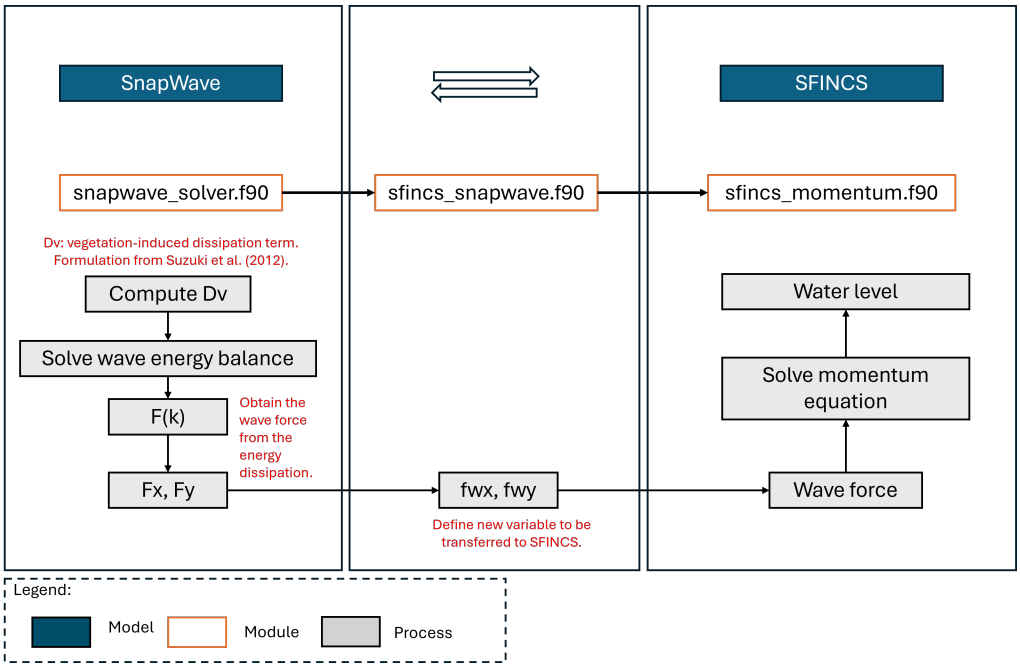

Figure 2.16: Simplified framework of the SFINCS-SnapWave coupling model including vegetation effects.

2.5.3. Remarks on XBeach-SB vs. SFINCS-SnapWave

Both the XBeach-SB and the SFINCS-SnapWave framework follow a similar principle of coupling wave processes with shallow-water flow equations to model wave-driven coastal flooding. In both cases, wave transformation and energy dissipation determine forces that drive mean flow and setup.

The key distinction lies in how the wave forcing (F_w) is generated. XBeach-SB explicitly solves a time-dependent wave action balance and directly computes spatial gradients of radiation stresses (i.e., $\partial S_{xx}/\partial x$), which enter the momentum equations as forcing terms. This allows XBeach to capture both wave setup and setdown due to shoaling, as well as dynamic infragravity (IG) motions.

In contrast, SFINCS does not solve wave equations itself. Instead, it relies on SnapWave for a stationary wave energy calculation. Here, the wave forces (F_w) are computed based purely on local energy dissipation (from breaking, bottom friction, and vegetation), rather than radiation stress gradients. As such, the default SFINCS-SnapWave implementation only represents dissipation-based setup and does not resolve setdown or dynamic IG motions. Nevertheless, recent work has demonstrated that nearshore IG wave boundary conditions estimated by SnapWave can be applied in SFINCS using its wavemaker boundary option, thereby enabling SFINCS to dynamically resolve IG wave runup and flooding (T. W. B. Leijnse et al. 2024). This distinction underlines that while SFINCS-SnapWave offers computational efficiency, it includes fewer internal wave-process details compared to XBeach-SB.

Finally, regarding vegetation, XBeach-SB incorporates vegetation effects both by modifying wave energy dissipation (affecting wave forcing F_w) and by applying a direct vegetation drag force (F_v). In contrast, SFINCS-SnapWave includes vegetation effects solely through their influence on wave dissipation and the resulting dissipation-based wave forcing (F_w).

A summary of the comparison between XBeach-SB and SFINCS-SnapWave is presented in Table 2.4.

Table 2.4: Summary of wave setup and vegetation processes in XBeach-SB and SFINCS-SnapWave

Process	XBeach-SB	SFINCS	SnapWave
Wave transformation	Wave action balance (Eq. 2.12) including vegetation dissipation term D_v	–	Wave energy equation (Eq. 2.18) including vegetation dissipation term D_v
Wave force (F_w)	Derived from radiation stress gradients	–	Computed from wave energy dissipation only
Vegetation force (F_v)	$F_v = F_{v,m} + F_{v,w}$ (Eq. 2.8); $F_{v,m}$ is due to mean flow (Eq. 2.9); $F_{v,w}$ due to wave nonlinearity (Eq. 2.10) via wave shape model	–	–
IG waves	Dynamic infragravity motions resolved via wave-group forcing	Can resolve dynamic IG runup only when forced with nearshore IG boundary conditions (wavemaker option)	Estimates stationary nearshore IG wave heights via energy balance and provides boundary conditions for SFINCS
Momentum equation	NLSWE (Eq. 2.17) with F_w and F_v	SSWE with discharge update (Eq. 2.24) including pressure, friction, and F_w	–

3

Methods

3.1. Model selection

Water level predictions are influenced by many factors, but hydrodynamics and vegetation are among the most critical. Vegetation can mitigate flooding by attenuating waves and storm surges (Temmerman et al. 2023) and by altering wave setup (even set down) (van Rooijen et al. 2016). However, vegetation–hydrodynamic interactions are complex and are often neglected or oversimplified in flood models. For example, large-scale flooding simulations commonly represent vegetation only as enhanced bed roughness (Radfar et al. 2024). While this reduces computational cost, it may also introduce substantial inaccuracies. Thus, there is a clear need for a computationally efficient flood model that can capture vegetation–hydrodynamic effects without the heavy cost of full-physics modeling.

A recent reduced-physics model is `SFINCS` (Super-Fast INundation of CoastS), which efficiently simulates compound flooding events (fluvial, pluvial, tidal, and surge-driven) with limited computational cost and good accuracy. It solves the Simplified Shallow Water Equations (SSWE), including advection in the momentum equation (T. Leijnse et al. 2021). Vegetation effects, however, are currently included only through enhanced bed roughness coefficients.

To resolve wave-driven processes, `SFINCS` requires external forcing from a wave model (T. W. B. Leijnse et al. 2024), as it does not include wave transformation internally. A recently developed stationary spectral model, `SnapWave`, addresses this by solving the wave action balance in an efficient manner (D. Roelvink et al. 2025). `SnapWave` captures essential nearshore physics such as refraction, shoaling, and dissipation, and now also incorporates vegetation-induced dissipation following the vertical layering approach of Suzuki et al. (2012).

The coupled `SFINCS-SnapWave` model therefore offers an efficient framework to simulate large-scale, multi-driver flooding with vegetation influence. Its current limitation is that vegetation acts only through dissipation in `SnapWave`, without explicit vegetation drag in `SFINCS`. This thesis applies `SFINCS-SnapWave` to evaluate its ability to reproduce vegetation effects on coastal flooding and proposes improvements to enhance vegetation representation while maintaining computational efficiency.

3.2. Approach

To address the research objectives formulated in Chapter 1, a stepwise approach is designed, consisting of two main parts: (i) model evaluation and (ii) model improvement. This structure allows the current `SFINCS-SnapWave` framework to be validated against existing benchmark models and laboratory data, followed by targeted enhancements to improve vegetation representation. The workflow is illustrated in Figure 3.1.

3.2.1. Model evaluation

In the evaluation step, the `SFINCS-SnapWave` model is configured to reproduce the laboratory flume experiments of Wu et al. (2011), previously modelled with `XBeach-SB` by van Rooijen et al. (2016).

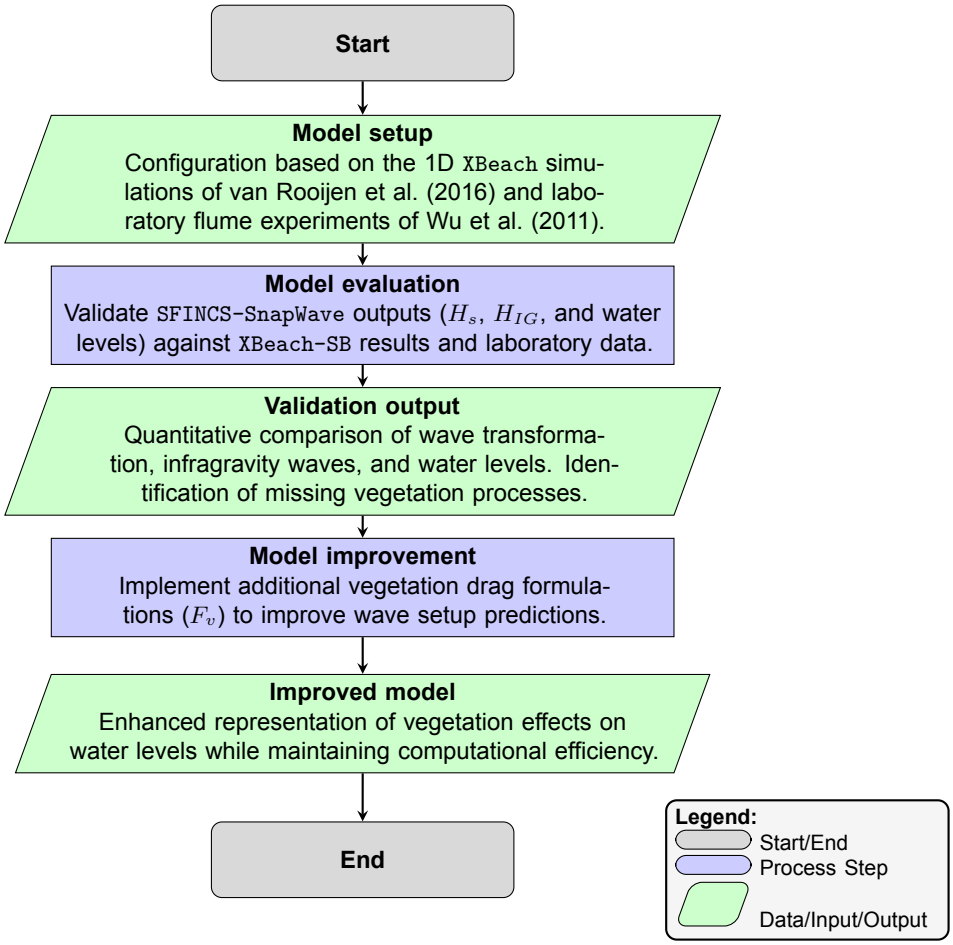

Figure 3.1: Workflow for evaluation and improvement of the SFINCS-SnapWave model to capture vegetation effects on wave setup.

The configuration consists of a bed slope with vegetation in a flume scale, induced by wave forcing with varying offshore significant wave height (H_s) and peak period (T_p). The model performance is assessed by comparing significant wave heights (H_s), infragravity wave heights (H_{IG}), and mean water levels (wave setup) along the cross-shore transect against both experimental observations and XBeach-SB simulations. This step identifies the extent to which SFINCS-SnapWave can reproduce observed vegetation–wave interactions and highlights missing processes that limit its accuracy.

3.2.2. Model improvement

The model evaluation highlights a key limitation of SFINCS-SnapWave: vegetation effects are currently included only via energy dissipation (D_v), without explicit vegetation drag forces (F_v). As shown in Chapter 2, the vegetation drag force is crucial for accurately reproducing wave setup, especially the nonlinear wave drag component $F_{v,w}$ (van Rooijen et al. 2016). Therefore, the proposed improvement strategy in this study focuses on extending the SFINCS-SnapWave framework by explicitly incorporating F_v.

The vegetation drag force consists of two components:

- $F_{v,w}$: vegetation drag due to nonlinear wave orbital velocities,
- $F_{v,m}$: vegetation drag due to mean (undertow) and infragravity flows.

In wave-dominated conditions, $F_{v,w}$ is expected to dominate over $F_{v,m}$, and is therefore prioritised in this implementation. The $F_{v,m}$ contribution can partly be approximated by enhanced bed roughness, but $F_{v,w}$ is entirely absent in the current model. The improvement framework is illustrated in Figure 3.2.

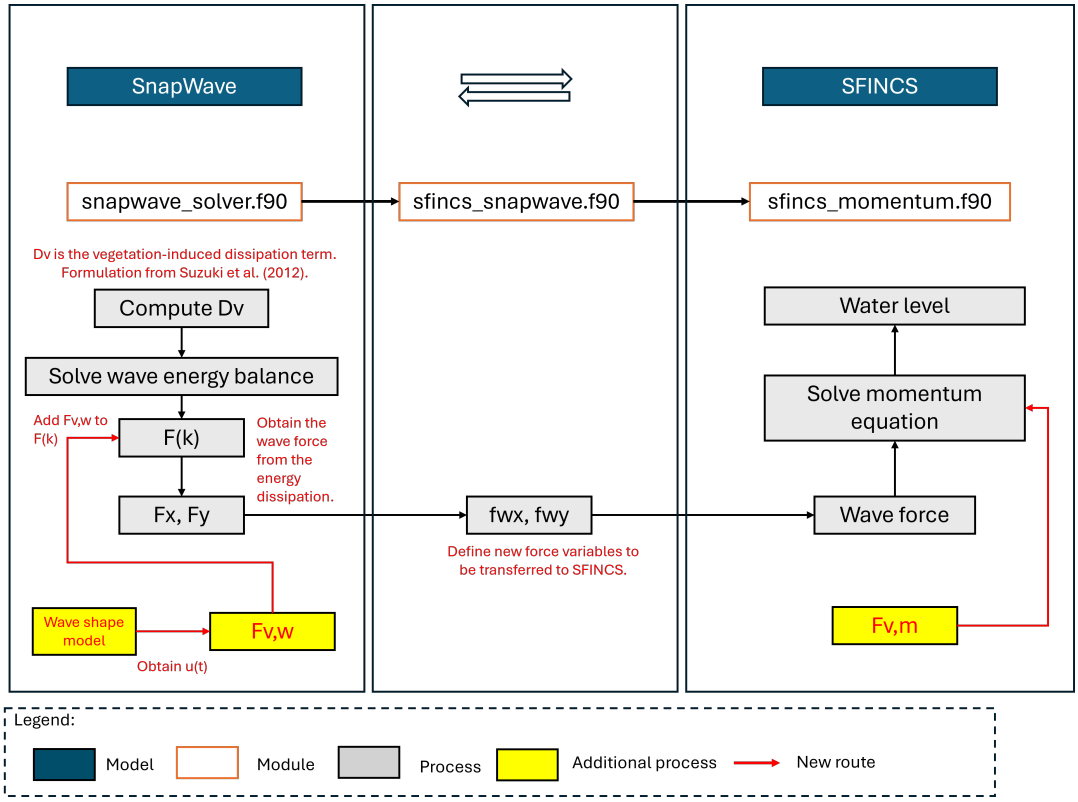

Figure 3.2: Proposed improvement of `SFINCS-SnapWave` coupling framework including explicit vegetation drag forces.

Implementation of $F_{v,w}$ in `SnapWave`

The nonlinear wave drag force $F_{v,w}$ depends only on wave parameters and vegetation geometry, making it suitable to implement within the `SnapWave` module. Two new subroutines are proposed in `snapwave_solver.f90`:

- `swvegnonlin`: computes the nonlinear orbital velocity (u_{nl}) using the wave shape model.
- `momeqveg`: computes $F_{v,w}$ from u_{nl}, vegetation parameters (C_D, b_v, N_v, h_v), and water density.

The computed $F_{v,w}$ is then integrated into the existing `solve_energy_balance2Dstat` subroutine, where it enters the wave forcing $F(k)$. This approach mirrors the structure of `XBeach` while remaining computationally efficient. Figure 3.3 summarises this proposed implementation.

Implementation of $F_{v,m}$ in `SFINCS`

The mean-flow vegetation drag $F_{v,m}$ directly depends on depth-averaged flow velocity and is therefore implemented inside the `SFINCS` solver. Within `sfincs_momentum.f90`, the `compute_fluxes` subroutine already evaluates forcing terms such as pressure gradients, wind stress, and bed shear. Here, $F_{v,m}$ is added as an additional quadratic drag term, allowing explicit computation of vegetation drag rather than being implicitly absorbed into bottom friction. Figure 3.4 shows the proposed structure. Due to the focus of this study on implementing the $F_{v,w}$ component, this proposed $F_{v,m}$ implementation is indeed important to be applied for future model enhancement.

Summary

By implementing $F_{v,w}$ in `SnapWave` and $F_{v,m}$ in `SFINCS`, the improved model captures both nonlinear wave drag and mean-flow drag effects of vegetation. This enhancement addresses a key gap in the current `SFINCS-SnapWave` framework. This improvement is expected to enhance the water level prediction due to coastal forcing while maintaining computational efficiency, and thus can be applied for large-scale multi-driven coastal flooding simulations.

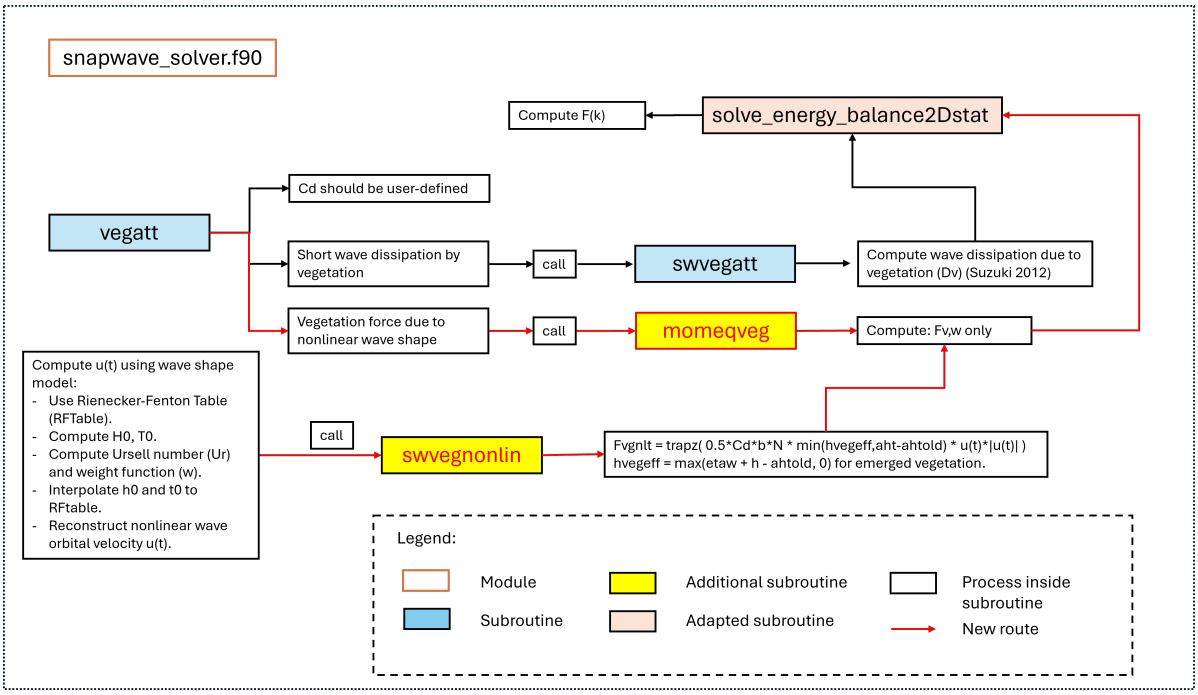

Figure 3.3: Proposed $F_{v,w}$ vegetation effect implementation in `snapwave_solver.f90`.

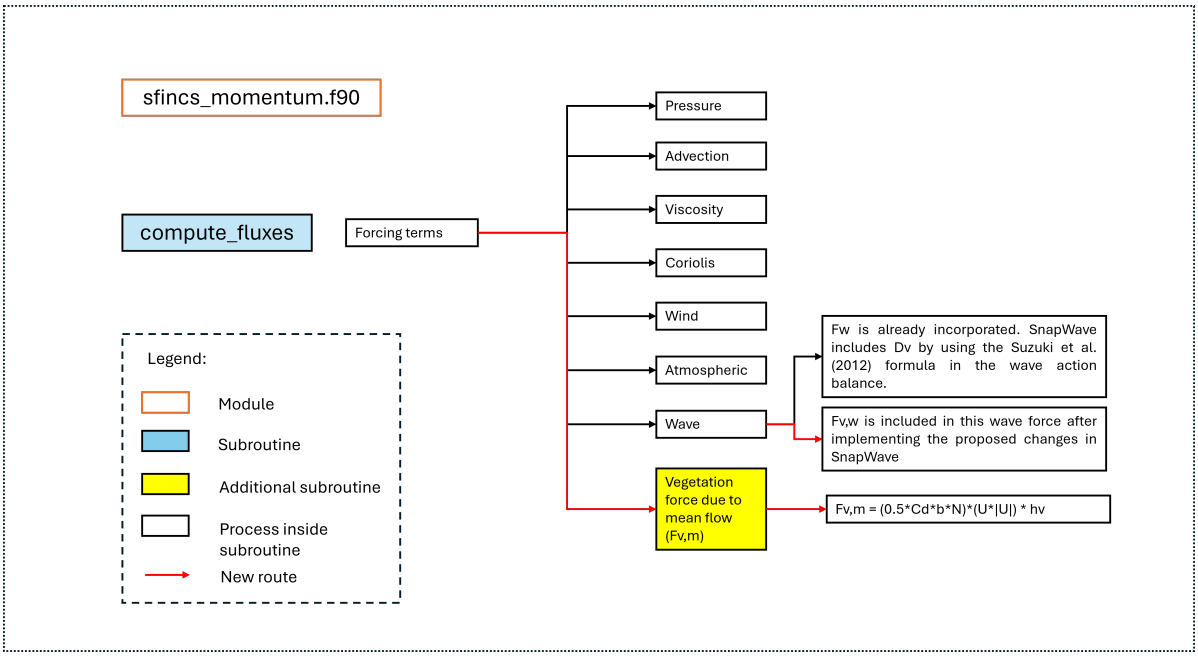

Figure 3.4: Proposed $F_{v,m}$ vegetation effect implementation in `sfincs_momentum.f90`.

4

Model evaluation and improvement

This chapter presents the results of the SFINCS-SnapWave model evaluation and improvement using version v2.2.1-alpha col d'Eze-branch:143. First, the configuration of the model and the scenarios are described, including parameter selection and assumptions following the modelling study of van Rooijen et al. (2016). Next, the results of the model evaluation are presented by validating the SFINCS-SnapWave outputs against laboratory flume data (Wu et al. 2011) and XBeach-SB results (van Rooijen et al. 2016), for both with-vegetation and without-vegetation cases. After identifying the model's main limitation related to vegetation effects on water levels, improvements are introduced, producing a new version called v2.2.1-alpha col d'Eze-branch:143_veg_fvw. This improved model is then validated against the same benchmark data as in the previous evaluation stage. For clarity, the current version of SFINCS-SnapWave is referred to as the "baseline model", while the modified one is called the "improved model".

4.1. Model configuration and scenarios

The laboratory experimental setup of Wu et al. (2011) consisted of a wave flume measuring 20.6 m in length, 0.69 m in width, and 1.22 m in depth. A ramp with a slope of 1/7 is installed in front of the wave generator, extending from $x = 0$ to $x = 2$ m. However, in the XBeach-SB model by van Rooijen et al. (2016), this ramp was excluded, and the model domain started from $x = 2$ m. To ensure comparability between models, the SFINCS-SnapWave model also adopts this configuration. A horizontal false floor was installed at elevation $z = -0.4$ m, transitioning into a 1/21 sloping bed starting at $x = 7.2$ m. The still water level was maintained at elevation $z = 0$ m.

Vegetation elements were introduced in the flume between $x = 11.5$ m and $x = 15.1$ m, represented by rigid cylinders with a height (h_v) of 0.20 m, a diameter (b_v) of 3.2 mm, and a density (N_v) of 3182 stems per square meter. The drag coefficient (C_D) was set to 1.7, consistent with van Rooijen et al. (2016) study. The experimental layout is shown in Figure 4.1.

The SFINCS-SnapWave model was configured with boundary conditions to replicate both the flume experiment and the previous XBeach-SB model. A water level boundary (Dirichlet B.C.) of $\eta = 0$ m was applied at the left edge (representing the start of the flume), while an outflow boundary condition (Neumann B.C.) was applied elsewhere. Due to differences in default settings between XBeach-SB and SFINCS-SnapWave, several parameters required adjustment. First, the bed roughness was converted from Chezy ($C = 51.6$, with $c_f = 0.003$) to Manning ($n \approx 0.015$). Second, regarding wave breaking, since XBeach applies $H_{max} = \gamma h$ while SnapWave approximates $H_{max} \approx 0.88\gamma h$ in shallow water, we set $\gamma_{\text{snapwave}} = \gamma_{\text{xbeach}}/0.88$ to ensure equivalent breaking thresholds.

A total of twelve validation scenarios were simulated with varying significant wave height (H_s), peak wave period (T_p), and vegetation presence. In the XBeach-SB simulations of van Rooijen et al. (2016), wave forcing was applied using a JONSWAP spectrum with a peak enhancement factor (γ_{jsp}) of 3.3. In contrast, the SnapWave model used a stationary wave solver with a parameterised frequency spectrum represented by a single frequency close to the peak frequency (D. Roelvink et al. 2025).

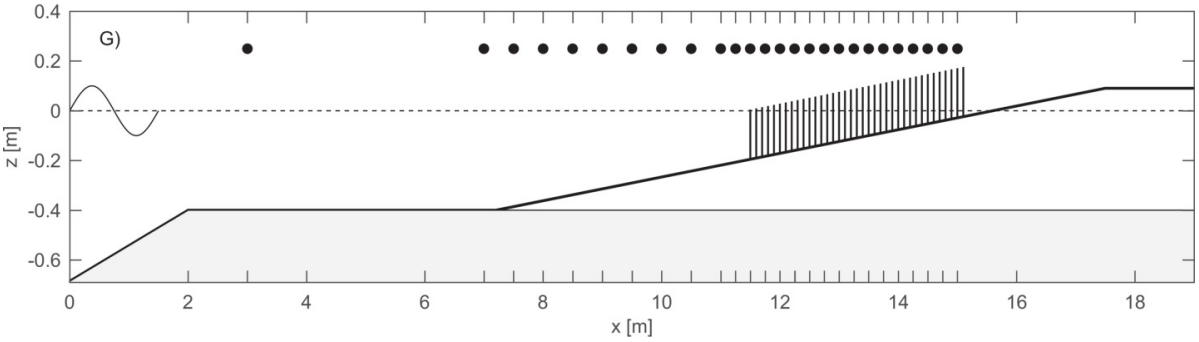

Figure 4.1: Schematic of the experimental setup used in the wave flume study of Wu et al. (2011), adapted from van Rooijen et al. (2016). The setup shows the wave generator (left boundary), the sloping beach, the false floor, and the vegetated section. The dots along the x-axis indicate wave gauge positions.

Table 4.1 presents the variation of offshore H_s and T_p for each scenario. The outputs of these simulations are significant wave height (H_s), infragravity-band wave height (H_{IG}), external force (F_x), and mean water level (η), plotted along the cross-shore profile.

Scenario	H_s (cm)	T_p (s)	Vegetation
S1–S2	3.7	1.2	Without / With
S3–S4	4.7	1.6	Without / With
S5–S6	5.4	1.2	Without / With
S7–S8	5.5	1.8	Without / With
S9–S10	7.4	1.6	Without / With
S11–S12	6.7	2.4	Without / With

Table 4.1: Wave setup scenarios based on Wu et al. (2011) and van Rooijen et al. (2016).

4.2. Model evaluation

In this section, scenarios S11 (without vegetation) and S12 (with vegetation) are discussed individually as representative examples to understand the physics of wave transformation, wave force generation, and water-level changes. These particular scenarios are explained extensively in van Rooijen et al. (2016), which facilitates a more detailed analysis of the model results in this study. The comparison results are presented in Figure 4.2, comparing the results of `SFINCS-SnapWave` baseline model and `XBeach-SB` against the measurements of Wu et al. (2011). For assessing overall performance across all scenarios, statistical evaluation using bias and scatter index is performed by plotting model results and measurements along the flume in Figure 4.4. Lastly, Appendix D shows the supplementary results that provide more detailed modelling results across all scenarios.

4.2.1. Measurement data description

This subsection describes the measurement data of Wu et al. (2011), which contains significant wave height and mean water level. In the case without vegetation (black dots in Figure 4.2), the measured wave height shows cross-shore transformation: shoaling followed by energy dissipation due to breaking as the local water depth decreases. The measured mean water level shows a somewhat noisy pattern between $x = 8$ m and $x = 14$ m. However, the general behaviour is clear: a slight decrease of water level (set-down) in the shoaling zone, followed by a sharp rise (set-up) in the breaker zone.

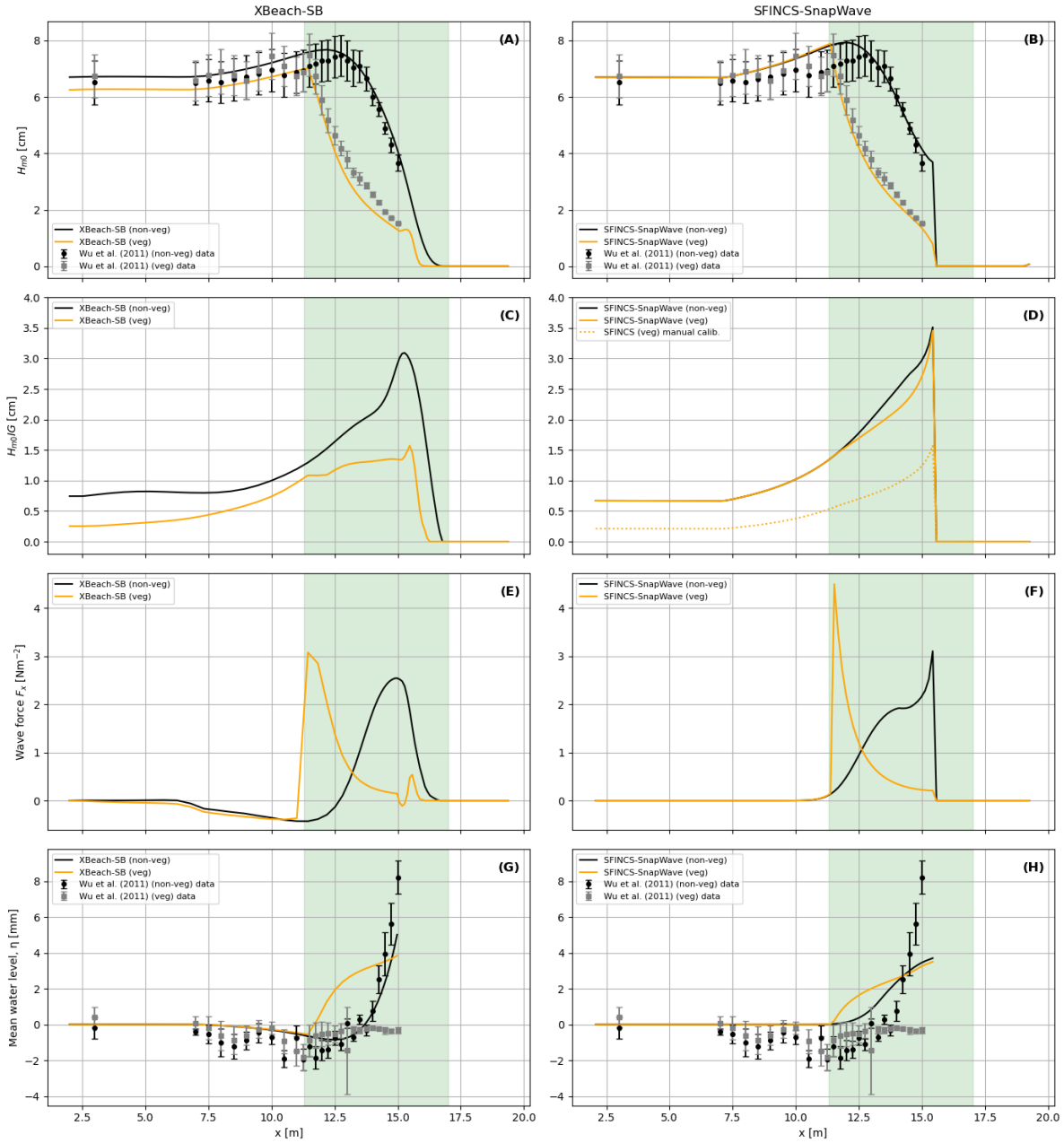

Figure 4.2: Cross-shore evolution from `XBeach-SB` (left) and `SFINCS-SnapWave` (right) for non-vegetated (black line) and vegetated (orange line) cases. Panels (A–B): H_{m0} [cm]; (C–D): IG-band H_{m0} [cm]; (E–F): wave force F_x [N m^{-2}]; and (G–H): mean water level η [mm]. Wu et al. (2011) data are shown as black circles (non-veg) and grey squares (veg). The vegetated zone is shaded green.

In the case with vegetation (grey dots in Figure 4.2), the measured wave height is dissipated earlier by vegetation, before the breakpoint is reached. This results in much lower wave heights already in relatively deeper water. The measured mean water level is much lower than in the non-vegetated case, with a gradual set-down in the shoaling region and hardly any set-up after the breaker zone.

4.2.2. Baseline model comparison

The performance of the `SFINCS-SnapWave` model is assessed in comparison to the measurements and the `XBeach-SB` results. The comparison is presented in two parts: without-vegetation and with-vegetation cases.

Without vegetation. In the case without vegetation (black lines in Figure 4.2), the significant wave height (first row) is slightly overestimated in the surf zone by both SFINCS-SnapWave and XBeach-SB. Nevertheless, both models capture the breaking location reasonably well compared to the measurements. At the end of the domain, SFINCS-SnapWave shows an unrealistic sharp drop of wave height to zero, whereas XBeach-SB reproduces a smoother decay. The IG wave height (second row) is very similar between SFINCS-SnapWave and XBeach-SB, increasing from about 0.8 cm to a peak of around 3.2 cm. Note that there are no measurement data for IG wave height; hence, only inter-model comparison is possible.

The wave force (third row) shows the expected gradual increase around the breaking point, with similar peak magnitudes of about 3 N m^{-2} for both models. However, XBeach-SB captures more detailed processes, such as negative (offshore-directed) wave force in the shoaling zone. This is physically expected as the radiation-stress gradient increases during shoaling. SFINCS-SnapWave does not capture this because its wave force is computed from wave dissipation only, which reflects negative energy gradients, whereas XBeach-SB explicitly computes radiation stresses. This difference in wave-force formulation may also affect the mean water level.

The mean water level (fourth row) in XBeach-SB exhibits the typical set-down in the shoaling zone and set-up in the breaker and surf zones. In contrast, SFINCS-SnapWave does not capture the set-down during shoaling because its wave forcing derives only from local dissipation, not from the gradient of radiation stress. Additionally, it yields a milder nearshore set-up than both the measurements and XBeach-SB.

With vegetation. In the case with vegetation (orange lines in Figure 4.2), the SFINCS-SnapWave model shows good agreement with the measured significant wave height (first row), reproducing the shoaling and breaking zones as well as the cross-shore variation. This supports the reliability of SnapWave in simulating wave transformation over vegetated foreshores under these experimental conditions. It is noted that the XBeach-SB simulations here show a slight reduction in wave height already at the offshore boundary, possibly due to temporal averaging of H_{m0}, whereas SnapWave provides a stationary solution. Overall, SnapWave agrees well with the measurements, while XBeach-SB is used as a qualitative reference.

For IG waves (second row), XBeach-SB clearly shows vegetation influence, with a reduction in the peak by approximately 50% relative to the non-vegetated scenario, indicating substantial attenuation of IG energy within the model framework. In contrast, SFINCS-SnapWave does not capture this peak reduction. A plausible explanation is that SnapWave primarily estimates incoming IG energy without resolving reflected components and vegetation–IG interactions. To approximate this effect for this particular case, a manual calibration was carried out by reducing the incident wave energy transferred to the IG wave height and reducing the multiplication factor for the IG shoaling source/ sink term. As illustrated by the dotted orange line in Figure 4.2 (D), these adjustments enable the model to better replicate the peak IG wave height reduction observed in the XBeach-SB simulations. Nevertheless, this calibration may not be generally applicable to all cases, due to limited measurement data. Furthermore, the understanding of the influence of vegetation in attenuating IG wave is still limited, thus this might need more attention in separate study. Thus, in this study, the broader influence of vegetation on IG waves in SFINCS-SnapWave still cannot be reliably captured.

Wave force (third row) in the vegetated case shows similar patterns between SFINCS-SnapWave and XBeach-SB, with a rapid increase at the start of the vegetated field, as expected due to the sharp decrease in wave height (and thus energy) there. However, as in the non-vegetated case, SFINCS-SnapWave does not capture the offshore-directed force in the shoaling zone. Consequently, the peak wave force in SFINCS-SnapWave (about 4.5 N m^{-2}) is higher than in XBeach-SB (about 3.1 N m^{-2}).

For the mean water level, both SFINCS-SnapWave and XBeach-SB considerably overpredict the nearshore values. While the measurements indicate hardly any wave setup, both models produce substantial setup up to about 4 mm (nearly four times too high in this case). This discrepancy arises because the models do not account for nonlinear wave-shape effects on vegetation force ($F_{v,w}$) in these runs, even though vegetation energy dissipation is included in the wave force. The vegetation-related force component $F_{v,w}$ in Equation 2.8—which is expected to add an offshore-directed contribution and thus

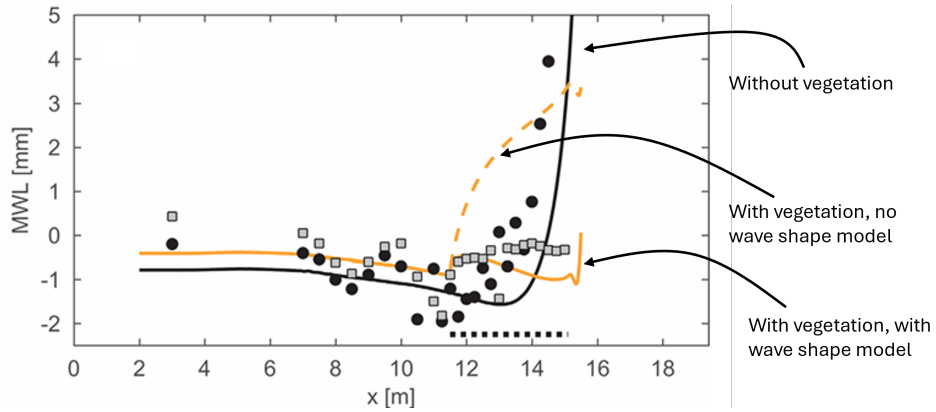

Figure 4.3: XBeach-SB mean water level based on van Rooijen et al. (2016). When the wave-shape model is activated, the nearshore setup becomes much lower than in the XBeach-SB runs of this study, likely due to model-version differences.

reduce setup—is not represented.

In XBeach-SB, however, there is an option to include this effect via wave shape model, which represents the impact of nonlinear waves on vegetation drag. When activated, the model yields a much closer prediction of the nearshore mean water level. This is illustrated in Figure 4.3, where the estimated water level in the vegetated case agrees far better with the measurements, showing very low setup (and in places, mainly set-down). Attempts to reproduce the XBeach-SB wave-shape simulation results were made, but the outcomes did not perfectly match the original paper, likely due to version differences and exploring XBeach-SB versions is beyond the scope of this study. Nevertheless, this underlines the importance of the vegetation drag force due to nonlinear wave shape ($F_{v,w}$) in simulating wave setup. Unfortunately, SFINCS-SnapWave presently lacks a similar capability to incorporate this vegetation force contribution.

4.2.3. Baseline model statistical performance

To evaluate overall performance across all scenarios, statistical evaluation is performed using two metrics: the scatter index (SI) and bias. The SI quantifies the relative spread of model predictions around the observations, normalised by the mean of the observed values, while the bias indicates systematic over- or underestimation. Figure 4.4 shows the comparison between model results and laboratory measurements of significant wave height and mean water level, evaluated along the flume (at locations indicated by black dots in Figure 4.1) and across all scenarios in Table 4.1.

Overall, the statistical results demonstrate that SFINCS-SnapWave accurately reproduces significant wave height (H_{m0}) under both non-vegetated and vegetated conditions. For the non-vegetated cases, SFINCS-SnapWave yields a very low SI of 0.09 and a small positive bias of 0.21, indicating close agreement with the measurements. Under vegetated conditions, the model also shows very low scatter (SI = 0.07) and a slight overestimation (bias = 0.04). These values are comparable to the performance of XBeach-SB.

For the mean water level in the non-vegetated cases, SFINCS-SnapWave shows reasonable agreement (SI = 1.25; bias = 0.45), comparable to XBeach-SB (SI = 0.98; bias = -0.12), although SFINCS-SnapWave has a slightly higher positive bias. This arises from overprediction in deeper regions and the inability to capture set-down during shoaling. This pattern is evident from the absence of values below zero on the SFINCS-SnapWave mean-water-level axis.

Under vegetated conditions, both models deviate more from the measurements. SFINCS-SnapWave shows SI = 3.52 and bias = 0.70, similar to XBeach-SB without the wave-shape model (SI = 4.07; bias = 0.70), indicating a strong overprediction of mean water level. Incorporating the wave-shape model in XBeach-SB substantially reduces both SI and bias (as reported by van Rooijen et al. (2016): SI = 0.072; bias = 0.179), emphasising the importance of accounting for nonlinear wave effects when predicting setup in vegetated conditions.

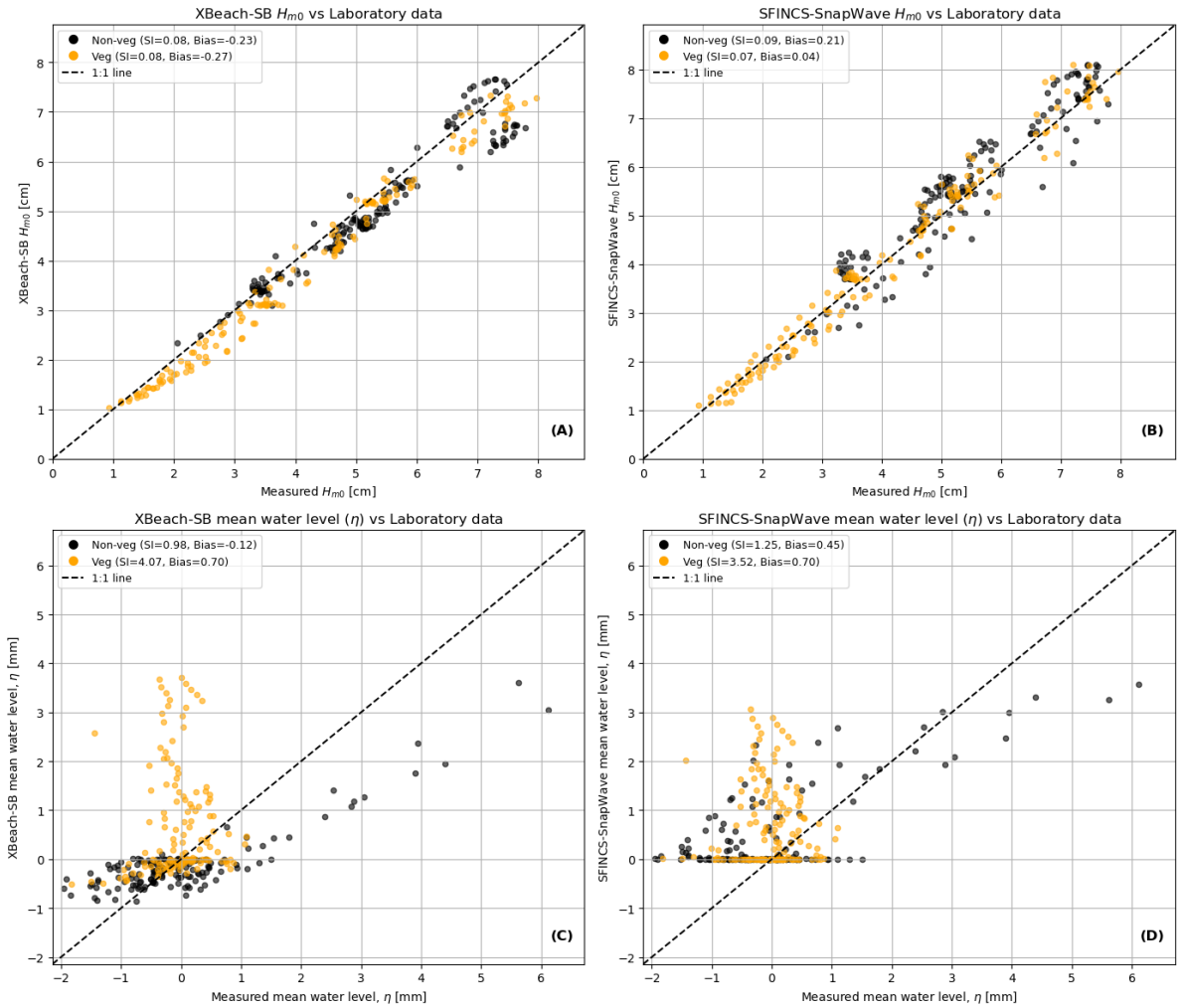

Figure 4.4: Scatter plots comparing modelled and measured significant wave height (H_{m0}) and mean water level along the wave flume across all scenarios. Top panels show H_{m0} for `XBeach-SB` (left) and `SFINCS-SnapWave` (right); the lower panels show mean water level. Black, orange, and blue markers indicate non-vegetated, vegetated, and wave-shape cases, respectively. Legends report SI and bias; the dashed line represents perfect agreement (1:1).

4.2.4. Baseline model limitations

There are at least four important `SFINCS-SnapWave` limitations, based on the validation results and literature, that may affect water-level prediction under coastal flooding in vegetated regions.

First, `SFINCS-SnapWave` strongly overpredicts mean water level in vegetated areas (Figure 4.2H) with a bias of 0.70 across all scenarios (Figure 4.4). This is expected due to the missing vegetation-force contribution from wave nonlinearity ($F_{v,w}$). The pattern mirrors `XBeach-SB` without the wave-shape option and improves substantially when $F_{v,w}$ is included. Hence, $F_{v,w}$ is a particularly important process in these wave-dominated experimental settings.

Second, `SFINCS-SnapWave` cannot capture the set-down that occurs when waves begin shoaling. The lowest mean water level in `SFINCS-SnapWave` is always zero in all cases (see Figure 4.4, bottom right). In reality, set-down is expected during shoaling prior to breaking, and this is captured by `XBeach-SB`. `SFINCS-SnapWave` does not capture this because wave forcing stems only from energy dissipation, not from radiation-stress gradients. Thus, when waves gain energy while shoaling, there is no offshore-directed wave force yet, and no set-down is produced. Wave force appears only once dissipation starts, which then drives set-up.

Third, `SFINCS-SnapWave` neglects the vegetation drag force due to mean flow ($F_{v,m}$). In this wave-dominated experiment, the effect of $F_{v,m}$ is not evident because mean flows are very small. Neverthe-

less, this absence is important for broader applications, such as surge-dominated cases. Optionally, higher bed roughness can be used to represent additional drag.

Lastly, IG waves produced by SFINCS-SnapWave do not capture vegetation effects. While the understanding of vegetation–IG interactions is still limited, SFINCS-SnapWave hardly introduces any IG attenuation due to vegetation, whereas XBeach-SB does. This is because the IG-wave estimate in SnapWave depends on the IG and incident energy balance and only accounts for incoming waves as the boundary condition in SFINCS.

Evaluating these limitations from both the literature and the validation, the vegetation force due to wave nonlinearity ($F_{v,w}$) emerges as the most important process to include in SFINCS-SnapWave when waves are present. Neglecting this effect can overestimate mean water level in vegetated areas by up to a factor of four in S12. This component is currently absent from the model yet is demonstrably important in wave-dominated settings. The next section discusses the implications of implementing $F_{v,w}$ in the improved SFINCS-SnapWave model.

4.3. Model improvement

To enhance the prediction of water levels influenced by vegetation, the SFINCS-SnapWave model is improved by implementing the vegetation force due to wave nonlinearity ($F_{v,w}$) using the approach presented in Chapter 3. In this section, the rationale for the improvement is explained. Next, the results of the improved model are presented, followed by an evaluation of the statistical performance across all scenarios.

4.3.1. Improvement implementation

To include the vegetation force due to wave nonlinearity ($F_{v,w}$) in SnapWave, two processes are added. First, computation of the vegetation force $F_{v,w}$ itself as expressed in Equation 2.10. Second, application of the wave-shape model to compute the nonlinear wave orbital velocity (u_w). These two processes are implemented as separate subroutines inside the snapwave_solver.f90 module, as presented in Figure 3.3.

Computation of $F_{v,w}$

The computation of $F_{v,w}$ is applied in a subroutine called momeqveg. This subroutine solves Equation 2.10 and assesses the contribution per vertical layer. The detailed coding documentation can be found in Appendix C.1. For completeness, the formula for $F_{v,w}$ is:

$$F_{v,w} = \int_0^{T_{\mathrm{rep}}} \frac{1}{2}\,\rho\, C_D\, b_v\, N_v\, h'_v\, u_w(t)\,|u_w(t)|\,dt. \tag{4.1}$$

The constant vegetation parameters (C_D, b_v, and N_v) can be used directly as defined in SnapWave; however, two variables—nonlinear wave orbital velocity (u_w) and effective submerged vegetation height (h'_v)—are not yet defined. The vegetation height (h_v) is defined, but it does not account for water depth. Therefore, the submerged vegetation height (h'_v) is estimated as the minimum of vegetation height (h_v) and still-water depth (h):

$$h'_v = \min(h_v,\, h). \tag{4.2}$$

Using the above approach, the effect of vegetation emergence in h'_v is not considered. In reality, if vegetation is emerged, the submerged vegetation height (h'_v) varies over the wave cycle due to free-surface oscillation. This is expected to add an offshore-directed contribution to $F_{v,w}$, as explained in Chapter 2.4.2. As a comparison, XBeach-SB also implements this emergence effect. The approach is:

$$h'_v(t) = \min\big(h_v,\, \eta_w(t) + h\big). \tag{4.3}$$

In this study, Equation 4.2 is chosen not only for simplicity, but also to remain conservative. It is found that applying Equation 4.3 mainly underestimates the water levels (see Appendix D). This is later discussed in Chapter 5.

Thus, to obtain $F_{v,w}$, computation of nonlinear wave orbital velocity (u_w) over a wave period is essential. Reconstruction of u_w is implemented in a separate subroutine by applying the wave-shape model.

The wave-shape model application

The wave-shape model is applied in subroutine `swvegnonlin`. It is used to account for the nonlinear wave orbital velocity (u_w) required for the $F_{v,w}$ calculation. Similar to the approach of Vries (2009), this method builds on the wave-shape description of Rienecker and Fenton (1981) and applies the empirical formulation by Ruessink et al. (2012) to reconstruct depth-averaged orbital-velocity time series (u_w) over a wave period. The detailed coding implementation can be found in Appendix C.4, following the `XBeach-SB` approach.

Following Rienecker and Fenton (1981), the sea–swell wave shape is reconstructed as a weighted sum of eight sine and cosine harmonics:

$$u_w(t) = \sum_{i=1}^{8} \Big[w\, A_i \cos(i\omega t) + (1-w)\, A_i \sin(i\omega t) \Big], \tag{4.4}$$

where u_w is the orbital velocity, A_i is the amplitude of the i-th harmonic, ω is the angular frequency, and w is a weighting function.

The harmonic amplitudes A_i are determined using a precomputed Rienecker–Fenton (RF) lookup table developed from stream-function wave theory (Rienecker and Fenton 1981). This table provides near-bed velocity amplitudes A_i for a range of nondimensional wave heights ($H_0 = H_{rms}/h$) and nondimensional periods ($T_0 = T_p\sqrt{g/h}$).

The weighting function (w) follows an empirical relationship that accounts for wave nonlinearity as a function of the Ursell number (U_r) and phase ϕ based on Ruessink et al. (2012):

$$w = 1 - \frac{\phi}{\pi}, \tag{4.5}$$

$$\phi = \frac{\pi}{2}\left(1 - \tanh\left(\frac{0.815}{U_r^{0.672}}\right)\right), \tag{4.6}$$

$$U_r = \frac{3}{8}\,\frac{H_{m0}\,k}{(kh)^3}. \tag{4.7}$$

Given that `SnapWave` resolves the significant wave height (H_{m0}) and peak period (T_p), this approach can be used to reconstruct the nonlinear orbital velocity (u_w). Moreover, it can be extended to obtain the free-surface oscillation (η_w) and thereby determine the effective submerged vegetation height $h'_v(t)$ in Equation 4.3, using:

$$\eta_w(t) = u_w(t)\,\sqrt{h/g}. \tag{4.8}$$

4.3.2. Improved model results

To evaluate the improved model, we compare against the Wu et al. (2011) measurements. Figure 4.5 shows `SFINCS-SnapWave` results for significant wave height, the decomposed external forcing (wave force F_w and vegetation force due to wave nonlinearity $F_{v,w}$), and mean water level, for both non-vegetated and vegetated cases. IG-wave results are omitted here, as the focus is on how $F_{v,w}$ modifies the mean water level. Consistent with the baseline evaluation, scenarios S11 and S12 are discussed individually, while the aggregate performance over all scenarios is quantified with statistical indices later.

The improved `SFINCS-SnapWave` model introduces the forcing $F_{v,w}$ alongside the existing F_w forcing. As outlined in Chapter 2, F_w is primarily onshore-directed (driving set-up), whereas $F_{v,w}$ adds an offshore-directed contribution (driving set-down). The magnitude and sign of $F_{v,w}$ follow the nonlinearity of the wave orbital velocity $u_w(t)$ (Equation 2.10): for a symmetric (non-skewed) waveform the wave-cycle integral vanishes, but as waves shoal and become skewed, the reconstructed $u_w(t)$ from the wave-shape model results a net $F_{v,w}$. In Figure 4.5D, this appears as a blue dashed curve opposing the orange dashed F_w. Near the vegetation front, rapid dissipation increases F_w, while the strong

nonlinearity of u_w simultaneously increases $F_{v,w}$ in the opposite direction; further shoreward, both the orbital velocity and the effective submerged plant height decrease with depth, so $F_{v,w}$ weakens. Their sum gives the total external force F_x (red line).

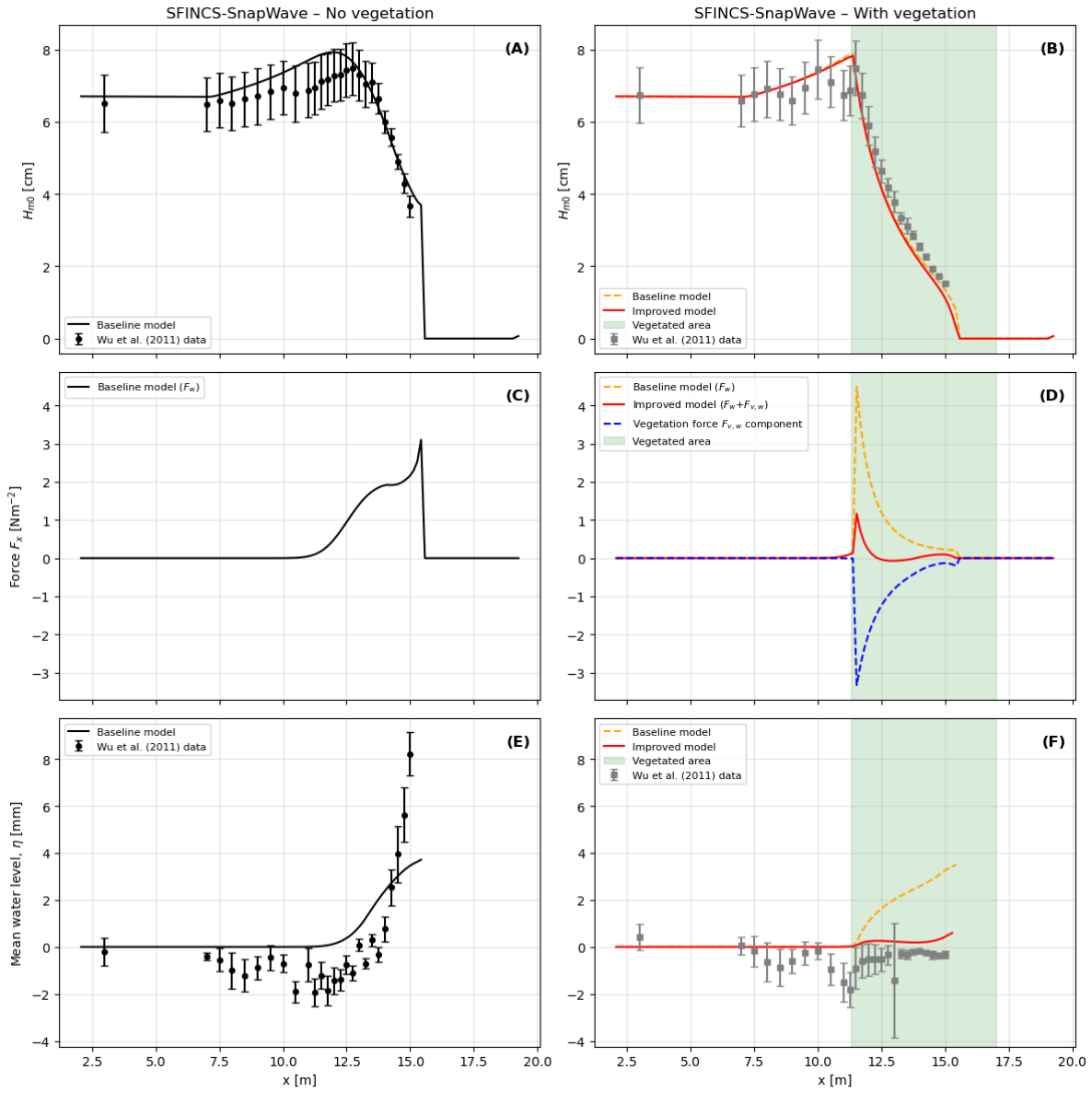

Figure 4.5: Cross-shore evolution from `SFINCS-SnapWave`, with the left column showing the non-vegetated case and the right column the vegetated case with Wu et al. (2011) observations (black circles: non-veg; grey squares: veg). Panels (A–B) show significant wave height H_{m0} [cm]. Panels (C–D) give the external force F_x [N m^{-2}]. Specifically, panel (D) decomposes the vegetated-case force into wave force F_w (orange dashed), vegetation force due to wave nonlinearity $F_{v,w}$ (blue dashed), and their sum $F_w+F_{v,w}$ (red solid). Panels (E–F) show mean water level η [mm] with observations. The vegetated zone is shaded green.

The reduced net forcing translates into a lower wave setup throughout the vegetated field. From the 1D momentum balance (Equation 2.6), the water-level slope scales with F_x and inversely with depth. Cross-shore towards the end of the vegetated zone, two tendencies compete: (i) F_x decreases (which would flatten or lower the setup), while (ii) the water depth also decreases (which would steepen the setup). In the improved run, the first effect dominates early in the vegetated section, yielding a much milder rise than in the baseline; thereafter the two effects nearly balance, producing a nearly constant mean water level across the vegetation (Figure 4.5F, red). This lower setup feeds back into the wave field: when `SFINCS` passes the updated water level to `SnapWave`, the slightly reduced depth increases

bottom-friction dissipation and marginally lowers H_{m0} in the vegetated region. The coupled change in depth and wavenumber also affects the vegetation dissipation term (Equation 2.3) via the shallow-water dispersion relation.

A slight overestimate of wave setup remains near the landward end because the current solver does not generate set-down during shoaling (the radiation-stress gradient is not represented). This limitation was acknowledged, as some physical processes were simplified to achieve a more computationally efficient model for compound flooding. The quantitative comparison in Table 4.2 illustrates how the baseline model systematically overestimates the mean water level relative to Wu et al. (2011), while the improved formulation reduces these values by a factor of three to ten.

Scenario	Wu et al. (2011) [mm]	Baseline model [mm]	Improved model [mm]	Ratio
S2	0.27	1.13	0.32	3.59
S4	0.00	1.81	0.19	9.57
S6	0.47	1.81	0.61	2.96
S8	-0.25	2.31	0.25	9.31
S10	0.09	3.29	0.81	4.08
S12	-0.33	3.51	0.59	5.91
Average	–	–	–	**5.90**

Table 4.2: Comparison of mean water level at the landward end for Wu et al. experiments and `SFINCS-SnapWave` model variants. Values are in millimetres. The ratio indicates how many times larger the baseline model result is compared to the improved model.

Runtime tests confirm that the improvement does not introduce additional computational cost: the baseline model averaged 19.54 s (≈ 0.33 min), while the improved model averaged 19.55 s (≈ 0.33 min). These differences are negligible and within the variability expected from hardware conditions (e.g., charging state), indicating that the reconstruction of nonlinear orbital velocity using the empirical wave-shape model keeps computational demand low. Computational efficiency tests were performed on a laptop equipped with an Intel Core i7-13700H (13th Gen) processor and 16 GB of RAM, running Microsoft Windows 11 Home (Version 10.0.26100, Build 26100). All simulations were executed while the laptop was connected to power, as runtimes were found to vary slightly between charging and battery conditions.

Overall, including $F_{v,w}$ substantially reduces the overestimation of wave setup. On average across all scenarios, the setup at the landward end of the domain decreases by nearly a factor of six relative to the baseline, bringing the profile much closer to the measurements (Figure 4.5F). The resulting pattern—a small increase near the vegetation front followed by an almost constant level—is consistent with the `XBeach-SB` simulations that include the wave-shape model (van Rooijen et al. 2016) (Figure 4.3) and with the flume data of Wu et al. (2011). In short, the $F_{v,w}$ implementation improves the physical consistency of the setup response in vegetated conditions while preserving the computational efficiency of the coupled model.

4.3.3. Improved model statistical performance

Across all scenarios (evaluated along the flume), the improved model significantly reduces the scatter index (SI) and bias compared to the baseline. Figure 4.6 shows the comparison between measured mean water level and the improved `SFINCS-SnapWave` results, with associated SI and bias, for all scenarios. The improved model (blue dots) produces substantially lower SI and bias than the baseline, with SI decreasing from 3.52 to 1.50 and bias from 0.70 to 0.15. This indicates a more physically consistent behaviour, particularly the relatively constant water level within the vegetated region, which aligns more closely with the measurements. A more detailed discussion of these findings is presented in Chapter 5.

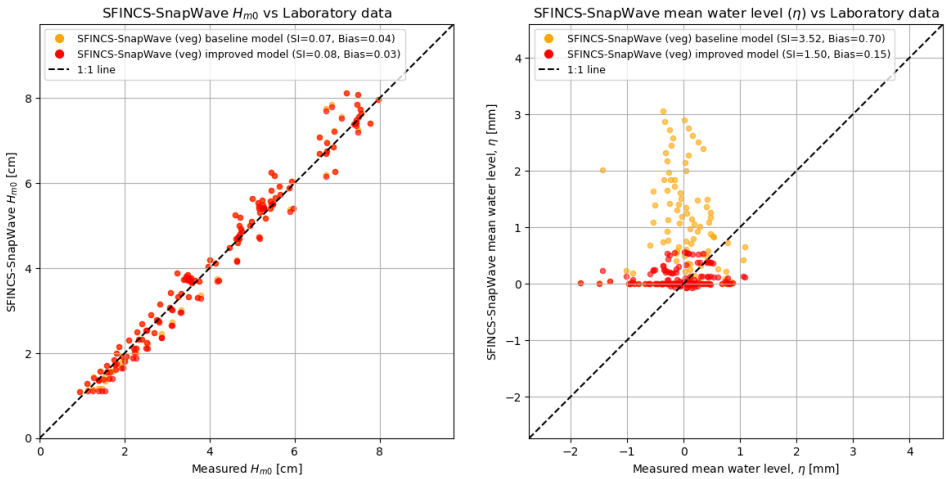

Figure 4.6: Model performance comparison against laboratory observations for all vegetated cases. The left panel shows significant wave height (H_{m0}), and the right panel shows mean water level (MWL). Orange markers represent the baseline `SFINCS-SnapWave` model (vegetation-induced wave dissipation only). Red markers indicate the improved model with nonlinear vegetation force ($F_{v,w}$). Dashed lines denote 1:1 reference. Scatter index (SI) and bias are shown in the legends.

5

Discussion

This study set out to evaluate and improve water-level predictions influenced by vegetation in SFINCS-SnapWave, using wave flume experiments and comparison with XBeach-SB as benchmarks. The inclusion of the nonlinear vegetation force ($F_{v,w}$) proved to be a good advancement: it substantially reduced the wave-setup bias in wave-dominated conditions, avoiding overestimation by a factor of six averaged across all scenarios measured in the landward end, while keeping runtime effectively unchanged. Building on these findings, this chapter reflects on the limitations of the improved model, its uncertainties, and the implications for broader application.

5.1. Model limitations and uncertainties

While the additional $F_{v,w}$ formulation improves vegetation–water level interaction in the model, several limitations remain. These are caused by both the underlying hydrodynamic formulations and the simplified representation of vegetation. The subsections below examine the most critical sources of uncertainty, their underlying causes, and their implications for predictive skill.

5.1.1. Inability to capture wave set-down during shoaling

The model fails to capture the set-down of the mean water level during wave shoaling. This is due to the SnapWave module calculating wave-induced forces solely from wave energy dissipation by bottom friction, wave breaking, and vegetation, which are then transferred to SFINCS to drive hydrodynamic responses. Unlike XBeach-SB, which computes wave forces from radiation stress gradients, SFINCS-SnapWave only generates forces where energy dissipation occurs—typically after wave breaking. As a result, it does not resolve the wave set-down that develops during shoaling, a process associated with energy redistribution rather than dissipation. While this limitation does not directly influence the vegetation processes, it affects the general output of the water level prediction. This limitation reflects the core formulation in the SnapWave source code, where the wave force is defined as:

```
F(k) = (Dw(k) + Dveg(k)) * kwav(k) / sig(k) / rho / depth(k)
```

5.1.2. Vegetation parameterisation and inputs

The selection of representative vegetation input and parameters is challenging. This becomes one of the sources of the model's uncertainties. For example, in reality, the vegetation parameters (b_v, h_v, and N_v) of one vegetation region compared to another might differ spatially, while taking one representative value for the whole region might lead to inaccurate results. In this model, vegetation is applied via an elevation-based mask, which restricts the choice of vegetation parameters. Additionally, vegetation-hydrodynamic interaction here is mainly accommodated by one bulk drag coefficient (C_D). For instance, a lower value might be applicable for more flexible vegetation and a higher value for the rigid one. Thus, the complex process of vegetation-hydrodynamic is highly simplified in this one parameter. Sensitivity analyses for these parameters are recommended for real-case applications. Lastly, indeed, in this model, we neglect entirely the dynamics of vegetation (breakage, uprooting, etc.) during flooding by

keeping the vegetation parameters constant over time. This introduces another uncertainty for real-world applications.

5.1.3. Vegetation force due to wave nonlinearity ($F_{v,w}$)

A central advancement of this study was the inclusion of the nonlinear vegetation force $F_{v,w}$. While this addition clearly reduced wave-setup bias, its present formulation also carries assumptions that introduce uncertainties. These concern how vegetation is represented vertically, how emergence effects are treated, and the applicability of the wave-shape model used to reconstruct nonlinear orbital velocities.

Vertical representation. Vegetation force due to wave nonlinearity ($F_{v,w}$) is currently computed with a single vegetation layer in the improved model. A multi-layer approach (varying b_v, N_v, and C_D vertically) would better represent vertical heterogeneity and could change the partitioning between set-down and set-up. This is indeed an important component, especially for simulating vegetation that has high variability in vertical structures, such as mangroves. Thus, Appendix C.3 provides the adapted code that can be applied to take into account the layering computation approach in $F_{v,w}$.

Emergence effect. In the improved model, the effective submerged vegetation height (h'_v) is taken conservatively as the minimum value of vegetation height (h_v) and still water depth (h) (see equation 4.2), which means not considering free-surface oscillation (emergence) effects, as explained in Chapter 4. In contrast, `XBeach-SB` provide a more detailed approach, by taking into account the free-surface oscillation (emergence) effects (see equation 4.3).

However, when we enable the emergence variant in `SFINCS-SnapWave`, the model tends to *overestimate* the reduction of mean water level by vegetation across scenarios (Figure D.1). A plausible explanation is that the vegetation force due to the mean flow ($F_{v,m}$) is still absent in our current implementation— it is expected to increase the water level slightly. Under breaking waves, an offshore-directed undertow develops, and the associated vegetation drag acts in the opposite (onshore) direction, partly offsetting the offshore-directed contribution from $F_{v,w}$. A simple post-processed estimate of $F_{v,m}$ is presented in Appendix B, and the results are consistent with this reasoning, showing that $F_{v,m}$ contributes an onshore-directed force that partly counteracts the offshore effect of $F_{v,w}$. Moreover, discrepancies may also stem from differing assumptions between `XBeach-SB` and `SFINCS-SnapWave`. A deeper inter-comparison is therefore needed to understand how the emergence effect is applied in both models. For future work, Appendix C.3 provides the code that enables emergence in the $F_{v,w}$ computation and can be used to advance the model.

Consequently, in the main results we do not represent the emergent effect, i.e. the temporal variation in water level due to wave action that periodically exposes or submerges vegetation. In reality—especially during compound flooding—the water level can vary due to storm surge or the interaction of river discharge and waves, producing a time-varying submerged vegetation height. This variability affects the vegetation drag force $F_{v,w}$, including intra-wave variations within each cycle. This limitation should therefore be considered a priority for future model development.

Wave-shape model applicability. The wave-shape reconstruction to compute the nonlinear waves' orbital velocity (u_w) and free-surface oscillation (η_w) was derived from a dataset of field observations of wave skewness and asymmetry from the coast without vegetation (Vries 2009). Thus, this might lead to an additional source of uncertainty, as to whether the reconstructed orbital velocity is completely applicable for vegetated regions. Therefore, in the future, if any other new empirical relation is available for a vegetated region, this may serve as a basis for further advancing the model.

5.1.4. Vegetation force due to mean flow ($F_{v,m}$)

The vegetation force due to mean flow drag ($F_{v,m}$) is still unavailable in the improved model. Even though the ($F_{v,m}$) does not give a substantial effect in this particular simulation setting (see Appendix B), these results should not be generalised to all scenarios. For example, in surge- or tide-dominated events, the mean flow can exceed the wave influence, and the vegetation drag may act in different directions depending on the flow. Such long-wave propagation towards vegetation induces a more

significant drag force. Thus, the incorporation of $F_{v,m}$ into the model is considered important to be able to capture the whole vegetation effects.

While the $F_{v,m}$ component is still missing, there is another way to incorporate a similar effect into the model. In practice, users sometimes emulate mean-flow drag via increased Manning's n within vegetated areas, especially for large-scale simulation to maintain low computational demand (Radfar et al. 2024). Some studies show a range of values of Manning's n to be applied as a vegetation representative, such as Noarayanan et al. (2012). However, this bulk roughness might not represent vegetation parameters explicitly, and its equivalence to $F_{v,m}$ is unverified. Bed roughness influences only bottom drag and does not account for vertical vegetation structure or dynamic responses to changing wave conditions. Moreover, a single roughness parameter is insufficient to capture vegetation properties such as height, density, and stem diameter. Since $F_{v,m}$ directly depends on flow velocity and vegetation properties, adding it is expected to improve accuracy—especially for current-related cases.

Lastly, the $F_{v,m}$ is indeed related to IG waves as the long waves tend to generate more currents. In the improved model, IG-band wave heights are not yet influenced by vegetation. Currently, the model overestimates IG wave energy in vegetated cases, failing to capture the observed 50% reduction reported by `XBeach-SB`. This discrepancy underscores the inability of `SFINCS-SnapWave` to represent IG wave–vegetation interactions due to its simplified, boundary-driven IG formulation. Moreover, the understanding of vegetation-IG interaction remains limited as well. Dedicated validation with data that resolves IG attenuation in vegetation is needed and further used as the basis to improve the model.

5.2. Real-world applicability

Beyond the technical model formulations, it is equally important to reflect on how the results transfer to real-world conditions. Laboratory flume experiments and one-dimensional simulations provide valuable insights, but they do not fully capture the complexity of natural coastal environments. The following section discusses the limitations of the present validation framework and outlines the steps needed for broader applicability.

Validation data and test scale. While this study validates the improved `SFINCS-SnapWave` model using small-scale wave flume laboratory data from Wu et al. (2011), some uncertainties arise when applying these results to real-scale coastal environments. It is known that scaled tests might introduce different results from real-scale tests. For example, laboratory flume studies often represent vegetation as rigid cylinders and produce bulk drag coefficients that have not yet been validated under extreme, field-scale conditions. Scale effects arise because vegetation flexibility, surface complexity, and viscous stresses are not reproduced accurately at small scales, which can lead to overestimated drag values compared to large-scale or field observations (van Wesenbeeck, Wolters, et al. 2022). Thus, it is important to validate this improved model using available data from real-scale experiments.

Additionally, Wu et al. (2011) laboratory experiments use uniform and rigid vegetation without any vertical layering, which does not represent the structural variation and flexibility of natural vegetation. In reality, mangroves, for example, are relatively rigid but have clear vertical layering, with varying stem density and diameter from bottom to top. In contrast, salt marshes are more uniform but highly flexible. Thus, while the improved model seems valid for this particular experiment data, it is better to be validated against a wide range of different vegetation characteristics.

Forcing configuration. The Wu et al. (2011) experiment, which served as the basis for this model validation, was limited to scenarios involving wave-driven cases. Although it may produce a wave-induced current, it is expected to make a small contribution. Thus, this particular experiment's data might not be suitable for testing the future inclusion of the vegetation force due to the mean flow $F_{v,m}$ in the model or for studying the effect of different bed roughness on the vegetation drag. Thus, for broader application, current-only or even wave-current experiment data, such as done by Yin et al. (2020), can be used to further validate the model while exploring the contribution of vegetation force due to the mean flow $F_{v,m}$. Additionally, to validate the influence of IG wave attenuation, experimental data by S. M. Løvås (2000) might be useful.

The use of global data. One approach to further explore the sensitivity of this model based on realistic input is by using global data. Appendix E presents the simulation configuration and scenarios that can be performed to explore mangroves' influence on the wave-surge driven flooding, building upon global data. The proposed 1D simulation framework is appropriate for idealised open coast settings, while filtering location with high dependency on wave-surge extreme events. This exploration might give additional insight into the contribution of wave-only, current-only, and wave-current interactions in mangrove areas.

2D real-case applications. The controlled nature of laboratory and one-dimensional (1D) model setups is useful for isolating key hydrodynamic processes and understanding vegetation–flow dynamics in simplified conditions. However, such configurations cannot fully capture the complexity of real-world multi-driven coastal flooding, where interactions between waves, storm surge, and river discharge—as well as lateral processes in estuaries, deltas, and lagoons—play a significant role. To enhance the reliability of the model for large-scale and realistic coastal applications, future validation and exploration should therefore be extended to two-dimensional (2D) field-based settings.

6

Conclusion and recommendation

6.1. Conclusion

This study set out to enhance the physical representation of vegetation processes in a computationally efficient flood model, with the aim of improving water-level predictions under coastal forcing. The baseline `SFINCS-SnapWave` model was evaluated against laboratory flume data and a benchmark process-based model `XBeach-SB`, its key limitations were identified, and a targeted improvement was implemented and tested. The conclusions to the five guiding sub-research questions are as follows:

1. **What are the essential physical processes in vegetation–hydrodynamic interactions that influence water-level predictions?**

   Three force contributions are most relevant for coastal-driven water levels over vegetated regions: (i) the wave-induced force F_w (linked to short-wave energy dissipation and radiation-stress effects), (ii) the vegetation force associated with nonlinearity of the waves $F_{v,w}$, and (iii) the vegetation force associated with mean flow $F_{v,m}$. Together, these terms set the sign and magnitude of the net external forcing and thus determine the setup/set-down through the momentum equation.

2. **How well does the initial model reproduce wave transformation and water levels in vegetated conditions?**

   The baseline `SFINCS-SnapWave` reproduced significant wave heights well in both vegetated and non-vegetated cases, showing low SI and small bias. However, it substantially overestimated nearshore mean water levels in the vegetated scenarios, with an overall bias of 0.70 across all scenarios and up to nearly four times higher in S12 when validated against Wu et al. (2011) and compared with `XBeach-SB` (van Rooijen et al. 2016). In particular, the model failed to reproduce the wave-induced set-down that normally occurs during shoaling, because water level variations in the baseline formulation arise solely from local wave energy dissipation (by breaking or vegetation) and not from cross-shore gradients in radiation stress that drive set-down.

3. **Which limitations in vegetation representation affect the accuracy of the initial model prediction on water levels?**

   Four limitations were identified: (i) the absence of $F_{v,w}$ (vegetation drag due to nonlinear wave shape), (ii) the absence of $F_{v,m}$ (vegetation drag due to mean flow), (iii) a dissipation-only wave–force formulation that cannot generate offshore-directed forcing during shoaling (hence no set-down), and (iv) the lack of vegetation effects on IG-wave heights. These omissions collectively bias water-level predictions in the vegetated runs. For the present wave-dominated flume conditions, $F_{v,w}$ can be identified as the dominant missing process: the baseline `SFINCS-SnapWave` and `XBeach-SB` without the wave-shape option produced comparable overestimates, while the inclusion of the wave-shape formulation in `XBeach-SB` (representing $F_{v,w}$) yielded markedly improved agreement with the measurements.

4. **To what extent does the improved model enhance the accuracy of water level and wave-transformation predictions?**

   Implementing $F_{v,w}$ via a wave-shape reconstruction reduced the net external force within the vegetation field and produced a near-constant mean water level across the regions, in line with measurements and `XBeach-SB` (with wave-shape). On average across all scenarios, the modelled wave setup at the landward end decreased by roughly a factor of six relative to the baseline. Aggregated statistics over all vegetated scenarios showed improvement in mean water level: SI decreased from 3.52 to 1.50 and bias from 0.70 to 0.15. Significant wave heights remained in good agreement throughout the scenarios.

   This improvement is explained by the role of $F_{v,w}$: it captures the net vegetation force due to skewed waves, which opposes the wave-breaking forcing. In the baseline model, this force component is still absent. Adding $F_{v,w}$ therefore corrects the excessive setup and brings predictions in line with data.

5. **What is the impact of the model improvements on computation time?**

   The improvement had almost no impact on runtime. The baseline and improved models completed in 19.54 s and 19.55 s, respectively, corresponding to a difference of only 0.07%. This confirms that the computational efficiency of the model is preserved.

6.2. Recommendation

The following recommendations are proposed for future research and for enhancing vegetation representation in `SFINCS-SnapWave`:

1. **Add vegetation force due to mean flow ($F_{v,m}$) components.** The current implementation focuses on the wave-induced vegetation force ($F_{v,w}$). Incorporating the mean flow drag force ($F_{v,m}$) is recommended, especially for models applicable to surge- or tide-dominated events where long-wave flow contributes significantly to vegetation resistance.
2. **Validate the model against wave-current driver.** Once $F_{v,m}$ components are incorporated into the model, it is recommended to validate it against current-related experiment data. Isolating the wave and current effects is recommended to identify the contribution of each driver. Furthermore, this approach may help to better understand the representation of vegetation by comparing it with bed roughness ($F_{v,m}$ vs. bed roughness).
3. **Validate and improve vegetation effects on IG waves.** The present validation Wu et al. (2011) does not include IG wave measurements, so IG attenuation could not be assessed. As a next step, the model could be tested against experiments that report IG wave energy in vegetated settings—e.g., S. M. Løvås (2000), as referenced by van Rooijen et al. (2016)—to quantify attenuation and calibrate relevant parameters. This would provide a first targeted evaluation of the model's IG–wave performance in vegetated regions.
4. **Validate against field-scale measurements.** While small-scale laboratory data were useful for controlled validation, their simplification introduces uncertainty when applied to real-world cases. Field-scale measurements that capture real vegetation structures, layering, and flow complexity are needed for more robust model validation.
5. **Extend the model to 2D applications.** The 1D simulation performed in this study is useful for idealised scenarios, but cannot capture lateral hydrodynamic interactions. For applications in estuaries, deltas, or lagoons, real case 2D model configurations are recommended to simulate more complex interactions of multi-driver coastal flooding, validated against field validation data.
6. **Explore vegetation-specific wave shape models.** The current wave shape model relies on empirical relations derived from non-vegetated coasts. Developing or adopting empirical relations that account for vegetation effects on wave skewness and asymmetry would improve the accuracy of intrawave velocity reconstruction.

References

Anderson, M. E. and J. M. Smith (2014). “Wave attenuation by flexible, idealized salt marsh vegetation”. In: *Coastal Engineering* 83, pp. 82–92. DOI: 10.1016/j.coastaleng.2013.10.004.

Austin, James Edward (2021). “The Effect of Simulated Mangrove Forest Width on Shoreline Stabilization at Multiple Tidal Water Levels”. Theses and Dissertations. 1128. Master’s thesis. Melbourne, Florida, USA: Florida Institute of Technology. URL: https://repository.fit.edu/etd/1128.

Baldock, T. E. et al. (1998). “Cross-shore hydrodynamics within an unsaturated surf zone”. In: *Coastal Engineering* 34.3, pp. 173–196. ISSN: 0378-3839. DOI: 10.1016/S0378-3839(98)00017-9. URL: https://www.sciencedirect.com/science/article/pii/S0378383998000179.

Bevacqua, E. et al. (2019). “Higher probability of compound flooding from precipitation and storm surge in Europe under anthropogenic climate change”. In: *Science Advances* 5.9, eaaw5531. DOI: 10.1126/sciadv.aaw5531. eprint: https://www.science.org/doi/pdf/10.1126/sciadv.aaw5531. URL: https://www.science.org/doi/abs/10.1126/sciadv.aaw5531.

Bosboom, J. and M. J. F. Stive (2023). *Coastal Dynamics*. Version 1.2. Subversion (SVN) revision 1489 logged at 2023-01-11 14:53. Cover image: Atlantic coast, Angola (courtesy Stefanie Ross). Corresponding author: j.bosboom@tudelft.nl. Delft, The Netherlands: TU Delft Open. ISBN: 978-94-6366-370-0. DOI: 10.5074/T.2021.001.

Buckley, Mark L. et al. (2016). “Wave Setup over a Fringing Reef with Large Bottom Roughness”. In: *Journal of Physical Oceanography* 46.8, pp. 2317–2333. DOI: 10.1175/JPO-D-15-0148.1.

Burger, B. (2005). “Wave Attenuation in Mangrove Forests”. Supervisors: M.J.F. Stive, H.J. Verhagen, M. de Vries, M. Zijlema, H.J. Opdam. Master’s thesis. Delft University of Technology. URL: http://resolver.tudelft.nl/uuid:0e4c6450-fe5d-4693-9ca9-58da343448b7.

Cascadia CoPes Hub (2025). *Team 2 – Compound Flooding*. Accessed: 2025-05-16. URL: https://cascadiacopeshub.org/team-2-compound-flooding/.

Couasnon, Anaïs et al. (2020). “Measuring compound flood potential from river discharge and storm surge extremes at the global scale”. In: *Natural Hazards and Earth System Sciences* 20, pp. 489–504. DOI: 10.5194/nhess-20-489-2020. URL: https://doi.org/10.5194/nhess-20-489-2020.

Dalrymple, R. A., J. T. Kirby, and P. A. Hwang (1984). “Wave diffraction due to areas of energy dissipation”. In: *Journal of Waterway, Port, Coastal, and Ocean Engineering* 110, pp. 67–79.

Das, S. C., K. Iimura, and N. Tanaka (2011). “Effects of Coastal Vegetation Species and Ground Slope on Storm Surge Disaster Mitigation”. In: *Coastal Engineering Proceedings*. Vol. 1. 32, p. 24.

De Dominicis, Michela et al. (2023). “Mangrove forests can be an effective coastal defence in the Pearl River Delta, China”. In: *Communications Earth Environment* 4, p. 13. DOI: 10.1038/s43247-022-00672-7. URL: https://doi.org/10.1038/s43247-022-00672-7.

Dean, R. G. and C. J. Bender (2006). “Static wave setup with emphasis on damping effects by vegetation and bottom friction”. In: *Coastal Engineering* 53.2, pp. 149–156. DOI: 10.1016/j.coastaleng.2005.10.005.

Dullaart, J. C. M., S. Muis, N. Bloemendaal, et al. (2021). “Accounting for tropical cyclones more than doubles the global population exposed to low-probability coastal flooding”. In: *Communications Earth & Environment* 2. Published: 29 June 2021, p. 135. DOI: 10.1038/s43247-021-00204-9. URL: https://doi.org/10.1038/s43247-021-00204-9.

Dullaart, J. C. M., S. Muis, H. de Moel, et al. (2023). “Enabling dynamic modelling of coastal flooding by defining storm tide hydrographs”. In: *Natural Hazards and Earth System Sciences* 23.5, pp. 1847–1862. DOI: 10.5194/nhess-23-1847-2023. URL: https://nhess.copernicus.org/articles/23/1847/2023/.

Ellison, Joanna C. (2000). “Mangrove community zonation in Belize: a test of the null hypothesis”. In: *Journal of Ecology* 88.4, pp. 817–828. DOI: 10.1046/j.1365-2745.2000.00500.x. URL: https://doi.org/10.1046/j.1365-2745.2000.00500.x.

Etminan, Vahid, Ryan J. Lowe, and Marco Ghisalberti (2019). “Canopy resistance on oscillatory flows”. In: *Coastal Engineering* 152, p. 103502. DOI: 10.1016/j.coastaleng.2019.04.014.

Fairchild, T. P. et al. (2021). “Coastal wetlands mitigate storm flooding and associated costs in estuaries”. In: *Environmental Research Letters* 16.7, p. 074034. DOI: 10.1088/1748-9326/ac0f64.

Friess, Daniel A. et al. (2019). “The State of the World’s Mangrove Forests: Past, Present, and Future”. In: *Annual Review of Environment and Resources* 44, pp. 89–115. DOI: 10.1146/annurev-environ-101718-033302. URL: https://doi.org/10.1146/annurev-environ-101718-033302.

Garzon, J. L. et al. (2019). “Wave attenuation by Spartina saltmarshes in the Chesapeake Bay under storm surge conditions”. In: *Journal of Geophysical Research: Oceans* 124.8, pp. 5220–5243. DOI: 10.1029/2018JC014865.

Gedan, K. B. et al. (2011). “The present and future role of coastal wetland vegetation in protecting shorelines: answering recent challenges to the paradigm”. In: *Climatic Change* 106, pp. 7–29. DOI: 10.1007/s10584-010-0003-7.

Gijón Mancheño, Alejandra (2022). “Restoring mangroves with structures: Improving the mangrove habitat using local materials”. Dissertation. Delft University of Technology. DOI: 10.4233/uuid:ed292367-ed2b-4bd3-a236-9f10d9c01da8. URL: https://doi.org/10.4233/uuid:ed292367-ed2b-4bd3-a236-9f10d9c01da8.

Giri, C. et al. (2010). “Status and distribution of mangrove forests of the world using earth observation satellite data”. In: *Aquatic Conservation: Marine and Freshwater Ecosystems* 20.3. First published: 17 August 2010, pp. 154–159. DOI: 10.1111/j.1466-8238.2010.00584.x.

— (2011). “Status and distribution of mangrove forests of the world using Earth observation satellite data”. In: *Global Ecology and Biogeography* 20.1, pp. 154–159. DOI: 10.1111/j.1466-8238.2010.00584.x.

Goldberg, Liza et al. (2020). “Global declines in human-driven mangrove loss”. In: *Global Change Biology*. This is an open access article under the terms of the Creative Commons Attribution License. Correspondence: liza.a.goldberg@nasa.gov. DOI: 10.1111/gcb.15275. URL: https://doi.org/10.1111/gcb.15275.

Gori, Avantika, Ning Lin, and Dazhi Xi (2020). “Tropical Cyclone Compound Flood Hazard Assessment: From Investigating Drivers to Quantifying Extreme Water Levels”. In: *Earth’s Future* 8.12. e2020EF001660 2020EF001660, e2020EF001660. DOI: https://doi.org/10.1029/2020EF001660. eprint: https://agupubs.onlinelibrary.wiley.com/doi/pdf/10.1029/2020EF001660. URL: https://agupubs.onlinelibrary.wiley.com/doi/abs/10.1029/2020EF001660.

Green, Joshua et al. (2025). “Review article: A comprehensive review of compound flooding literature with a focus on coastal and estuarine regions”. In: *Natural Hazards and Earth System Sciences* 25, pp. 747–816. DOI: 10.5194/nhess-25-747-2025. URL: https://doi.org/10.5194/nhess-25-747-2025.

Hallegatte, Stéphane et al. (2013). “Future flood losses in major coastal cities”. In: *Nature Climate Change* 3, pp. 802–806. DOI: 10.1038/nclimate1979. URL: https://doi.org/10.1038/nclimate1979.

Hasselmann, Klaus and J. Collins (1968). “Spectral dissipation of finite-depth gravity waves due to turbulent bottom friction”. In: *Journal of Marine Research* 26, pp. 77–85.

Henderson, S. M., R. T. Guza, et al. (2006). “Nonlinear generation and loss of infragravity wave energy”. In: *Journal of Geophysical Research* 111.C12, p. C12007. DOI: 10.1029/2006JC003539.

Henderson, S. M., B. K. Norris, et al. (2017). “Wave-frequency flows within a near-bed vegetation canopy”. In: *Continental Shelf Research* 147, pp. 91–101. DOI: 10.1016/j.csr.2017.06.010.

Hendriks, I. (2014). “Wave Attenuation by Mangrove Forests: Field Data and Numerical Modelling”. MA thesis. University of Twente. URL: https://www.utwente.nl/en/et/cem/education/assignments/finished-msc-assignments/finished_graduation_projects/wem-msc-thesis/2014/hendriks.pdf.

Herrera-Silveira, J. A. et al. (2022). “Hurricane Damages to Mangrove Forests and Post-Storm Restoration Techniques and Costs”. In: *The Nature Conservancy*.

Hochard, J. P., S. Hamilton, and E. B. Barbier (2019). “Mangroves shelter coastal economic activity from cyclones”. In: *Proceedings of the National Academy of Sciences* 116.25, pp. 12232–12237. DOI: 10.1073/pnas.1820067116.

Horstman, E. et al. (2012). “Wave Attenuation in Mangrove Forests: Field Data Obtained in Trang, Thailand”. In: *Coastal Engineering Proceedings*. Vol. 1. 33, waves.40. DOI: 10.9753/icce.v33.waves.40.

Horstman, E. M. (2014). *Data Report: Field Campaign Trang, Thailand; November 2010 – May 2011*. Tech. rep. Enschede, The Netherlands: University of Twente.

Horstman, E.M. et al. (2014). "Wave attenuation in mangroves: A quantitative approach to field observations". In: *Coastal Engineering* 94, pp. 47–62. ISSN: 0378-3839. DOI: https://doi.org/10.1016/j.coastaleng.2014.08.005. URL: https://www.sciencedirect.com/science/article/pii/S0378383914001574.

Jadhav, R. S., Q. Chen, and J. M. Smith (2013). "Spectral distribution of wave energy dissipation by salt marsh vegetation". In: *Coastal Engineering* 77, pp. 99–107. DOI: 10.1016/j.coastaleng.2013.02.013.

Janssen, M.P.J. (2016). "Flood Hazard Reduction by Mangroves". Hydraulic Engineering Department. Supervisors: M.J.F. Stive, B.K. van Wesenbeeck, J.T. Dijkstra, B. Hofland, V. Vuik. Master's thesis. Delft, The Netherlands: Delft University of Technology. URL: http://resolver.tudelft.nl/uuid:b3cfe9b0-c8d3-4eb6-aad2-977d879430b5.

Kalloe, Su A. et al. (2022). "Quantifying Frontal-Surface Area of Woody Vegetation: A Crucial Parameter for Wave Attenuation". In: *Frontiers in Marine Science* 9. DOI: 10.3389/fmars.2022.820846.

Kathiresan, K. (2021). "Mangroves: Ecology, Biodiversity and Management". In: *Mangroves: Ecology, Biodiversity and Management*. Ed. by R. P. Rastogi et al. Springer Nature Singapore.

Knapp, K. R. et al. (2010). "The International Best Track Archive for Climate Stewardship (IBTrACS): Unifying tropical cyclone best track data". In: *Bulletin of the American Meteorological Society* 91, pp. 363–376. DOI: 10.1175/2009BAMS2755.1.

Krauss, Ken W. and Michael J. Osland (2020). "Tropical cyclones and the organization of mangrove forests: a review". In: *Annals of Botany* 125.2, pp. 213–234. DOI: 10.1093/aob/mcz161.

Leijnse, Tim et al. (2021). "Modeling compound flooding in coastal systems using a computationally efficient reduced-physics solver: Including fluvial, pluvial, tidal, wind- and wave-driven processes". In: *Coastal Engineering* 163, p. 103796. DOI: 10.1016/j.coastaleng.2020.103796. URL: https://doi.org/10.1016/j.coastaleng.2020.103796.

Leijnse, Tim W. B. et al. (2024). "Estimating nearshore infragravity wave conditions at large spatial scales". In: *Frontiers in Marine Science* 11, p. 1355095. DOI: 10.3389/fmars.2024.1355095. URL: https://doi.org/10.3389/fmars.2024.1355095.

Løvås, S. M. (2000). "Hydro-physical conditions in kelp forests and the effect on wave damping and dune erosion: A case study on *Laminaria hyperborea*". PhD thesis. Trondheim, Norway: Faculty of Civil, Environmental Engineering, Norwegian University of Science, and Technology.

Løvås, Sigrid M. and Alfred Tørum (2001). "Effect of the kelp *Laminaria hyperborea* upon sand dune erosion and water particle velocities". In: *Coastal Engineering* 44.1, pp. 37–63. DOI: 10.1016/S0378-3839(01)00021-7.

Luhar, Mitul et al. (2010). "Wave-induced velocities inside a model seagrass bed". In: *Journal of Geophysical Research: Oceans* 115, p. C12005. DOI: 10.1029/2010JC006345.

Marcos, Marta et al. (2019). "Increased extreme coastal water levels due to the combined action of storm surges and wind waves". In: *Geophysical Research Letters* 46.7, pp. 4356–4364. DOI: 10.1029/2019GL082599.

Marsooli, R., P. M. Orton, and G. Mellor (2017). "Modeling wave attenuation by salt marshes in Jamaica Bay, New York, using a new rapid wave model". In: *Journal of Geophysical Research: Oceans* 122.7, pp. 5689–5707. DOI: 10.1002/2017JC012772.

Maza, María, Javier L. Lara, and Iñigo J. Losada (2019). "Experimental analysis of wave attenuation and drag forces in a realistic fringe Rhizophora mangrove forest". In: *Advances in Water Resources* 131, p. 103376. DOI: 10.1016/j.advwatres.2019.07.006.

Mazda, Y. et al. (2006). "Wave reduction in a mangrove forest dominated by Sonneratia sp." In: *Wetlands Ecology and Management* 14, pp. 365–378.

McIvor, Anna et al. (2012). *Reduction of Wind and Swell Waves by Mangroves*. Natural Coastal Protection Series: Report 1, Working Paper 40 ISSN 2050-7941. Cambridge Coastal Research Unit. URL: https://www.nature.org/media/oceansandcoasts/natural-coastal-protection.pdf.

Mendez, F. J. and I. J. Losada (2004). "An empirical model to estimate the propagation of random breaking and nonbreaking waves over vegetation fields". In: *Coastal Engineering* 51, pp. 103–118.

Mo, Yu, Marc Simard, and Jim W. Hall (2023). "Tropical cyclone risk to global mangrove ecosystems: potential future regional shifts". In: *Frontiers in Ecology and the Environment*. First published: 06 June 2023. DOI: 10.1002/fee.2650. URL: https://doi.org/10.1002/fee.2650.

Möller, I. et al. (2014). “Wave attenuation over coastal salt marshes under storm surge conditions”. In: *Nature Geoscience* 7, pp. 727–731. DOI: 10.1038/ngeo2251.

Montgomery, J. M. et al. (2019). “Attenuation of storm surges by coastal mangroves”. In: *Geophysical Research Letters* 46.5, pp. 2680–2689. DOI: 10.1029/2018GL081636.

Morison, J. R. et al. (1950). *The Force Exerted by Surface Waves on Piles*. Tech. rep. TR-3. Berkeley, California: University of California, Institute of Engineering Research.

Muis, Sanne et al. (2016). “A global reanalysis of storm surges and extreme sea levels”. In: *Nature Communications* 7, p. 11969. DOI: 10.1038/ncomms11969. URL: https://doi.org/10.1038/ncomms11969.

Narayan, S. et al. (2016). “The effectiveness, costs and coastal protection benefits of natural and nature-based defences”. In: *PLOS ONE* 11.5, e0154735. DOI: 10.1371/journal.pone.0154735.

Noarayanan, L., K. Murali, and V. Sundar (Mar. 2012). “Manning’s ‘n’ co-efficient for flexible emergent vegetation in tandem configuration”. In: *Journal of Hydro-environment Research* 6.1, pp. 51–62. ISSN: 1570-6443. DOI: 10.1016/j.jher.2011.05.002. URL: https://doi.org/10.1016/j.jher.2011.05.002.

Norris, B. K. et al. (2021). “Relating millimeter-scale turbulence to meter-scale subtidal erosion and accretion across the fringe of a coastal mangrove forest”. In: *Earth Surface Processes and Landforms* 46.3, pp. 573–592.

Pelckmans, Ignace et al. (2024). “Mangroves as nature-based mitigation for ENSO-driven compound flood risks in a large river delta”. In: *Hydrology and Earth System Sciences* 28. Accessed: 2024-12-05, pp. 1463–1476. DOI: 10.5194/hess-28-1463-2024. URL: https://doi.org/10.5194/hess-28-1463-2024.

Phan, Linh K., Jaap S. M. van Thiel de Vries, and Marcel J. F. Stive (2015). “Coastal Mangrove Squeeze in the Mekong Delta”. In: *Journal of Coastal Research* 31.2, pp. 233–243. DOI: 10.2112/JCOASTRES-D-14-00049.1.

Phillips, O. M. (1977). *The Dynamics of the Upper Ocean*. 2nd. Cambridge, U. K.: Cambridge University Press, p. 336.

Pinsky, M. L., G. Guannel, and K. K. Arkema (2013). “Quantifying wave attenuation to inform coastal habitat conservation”. In: *Ecosphere* 4.8, pp. 1–16. DOI: 10.1890/ES13-00080.1.

Polidoro, Beth A. et al. (2010). “The loss of species: Mangrove extinction risk and geographic areas of global concern”. In: *PLoS ONE* 5.4, e10095. DOI: 10.1371/journal.pone.0010095. URL: https://doi.org/10.1371/journal.pone.0010095.

Quartel, S. et al. (2007). “Wave attenuation in coastal mangroves in the Red River Delta, Vietnam”. In: *Journal of Asian Earth Sciences* 29, pp. 576–584.

Radfar, Soheil et al. (2024). “Nature-based solutions as buffers against coastal compound flooding: Exploring potential framework for process-based modeling of hazard mitigation”. In: *Science of the Total Environment* 938. Available online 29 May 2024, p. 173529. DOI: 10.1016/j.scitotenv.2024.173529. URL: https://doi.org/10.1016/j.scitotenv.2024.173529.

Resio, D. T. and J. J. Westerink (2008). “Modelling the physics of storm surges”. In: *Physics Today* 61.9, pp. 33–38. DOI: 10.1063/1.2982120.

Rienecker, M. M. and J. D. Fenton (1981). “A Fourier approximation method for steady water waves”. In: *Journal of Fluid Mechanics* 104, pp. 119–137. DOI: 10.1017/S0022112081002851.

Riffe, K. C., S. M. Henderson, and J. C. Mullarney (2011). “Wave dissipation by flexible vegetation”. In: *Geophysical Research Letters* 38.18, p. L18607. DOI: 10.1029/2011GL048773.

Roelvink, Dano et al. (2025). “SnapWave: fast, implicit wave transformation from offshore to nearshore”. In: *EGUsphere*. Preprint. Discussion started: 24 March 2025. DOI: 10.5194/egusphere-2025-492. URL: https://doi.org/10.5194/egusphere-2025-492.

Roelvink, J. A. (1993). “Dissipation in random wave groups incident on a beach”. In: *Coastal Engineering* 19.1, pp. 127–150. DOI: 10.1016/0378-3839(93)90021-Y.

Roelvink, J. A. et al. (Nov. 2009). “Modelling storm impacts on beaches, dunes and barrier islands”. In: *Coastal Engineering* 56.11-12, pp. 1133–1152. DOI: 10.1016/j.coastaleng.2009.08.006. URL: http://linkinghub.elsevier.com/retrieve/pii/S0378383909001252.

Romañach, Stephanie S. et al. (2018). “Conservation and restoration of mangroves: Global status, perspectives, and prognosis”. In: *Ocean & Coastal Management* 154, pp. 72–82. ISSN: 0964-5691. DOI: 10.1016/j.ocecoaman.2018.01.009. URL: https://www.sciencedirect.com/science/article/pii/S0964569117301710.

Ruessink, B. G., G. Ramaekers, and L. C. van Rijn (2012). “On the parameterization of the free-stream non-linear wave orbital motion in nearshore morphodynamic models”. In: *Coastal Engineering* 65, pp. 56–63. DOI: 10.1016/j.coastaleng.2012.03.006.

Sanders, B. F., O. E. J. Wing, and P. D. Bates (2024). “Flooding is not like filling a bath”. In: *Earth’s Future* 12, e2024EF005164. DOI: 10.1029/2024EF005164.

Schipper, Matthieu de (2024). *Lecture 4.1 Nearshore Hydrodynamics*. Slides from course Advanced Coastal System Q4 2023-2024, TU Delft.

Schoutens, K. et al. (2019). “How effective are tidal marshes as nature-based shoreline protection throughout seasons?” In: *Limnology and Oceanography* 64.4, pp. 1750–1762.

Sebastian, Antonia (2022). “Chapter 7 - Compound flooding”. In: *Coastal Flood Risk Reduction*. Ed. by Samuel Brody, Yoonjeong Lee, and Baukje Bee Kothuis. Elsevier, pp. 77–88. ISBN: 978-0-323-85251-7. DOI: https://doi.org/10.1016/B978-0-323-85251-7.00007-X. URL: https://www.sciencedirect.com/science/article/pii/B978032385251700007X.

Smolders, S. et al. (2015). “Role of intertidal wetlands for tidal and storm tide attenuation along a confined estuary: a model study”. In: *Natural Hazards and Earth System Sciences* 15.7, pp. 1659–1675. DOI: 10.5194/nhess-15-1659-2015.

Spier, Daphne et al. (2016). “Flood regime as a driver of the distribution of mangrove and salt marsh species in a subtropical estuary”. In: *Journal of Experimental Marine Biology and Ecology* 483, pp. 120–129.

Sumer, B. Mutlu and Jørgen Fredsøe (1998). “Book review: Hydrodynamics around cylindrical structures, B. M. Sumer and J. Fredsøe, World Scientific, Singapore”. In: *Journal of Fluids and Structures* 12, pp. 221–222.

Suzuki, Tomohiro et al. (2012). “Wave dissipation by vegetation with layer schematization in SWAN”. In: *Coastal Engineering* 59, pp. 64–71. DOI: 10.1016/j.coastaleng.2011.07.006. URL: https://doi.org/10.1016/j.coastaleng.2011.07.006.

Tanino, Y. and H. M. Nepf (2008). “Laboratory investigation of mean drag in a random array of rigid, emergent cylinders”. In: *Journal of Hydraulic Engineering* 134.1, pp. 34–41. DOI: 10.1061/(ASCE)0733-9429(2008)134:1(34).

Temmerman, Stijn et al. (2023). “Marshes and Mangroves as Nature-Based Coastal Storm Buffers”. In: *Annual Review of Marine Science* 15. First published as a Review in Advance on July 18, 2022. Licensed under a Creative Commons Attribution 4.0 International License., pp. 95–118. DOI: 10.1146/annurev-marine-040422-092951. URL: https://doi.org/10.1146/annurev-marine-040422-092951.

Thornton, E. B. and R. T. Guza (1983). “Transformation of wave height distribution”. In: *Journal of Geophysical Research* 88.C10, pp. 5925–5938. DOI: 10.1029/JC088iC10p05925.

Valle, A. del et al. (2020). “Mangroves protect coastal economic activity from hurricanes”. In: *Proceedings of the National Academy of Sciences* 117.1, pp. 265–270. DOI: 10.1073/pnas.1911617116.

van Rooijen, A. A. et al. (2016). “Modeling the effect of wave-vegetation interaction on wave setup”. In: *Journal of Geophysical Research: Oceans* 121.6, pp. 4333–4352. DOI: 10.1002/2015JC011392.

van Veelen, Thomas J. et al. (2020). “Experimental study on vegetation flexibility as control parameter for wave damping and velocity structure”. In: *Coastal Engineering* 157, p. 103648. DOI: 10.1016/j.coastaleng.2020.103648.

van Wesenbeeck, Bregje K., Vincent T. M. van Zelst, et al. (2025). “Quantifying Uncertainty in Wave Attenuation by Mangroves to Inform Coastal Green Belt Policies”. In: *Communications Earth & Environment*. Article in press. DOI: 10.1038/s43247-025-02178-4. URL: https://doi.org/10.1038/s43247-025-02178-4.

van Wesenbeeck, Bregje K., Guido Wolters, et al. (2022). “Wave attenuation through forests under extreme conditions”. In: *Scientific Reports* 12.1, p. 1884. DOI: 10.1038/s41598-022-05753-3.

van Zelst, Vincent T. M. et al. (2021). “Cutting the costs of coastal protection by integrating vegetation in flood defences”. In: *Nature Communications* 12.1, p. 6533. DOI: 10.1038/s41467-021-26887-4. URL: https://doi.org/10.1038/s41467-021-26887-4.

Vries, J. S. M. Van Thiel de (2009). “Dune erosion during storm surges”. PhD thesis. Delft, Netherlands: Faculty of Civil Engineering and Geosciences, Delft University of Technology.

Vuik, V. et al. (2018). “Stem breakage of salt marsh vegetation under wave forcing: a field and model study”. In: *Estuarine, Coastal and Shelf Science* 200, pp. 41–58. DOI: 10.1016/j.ecss.2017.09.028.

Vuik, Vincent et al. (2016). “Nature-based flood protection: the efficiency of vegetated foreshores for reducing wave loads on coastal dikes”. In: *Coastal Engineering* 116, pp. 42–56. DOI: 10.1016/j.coastaleng.2016.06.001.

Wamsley, T. V. et al. (2010). “The potential of wetlands in reducing storm surge”. In: *Ocean Engineering* 37.1, pp. 59–68. DOI: 10.1016/j.oceaneng.2009.07.018.

Wikipedia contributors (2024). *Mangrove — Wikipedia, The Free Encyclopedia*. Accessed: 2025-05-17. URL: https://en.wikipedia.org/wiki/Mangrove.

Winterwerp, Johan C., Thorsten Albers, et al. (2020). “Managing erosion of mangrove-mud coasts with permeable dams – lessons learned”. In: *Ecological Engineering* 158, p. 106078. DOI: 10.1016/j.ecoleng.2020.106078. URL: https://doi.org/10.1016/j.ecoleng.2020.106078.

Winterwerp, Johan C., Annalise Bayney, et al. (2025). “Mangrove recovery by habitat restoration using nature-based solutions”. In: *Ecological Engineering* 212, p. 107520. DOI: 10.1016/j.ecoleng.2025.107520. URL: https://doi.org/10.1016/j.ecoleng.2025.107520.

Worthington, Thomas A. et al. (2020). “A global biophysical typology of mangroves and its relevance for ecosystem structure and deforestation”. In: *Scientific Reports* 10, p. 14652. DOI: 10.1038/s41598-020-71478-w. URL: https://doi.org/10.1038/s41598-020-71478-w.

Wu, Weiming et al. (2011). *Phase I Report for SERRI Project No. 80037: Investigation of Surge and Wave Reduction by Vegetation*. Tech. rep. SERRI Report 80037-01. Lab. Publ. 1, 315 pp. Oak Ridge, Tennessee: Oak Ridge National Laboratory.

XBeach Manual (2025). *XBeach Manual: Hydrodynamics Options*. Accessed: 2025-09-08. URL: https://xbeach.readthedocs.io/en/latest/xbeach_manual.html#.

Yin, Zegao et al. (2020). “Wave attenuation by rigid emergent vegetation under combined wave and current flows”. In: *Ocean Engineering* 213, p. 107632. ISSN: 0029-8018. DOI: 10.1016/j.oceaneng.2020.107632. URL: https://doi.org/10.1016/j.oceaneng.2020.107632.

A

Theoretical background on ocean waves

A.1. Introduction to ocean waves

Ocean waves are defined as all sea surface variations that are generated in the oceans on different timescales (Bosboom and Stive 2023). A simple way to represent wave motion is using a sine or cosine function, which can describe either spatial variation at a fixed time or temporal variation at a fixed location. These two perspectives are illustrated in Figure A.1.

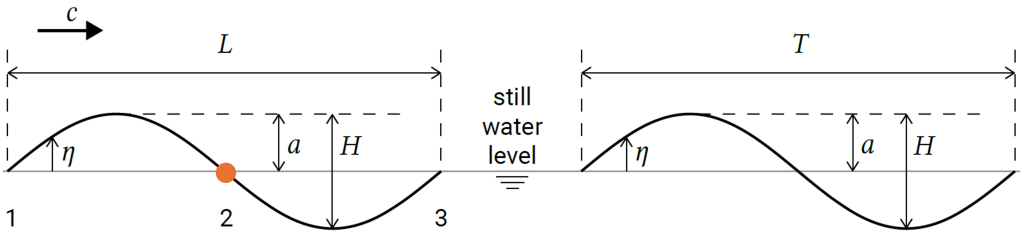

Figure A.1: Left: spatial variation of the water surface elevation along the wave propagation direction at a fixed time. Right: temporal variation of the water level at a fixed location (location 2). Figure from Bosboom and Stive (2023).

The wave height H is the vertical distance between the wave crest and trough, and equals twice the amplitude a for a sinusoidal wave: $H = 2a$. The wave period T is the time between successive crests passing a fixed point, with its inverse being the frequency $f = 1/T$. The wavelength L is the distance between successive crests along the direction of propagation x, and it represents the distance a wave travels in one period. The wave steepness is defined as the ratio H/L.

The surface elevation η of a sinusoidal wave can be described as:

$$\eta(x,t) = a\sin(\omega t - kx)$$

where ω is the angular frequency and k is the wave number, defined as:

$$k = \frac{2\pi}{L}, \quad \omega = \frac{2\pi}{T}$$

The units of ω and k may be expressed as 1/s and 1/m. The wave speed c is given by:

$$c = \frac{L}{T} = \frac{\omega}{k}$$

Ocean waves can be classified depending on their disturbing force (i.e., their mechanism of generation), restoring force (i.e., their mechanism that dampens wave motions), and length (represented by

wavelength or wave period) (Bosboom and Stive 2023). Figure A.2 shows the classification as a function of their wave period and energy level. Based on the primary disturbing force, we will focus on two wave types: wind waves and storm surges.

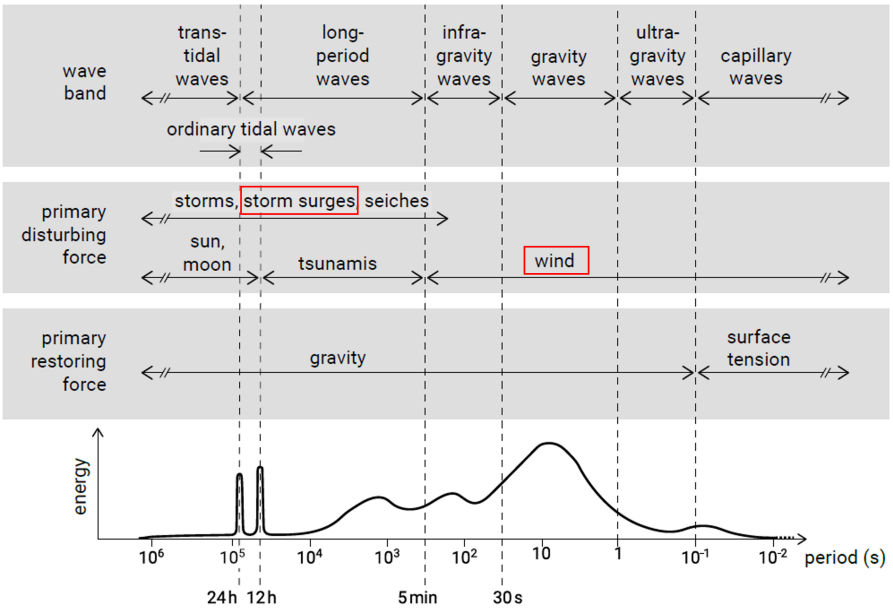

Figure A.2: Sketch showing the relative energy distribution of ocean waves as a function of wave period. The top section classifies waves by wavelength, the middle by generating force, and the bottom by restoring force. Figure adapted from Bosboom and Stive (2023).

A.2. Wind waves

Wind-generated gravity waves are classified as waves with periods ranging from 0.25 to 30 seconds. They are driven by wind and restored by gravity. Local winds produce short, irregular waves known as 'sea'. As these waves travel away from their origin, they undergo frequency dispersion and damping, gradually forming longer, lower, faster, and more regular waves called 'swell'. In wind waves, infragravity waves are often generated by groups of waves in shallow water, producing oscillations such as surf beat. They are long-period gravity waves with durations ranging from 30 seconds to 5 minutes, which is comparable to the length of a wave group.

This section elaborates thoroughly on the basic concept of wind waves. The primary reference of this section is based on the Coastal Dynamics book by Bosboom and Stive (2023).

A.2.1. Wave characteristics

In the real world, the wind wave indeed has an irregular character as opposed to the single sine signal as shown in Figure A.1. These irregular waves can be described statistically over short time periods and are therefore treated as a random stationary process. There are two main approaches to characterize wave records: time series analysis and spectral analysis.

A commonly used parameter for wave characterization is the significant wave height, denoted as $H_{1/3}$ or H_s, which represents the average height of the highest one-third of all waves occurring in a particular time period (McIvor et al. 2012). In spectral analysis, this is given by $H_s = H_{1/3} = 4\sqrt{m_0}$, where m_0 is the zeroth moment of the wave spectrum (i.e., the area under the variance density spectrum). The root-mean-square wave height is defined as $H_{rms} = 2\sqrt{2}\sqrt{m_0}$ in spectral terms.

Wave energy is another key parameter. For a regular wave, the mean wave energy per unit surface area is $E = \frac{1}{2}\rho g a^2 = \frac{1}{8}\rho g H^2$, where a is the wave amplitude. For an irregular wave field, the energy is expressed as $E = \rho g m_0 = \frac{1}{8}\rho g H_{rms}^2$ (Bosboom and Stive 2023). Wave attenuation occurs when they lose energy, resulting reduction in wave height (McIvor et al. 2012).

A.2.2. Wave transformation

Waves are transforming as they approach the shore. The effect of the sea bed, changing from deep into intermediate and shallow water, affects the waves' attributes, such as their height, length, and direction, until they finally break and lose their energy. We consider a linear wave propagation in this process, in which the local wave characteristics are described by linear wave theory. In this part, we will only focus on a certain wave transformation process that is relevant to the topic, called shoaling and wave breaking.

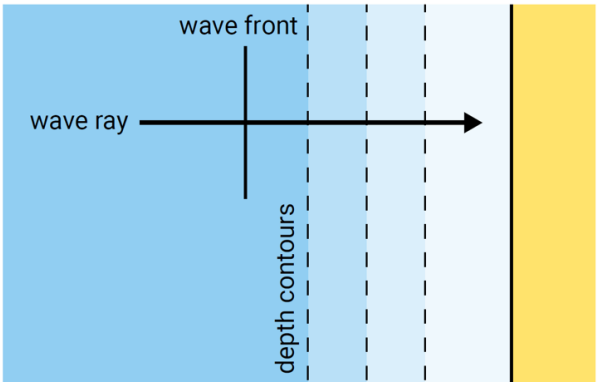

Figure A.3: Normally incident waves with parallel depth contours. Figure from Bosboom and Stive (2023).

First, understanding the fundamentals of energy balance is important. Wave transformation is commonly described using the spectrally integrated energy balance, which provides insight into how wave properties evolve. In the absence of currents, wave energy is conserved, and the energy balance applies. However, when currents are present, energy is exchanged between waves and flow, and wave action (E/ω) becomes the conserved quantity. For conceptual clarity, Box 1 explains the energy balance without currents. Equation A.1 shows that the dissipation term D accounts for processes like wave breaking, bottom friction, and interactions with vegetation such as mangroves.

Box 1: Energy balance equation

In the absence of currents, wave energy is conserved and evolves according to:

$$\underbrace{\frac{\partial E}{\partial t}}_{\text{change of energy}} + \underbrace{\frac{\partial}{\partial x}\left(E c_g \cos\theta\right)}_{\text{import of energy in } x\text{-direction}} + \underbrace{\frac{\partial}{\partial y}\left(E c_g \sin\theta\right)}_{\text{import of energy in } y\text{-direction}} = \underbrace{S - D}_{\text{gain of energy}} \tag{A.1}$$

Here, $E = \frac{1}{8}\rho g H_{\mathrm{rms}}^2$ is the wave energy, c_g the group velocity, and θ the wave direction. S represents wind input (often negligible nearshore), while D includes dissipation from wave breaking, bottom friction, or vegetation.
Under stationary wave and simple alongshore uniform coast conditions, the equation simplifies along a wave ray s to:

$$\frac{d}{ds}(E c_g) = -D_f - D_w \tag{A.2}$$

where D_f is near-bed shear stress induced by wave orbital motion dissipation (generally very small) and D_w represents wave dissipation due to breaking.

As waves enter shallower water, the shoaling process begins, which increases the wave height (H) as they travel. However, there is a certain limit at which the shoaling process ends - the wave breaking. As wave height (H) increases, the decrease in water depth leads to a lower wave celerity, hence its wavelength (L). Therefore, wave steepness (H/L) increases, and often this breaking condition is described by a crest angle of about 120°. In addition to that, wave particle velocity near the surface also increases as the wave height increases. The waves break when the horizontal particle velocity

near the surface of the waves exceeds the wave celerity. Box 2 presents the detailed explanation of shoaling and wave breaking process, as well as the related formulation.

Box 2: Shoaling and Wave Breaking

Shoaling
As waves approach shallower regions (Figure A.3), their energy flux is conserved in the absence of breaking or dissipation:

$$U = Ec_g = Enc = \text{constant} \tag{A.3}$$

U is the wave power per unit width [J/(m·s)], E is the wave energy density [J/m²], c_g and c are the group and phase velocities [m/s], and $n = c_g/c$.

Wave shoaling—an increase in wave height due to decreasing depth—is described by:

$$\frac{H_2}{H_1} = \sqrt{\frac{n_1 c_1}{n_2 c_2}} \tag{A.4}$$

Wave Breaking
As wave steepness increases in shallow water, breaking occurs when a critical wave height-to-depth ratio is exceeded. The maximum value is given by Miche (1944) for a regular wave:

$$\gamma = \left(\frac{H}{h}\right)_{\text{max}} = \frac{H_b}{h_b} \approx 0.88 \tag{A.5}$$

Assuming Rayleigh-distributed (irregular) waves ($H_{\max} \approx 2H_s$), this translates to:

$$\gamma = \frac{H_s}{h} \approx 0.4\text{–}0.5 \tag{A.6}$$

Effect of Bed Slope
The Iribarren number, defined as:

$$\xi = \frac{\tan\alpha}{\sqrt{H_0/L_0}}, \tag{A.7}$$

Irribaren number captures the influence of bed slope $\tan\alpha$ relative to deep-water wave height H_0 and wavelength L_0. Based on this parameter, waves can be classified as:

Iribarren Number ξ	**Breaker Type**	**Breaker Index** γ
$\xi < 0.5$	Spilling	$\gamma \approx 0.6\text{–}0.8$
$0.5 < \xi < 3.3$	Plunging	$\gamma \approx 0.8\text{–}1.2$
$\xi > 3.3$	Collapsing or surging	minimal or no breaking

A.2.3. Wave asymmetry and skewness

After considering linear wave propagation and wave transformation processes such as shoaling and breaking, we now examine the non-linear transformation of wave shapes. As waves propagate toward the shore, shoaling occurs, leading not only to an increase in wave height but also to typical non-linear modifications of the wave shape. To describe them, non-linear wave theories such as Stokes, cnoidal, and Boussinesq formulations are used (Bosboom and Stive 2023). This results in two primary asymmetry effects: skewness and asymmetry. The Ursell parameter $U = HL^2/h^3$ can be used as a skewness and asymmetry indicator.

Skewness

Skewness is described as a gradual peaking of the wave crest and flattening of the trough, representing asymmetry relative to the horizontal axis of the wave signal. For example, the skewed wave profile can be described by a sum of sinusoidal components with higher harmonics, such as in Stokes' second-order theory as written in equation A.8. Here, the higher harmonic remains phase-locked to the primary wave, resulting in sharper crests and flatter troughs (i.e., positive skewness).

$$\eta = \hat{\eta}_1 \cos(\omega t - kx) + \hat{\eta}_2 \cos\big(2(\omega t - kx)\big) \tag{A.8}$$

Asymmetry

Asymmetry refers to a pitched-forward wave shape due to the steepening of the wave face as it approaches breaking, representing asymmetry relative to the vertical axis of the wave signal. This wave shape arises when the wave crest moves faster than the trough, as described by the propagation speeds of shallow water waves: $c_{\text{crest}} = \sqrt{g(h+a)}$ and $c_{\text{trough}} = \sqrt{g(h-a)}$. This causes the wave face to steepen relative to the back, producing a sawtooth-like shape. Such asymmetry requires a phase shift between the harmonics (for example, a second harmonic that is forward phase-shifted relative to the primary). This type of asymmetry cannot be captured by standard Stokes waves. As shown in Figure A.4, the left panel illustrates wave skewness, while the right panel shows asymmetry due to phase shifts.

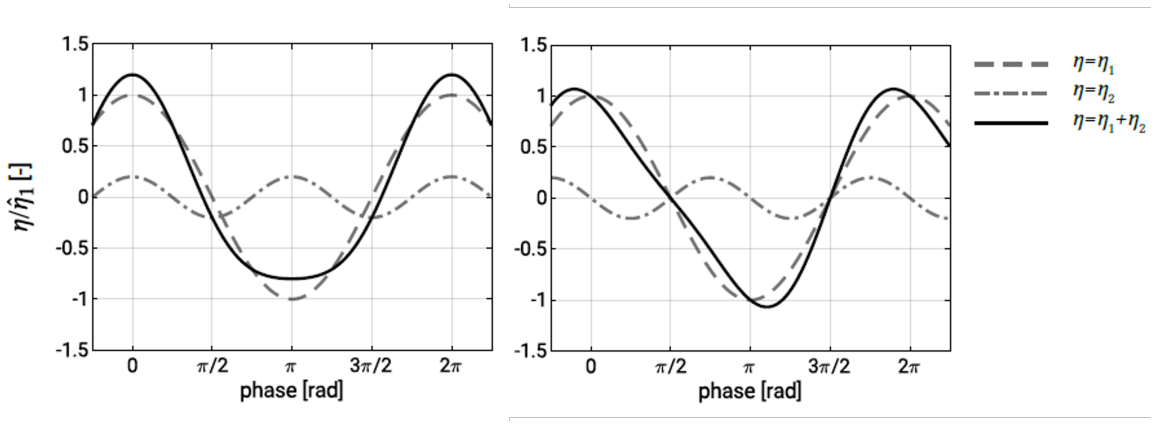

Figure A.4: Wave skewness and asymmetry illustrated using higher harmonics. **Left:** A second-order Stokes wave with phase-locked harmonics ($\hat{\eta}_2/\hat{\eta}_1 = 0.2$) shows crest-trough asymmetry (skewness). **Right:** An asymmetric wave with the second harmonic phase-shifted by $90°$, producing a pitched-forward profile (time asymmetry). Illustration from Bosboom and Stive (2023).

A.2.4. Wave orbital velocity

Beneath the wave surface, fluid particles follow orbital paths associated with the motion of the water surface. According to linear wave theory, these orbits are nearly circular in deep water ($h/L > 0.5$), with diameters that decrease with depth. In intermediate water depths, the orbits become ellipses that flatten toward the seabed, resulting in predominantly horizontal motion near the bottom. Figure A.5 describes the water particle movement in intermediate water depth. In shallow water ($h/L < 1/20$), the vertical displacement becomes negligible, while the horizontal motion remains nearly uniform throughout the depth. The horizontal orbital velocity is described by the equations A.9 and A.10.

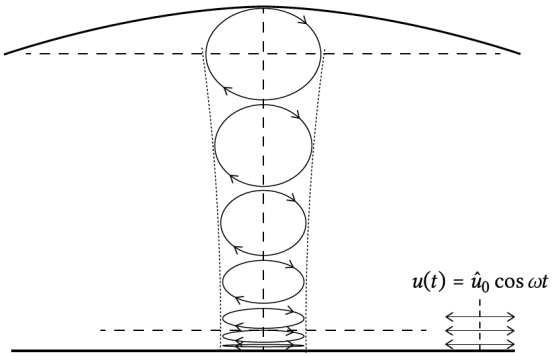

Figure A.5: Illustration of water particle orbits beneath a wave in intermediate water depth. The paths become elliptical and flatten toward the bottom, indicating predominantly horizontal motion near the seabed. Figure from Bosboom and Stive (2023).

$$u(t) = \hat{u}(z)\cos(\omega t) \tag{A.9}$$

$$\hat{u}(z) = \frac{\omega a \cosh k(h+z)}{\sinh kh} \tag{A.10}$$

with:

- ω = angular frequency = $2\pi/T$ (rad/s),
- a = wave amplitude (m),
- k = wavenumber = $2\pi/L$ (rad/m),
- h = water depth (m),
- z = vertical coordinate (positive upward, $z = 0$ at still water level).

Figure A.6 illustrates the vertical profiles of amplitude velocity $\hat{u}$.

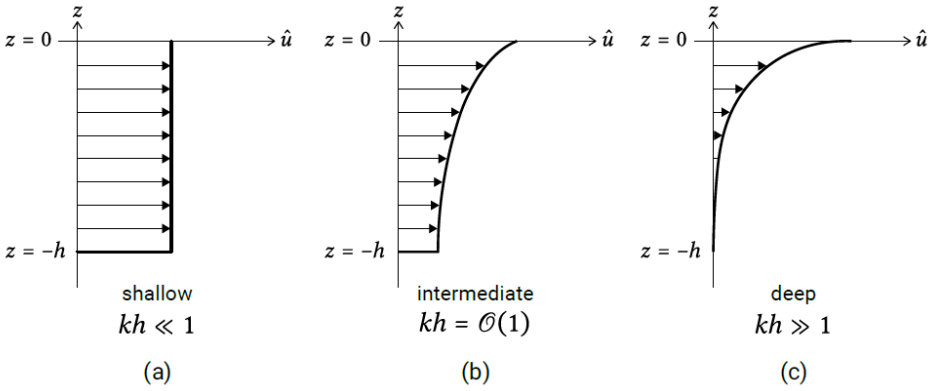

Figure A.6: Vertical profiles of horizontal orbital velocity amplitude $\hat{u}(z)$ under linear wave theory, showing decay with depth. In shallow water, $\hat{u}(z)$ remains nearly uniform over depth. Figure from Bosboom and Stive (2023).

A.2.5. Wave set-up and set-down process

The explanation of how wave set-up and set-down proceed is presented here. The increase (set-up) and decrease (set-down) of the mean water level due to waves are related to the momentum carried by the waves, the resulting radiation stress, and the wave-induced forces that are thus produced. The following paragraphs present the explanation of the processes.

Wave-induced momentum. Propagating waves not only carry energy, but also momentum. Momentum is defined as the product of mass and velocity, which means that the mass in motion brings momentum. The total amount of momentum or mass flux (q) of the wave per unit surface area is obtained by integration over the depth of the mass density (ρ) between wave trough and wave crest, and velocity (u). In the surf zone, it is assumed that the mass flux (q) consists of two parts: due to the progressive character of the waves and due to the surface roller in breaking waves. This formula is described in equation A.11. In the case of a closed boundary, such as a coastline, there can be no net mass transport across the vertical boundary — otherwise, water would accumulate along the shore. This means that any onshore mass flux above the wave trough must be balanced by a compensating flow below the trough level: a return current. As a result, the cross-shore depth-averaged velocity below the wave trough is described in equation A.12. Figure A.7 shows the process of return current.

$$q_{\text{drift}} = q_{\text{non-breaking}} + q_{\text{roller}} = \frac{E}{c} + \frac{\alpha E_r}{c} \tag{A.11}$$

$$U_{\text{below trough}} = -\frac{q_{\text{drift},x}}{\rho h} = -(\frac{E}{\rho h c} + \frac{\alpha E_r}{\rho h c}) \tag{A.12}$$

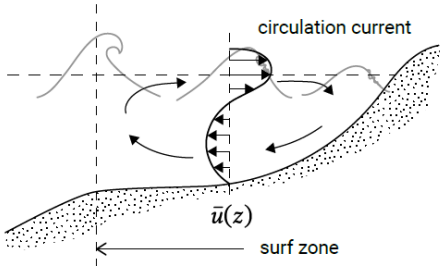

Figure A.7: Illustration of undertow: the compensating seaward-directed flow below the wave trough that balances the onshore mass transport above the trough in the surf zone. Figure from Bosboom and Stive (2023).

Radiation stress. Radiation stress is the depth-integrated and wave-averaged flux of momentum due to waves. When there is a spatial change in this wave-induced momentum flux, wave forces act on the water, affecting mean currents and water levels. These forces cause set-down (a lowering of the mean water level in the shoaling zone) and set-up (a rise in the surf zone). According to linear wave theory, under alongshore uniform conditions, the radiation stress components for waves travelling at an angle θ are given in equations A.13 to A.15, where S_{xx} and S_{yy} are the normal components, S_{xy} and S_{yx} are the shear components, n is the ratio of group velocity to phase velocity, and E is the wave energy density. Figure A.8 illustrates the radiation stress components and their formula as well.

$$S_{xx} = \left(n - \frac{1}{2} + n\cos^2\theta\right) E, \tag{A.13}$$

$$S_{yy} = \left(n - \frac{1}{2} + n\sin^2\theta\right) E, \tag{A.14}$$

$$S_{xy} = S_{yx} = n\cos\theta\sin\theta\, E, \tag{A.15}$$

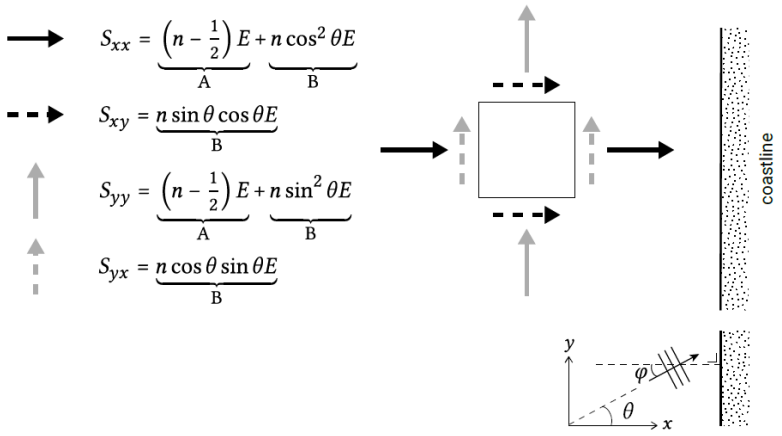

Figure A.8: Radiation stress components according to linear wave theory. Situation sketch for an alongshore uniform coast with depth contours parallel to the y-axis. 'A' indicates the pressure contribution; 'B' the contribution due to advection by the horizontal particle velocity. Figure from Bosboom and Stive (2023).

Wave-induced forces. Horizontal gradients in radiation stress give rise to wave-induced forces on the water, which can lead to mean water level changes such as set-up and set-down. The net force in the x-direction is described by equation A.16. For an alongshore uniform coastline, there are no gradients in the y-direction, so this reduces to equation A.17. In this study, we focus only on the x-direction (cross-shore) component, as it is most relevant to our analysis.

$$F_x = -\left(\frac{\partial S_{xx}}{\partial x} + \frac{\partial S_{xy}}{\partial y}\right) \tag{A.16}$$

$$F_x = -\frac{dS_{xx}}{dx} \tag{A.17}$$

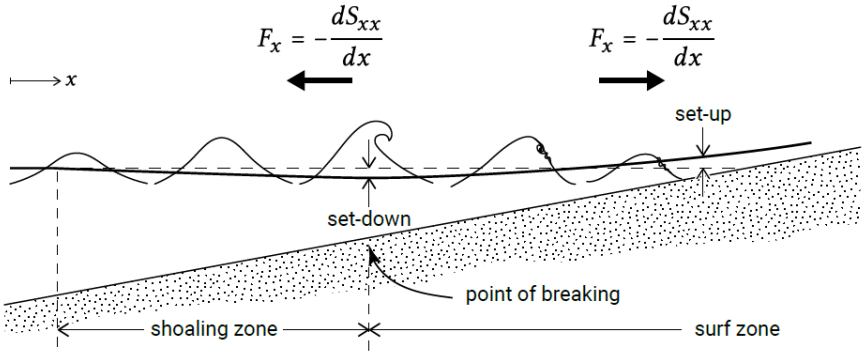

Figure A.9: In the shoaling zone, increasing S_{xx} drives offshore forces, lowering the mean water level (set-down). In the surf zone, decreasing S_{xx} leads to onshore forces, raising the water level toward the shore (set-up). Figure from Bosboom and Stive (2023).

Cross-shore momentum balance: wave set-up and set-down. For an alongshore uniform coast, equation A.17 applies, and the cross-shore forces and momentum balance each other. As waves shoal, the increasing radiation stress (positive gradient) leads to offshore-directed forces, lowering the mean water level (set-down). After breaking, the decreasing radiation stress (negative gradient) results in onshore-directed forces, raising the water level (set-up). This can be described by the 1D momentum equation A.18, which simplifies under stationary conditions, with no surface stress, bed friction, velocity

gradients, or horizontal mixing, to equation A.19. The water level gradient thus directly reflects the direction of external forces. The illustration of this process is shown in Figure A.9.

$$\underbrace{\frac{\partial U}{\partial t}}_{\text{Local acc.}} + \underbrace{U\frac{\partial U}{\partial x}}_{\text{Advective acc.}} = \underbrace{\frac{\partial}{\partial x}\left(D_h \frac{\partial U}{\partial x}\right)}_{\text{Horizontal mixing}} + \underbrace{\frac{\tau_{sx}}{\rho h}}_{\text{Surface stress}} + \underbrace{\frac{\tau_{bx}}{\rho h}}_{\text{Bed shear}} - \underbrace{g\frac{\partial \eta}{\partial x}}_{\text{Water level slope}} + \underbrace{\frac{F_x}{\rho h}}_{\text{External force}} \tag{A.18}$$

$$\underbrace{g\frac{\partial \eta}{\partial x}}_{\text{Water level slope}} = \underbrace{\frac{F_x}{\rho h}}_{\text{External force}} \tag{A.19}$$

A.3. Infragravity (IG) waves

As described in Figure A.2, the IG waves are low-frequency waves with periods from 30 seconds to 5 minutes, much longer than the typical wind waves and quite comparable to the length of a wave group. IG waves are often generated by the groupiness of the short-waves, producing oscillations such as surf beat. Based on its mechanism approaching the shoreline, there are two types of IG waves: the bound long waves and the free long waves.

A.3.1. Bound long waves

Wave groups cause variations in radiation stress, leading to local set-downs under high waves and set-ups under low waves. This surface response, directly linked to the wave group pattern, is called bound long waves. As waves move onshore, their amplitude scales roughly as $\eta_{\text{lb}} \sim h^{-5/2}$, meaning long-wave height increases strongly as depth decreases (Schipper 2024). These incoming bound long waves happen as long as there is groupiness of the short waves, which appear stronger before they break.

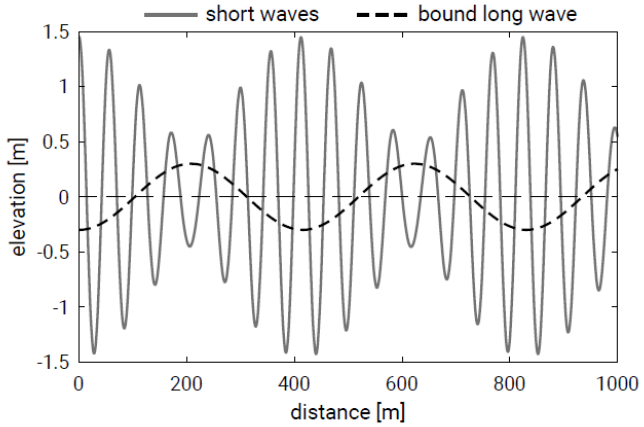

Figure A.10: Illustration of bound long waves: wave groups induce variations in radiation stress, creating a set-down under high waves and a set-up under low waves. Figure from Bosboom and Stive (2023).

A.3.2. Free long waves

When wave breaking occurs in the surf zone, the wave groups that sustain bound long waves diminish, releasing these bound long waves as free long waves. Breaking reduces wave groupiness, making short waves more uniform and eliminating the varying radiation stress that previously governed the bound long waves. As a result, short waves no longer determine the long-wave surface elevation, and the free long waves propagate independently at their own frequency and speed. Free long waves travel at $c = \sqrt{gh}$, typically faster than the group speed of bound long waves, $c_g = nc$, with $0.5 < n < 1$. As they move into shallower water, free long waves shoal according to $\eta_{\text{lf}} \sim h^{-1/4}$ (Green's law), meaning decreasing depth leads to higher wave amplitudes, though with a relatively weak dependence compared to bound long waves. Unlike bound long waves, which consist only of incoming components

tied to wave groups, free long waves include both incoming and outgoing (reflected) parts (Schipper 2024).

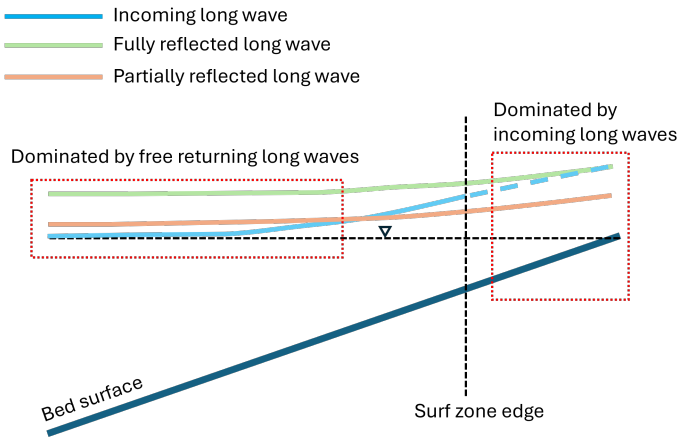

Figure A.11: Depth dependence of bound and free long waves: incoming bound long waves amplify rapidly nearshore ($\sim h^{-5/2}$), while reflected free long waves show weaker scaling ($\sim h^{-1/4}$). Near the shoreline, long-wave action is dominated by incoming waves; at intermediate depths, reflected waves prevail. Figure adapted from Schipper (2024) after Henderson, Guza, et al. (2006).

B

Post-processing approach for vegetation force estimation

This section presents the inclusion of $F_{v,m}$ and $F_{v,w}$ into the `SFINCS-SnapWave` model results through a post-processing approach. The initial wave setup results from Chapter 4 will be corrected by explicitly adding the effects of vegetation-induced wave forces. Similar to the previous chapter, this section focuses on a single representative case, S12, with $H_s = 6.7$ cm and $T_p = 2.4$ s.

The wave shape model is employed to approximate the wave orbital velocity and compute the vegetation force due to nonlinear wave orbital motion, $F_{v,w}$. Additionally, the vegetation force due to mean flow, $F_{v,m}$, is also included by estimating the mean flow velocity using the undertow formula within the vegetated area. The result of this approach indeed would not be accurate enough as there are no coupling feedback between momentum equation and wave energy balance. This approach is performed to explore the possible quantity of the vegetation force effect on water levels.

B.1. $F_{v,w}$ estimation

As shown in equation 2.10, the calculation of $F_{v,w}$ primarily requires the time series of the depth-averaged wave orbital velocity, u_w. The nonlinearity of u_w is critical: if the velocity were purely linear and symmetric over time, the integral over a wave period would vanish since the other variables are constant. This highlights the necessity of accounting for wave nonlinearity as waves propagate through vegetation, modifying the shape of the velocity signal and thus the drag force. The following steps outline the procedure to compute u_w using the wave shape model, consistent with van Rooijen et al. (2016), as well as the final result of $F_{v,w}$.

B.1.1. Reconstruction of the nonlinear wave orbital velocity

First, the theory behind the wave shape model is explained. According to van Rooijen et al. (2016), the wave shape model is used to account for the effects of nonlinear sea-swell waves, ultimately enabling the calculation of the vegetation-induced force $F_{v,w}$. This approach is similar to the model proposed by Vries (2009), which builds upon the wave shape description of Rienecker and Fenton (1981) and applies the empirical formulation by Ruessink et al. (2012) to reconstruct a depth-averaged orbital velocity time series over a wave period.

It is important to note that the wave shape model was originally developed using data from non-vegetated coastal environments. As such, its application in vegetated settings introduces some uncertainty. Nevertheless, van Rooijen et al. (2016) demonstrated that the model can still accurately reproduce wave setup in vegetated conditions. Therefore, this approach is considered appropriate for use in the present study.

Following the parameterisation by Rienecker and Fenton (1981), the shape of sea-swell waves is reconstructed as a weighted sum of eight sine and cosine harmonics:

$$u_w(t) = \sum_{i=1}^{8} [wA_i \cos(i\omega t) + (1-w)A_i \sin(i\omega t)] \tag{B.1}$$

where u_w is the wave orbital velocity, A_i is the amplitude of the i-th harmonic, ω is the angular wave frequency, and w is a weighting function.

The weight function (w) follows an empirical relationship that accounts for wave nonlinearity as a function of the Ursell number and phase ϕ based on the formulation of Ruessink et al. (2012). It is expressed as:

$$w = 1 - \frac{\phi}{\pi} \tag{B.2}$$

$$\phi = \frac{\pi}{2}\left(1 - \tanh\left(\frac{0.815}{Ur^{0.672}}\right)\right) \tag{B.3}$$

$$Ur = \frac{3}{8}\frac{H_{m0}k}{(kh)^3} \tag{B.4}$$

The harmonic amplitudes A_i are determined using a precomputed lookup table from Rienecker and Fenton (RF table), developed from stream function wave theory (Rienecker and Fenton 1981). This table provides near-bed velocity amplitudes A_i for a range of nondimensional wave heights ($H_0 = H_{rms}/h$) and nondimensional wave periods ($T_0 = T_p * \sqrt{g/h}$).

Given this workflow, we indeed need to extract the `SFINCS-SnapWave` model initial output: the significant wave height (H_{m0}), peak period (T_p), and water depth (h). These are then used to calculate the angular frequency (ω), wave number (k), and Ursell number (Ur). Lastly, the weight function (w) is computed, which is essential for constructing the time series of u_w. Figure B.1 presents the summary of the computation result.

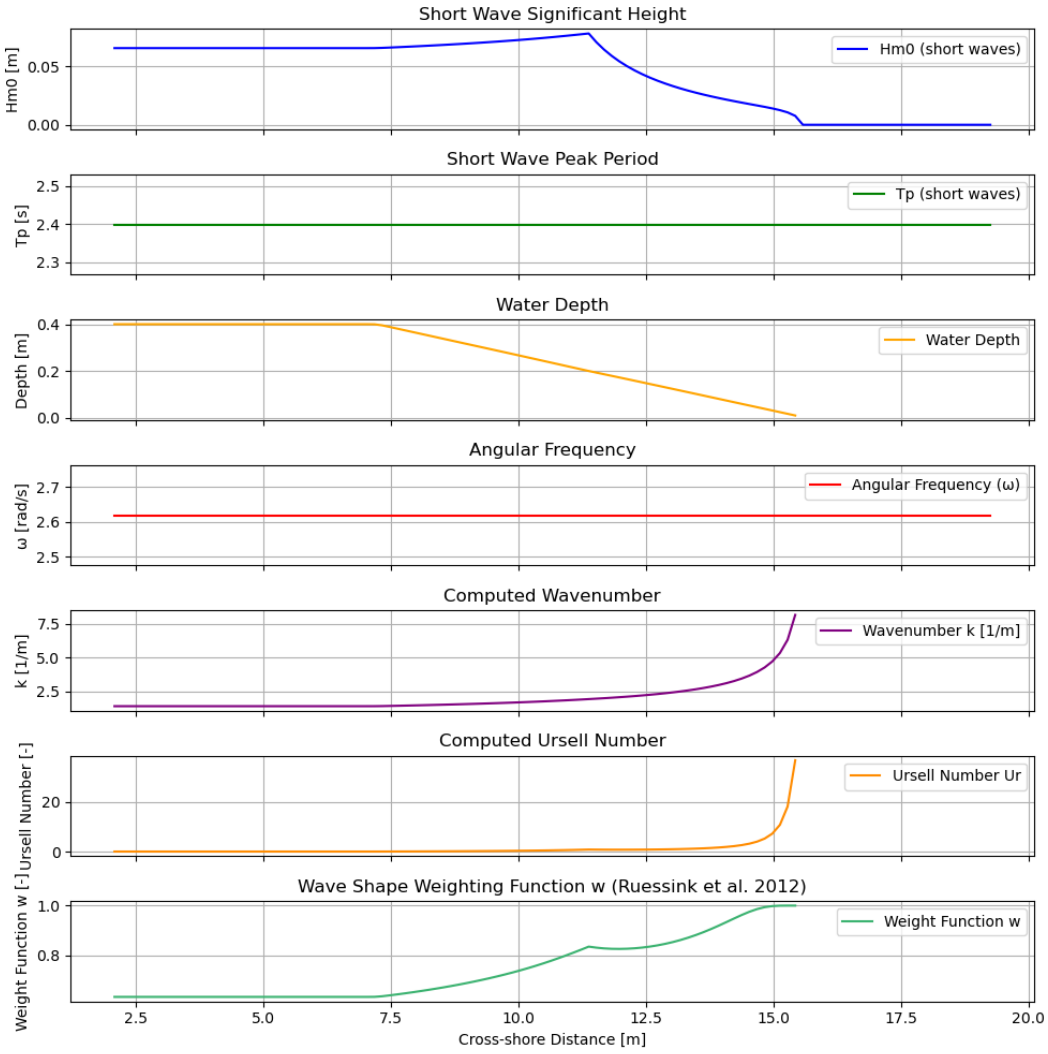

Figure B.1: Computation results of the model output

Once we have the wave function parameter (w), we only need to find the other parameter: A_i, to finally reconstruct the equation B.1. A_i can be determined by doing bilinear interpolation on the precomputed Rienecker-Fenton (RF) table. Combining these amplitudes with the cosine and sine series adjusted by the weights, it calculates the full time series of $u_w(t)$. Figure B.2 shows the reconstructed nonlinear velocity over the wave period at selected locations along the flume.

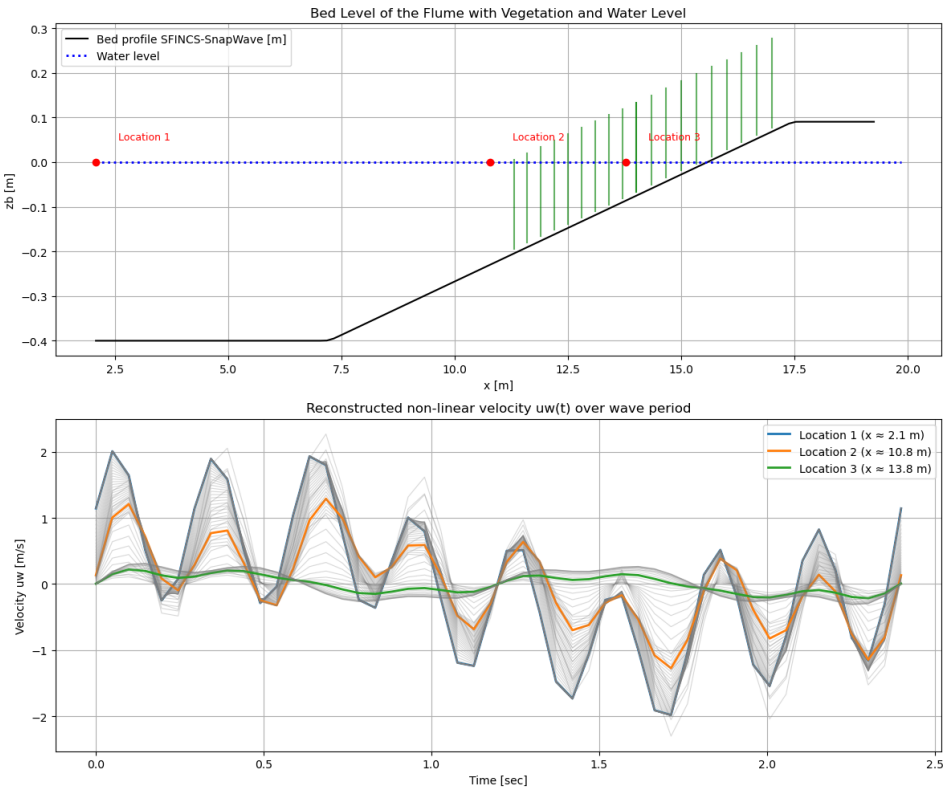

Figure B.2: Reconstructed nonlinear velocity $u_w(t)$ at three representative locations: (1) near the start of the flume, (2) just before the vegetated area, and (3) inside the vegetated area. The figure also includes grey lines showing the velocity time series at other cross-shore locations for context.

B.1.2. Computation of $F_{v,w}$ and its contribution to water level changes

The vegetation-induced wave drag force due to nonlinear wave shape $F_{v,w}$ is computed as:

$$F_{v,w} = \frac{1}{T_{\text{rep}}} \int_0^{T_{\text{rep}}} \frac{1}{2} \rho C_D b_v N_v h_v \, u_w \, |u_w| \, dt \tag{B.5}$$

where the division by T_{rep} provides the time-averaged force over a wave period. The parameter h_v would be constant (not changing over time) by selecting the minimum value of the initial water depth and the vegetation height. The resulting unit of $F_{v,w}$ is [kg/(m·s^2)]. As a note, the $F_{v,w}$ sign is negative due to the direction of the force against the incoming wave.

The corresponding water level gradient can be obtained from a simplified momentum balance:

$$\underbrace{\frac{\partial \eta}{\partial x}}_{\text{Water level slope}} = \frac{1}{\rho g h} \underbrace{F_v}_{\text{Vegetation drag force}} \tag{B.6}$$

Accordingly, the water level change induced by $F_{v,w}$ can be determined by integrating the slope along the cross-shore direction:

$$\eta(x) = \int \frac{F_v(x)}{\rho g h(x)} \, dx + \eta_0 \tag{B.7}$$

By applying Equation B.7 to the computed $F_{v,w}$ distribution along the flume, the corresponding water level contribution $\eta_{v,w}$ can be obtained. This additional set-down is then superimposed on the initial wave setup η_{initial} to evaluate the combined effect of vegetation-induced drag on the total water level.

The result allows for a direct comparison between the modelled setup with and without the inclusion of $F_{v,w}$, and is also plotted against laboratory measurements, which is shown in Figure B.3.

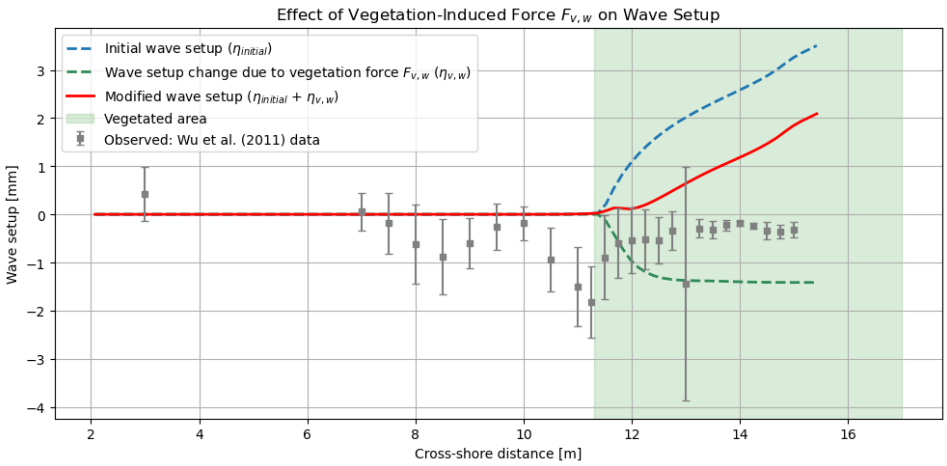

Figure B.3: Comparison of wave setup profiles with and without the effect of vegetation-induced force $F_{v,w}$. The initial wave setup η_{initial} (blue line) is adjusted using the computed contribution from $\eta_{v,w}$ due to $F_{v,w}$ (green line). The red dashed line shows the modified water level after incorporating $F_{v,w}$, while the grey markers represent laboratory measurements in vegetated conditions from Wu et al. (2011).

B.2. $F_{v,m}$ estimation

The vegetation-induced wave drag force due to mean flow $F_{v,m}$ can be computed as:

$$F_{v,m} = \frac{1}{2}\rho C_D b_v N_v h_v \, u_E \, |u_E| \tag{B.8}$$

The resulting unit of $F_{v,m}$, similar to $F_{v,w}$ in the previous section, is [kg/(m·s^2)]. In this case, we need to approximate the u_E to obtain $F_{v,m}$. Ideally, u_E has to consist of two components: the mean flow and IG flow. Even though the `SnapWave` could estimate the incoming IG wave, it does not solve the IG wave explicitly, and thus, no IG flow dynamics are solved. Due to this limitation, we consider the u_E by approximating it with the undertow velocity (u_u) formula. This force may add to the water level at the end of the domain due to its nature that flows back to offshore, hence the force directed on shore (positive sign). Thus, we may expect additional setup due to this $F_{v,m}$ component. The undertow velocity u_u is estimated from momentum considerations:

$$u_u = -\frac{E}{\rho h c} \tag{B.9}$$

E is the wave energy, ρ is the water density, h is the local depth, and c is the phase speed. Using the same approach with $F_{v,w}$, the estimate of water level is obtained by integrating the water level slope along the cross-shore direction as shown in equation B.7. Figure B.4 shows the result of the water level due to $F_{v,m}$ contribution, compared to the initial water level and laboratory measurements. Compared to Figure B.3, it is clearly shown that the influence of $F_{v,m}$ is much less than $F_{v,w}$ on the water level in this case.

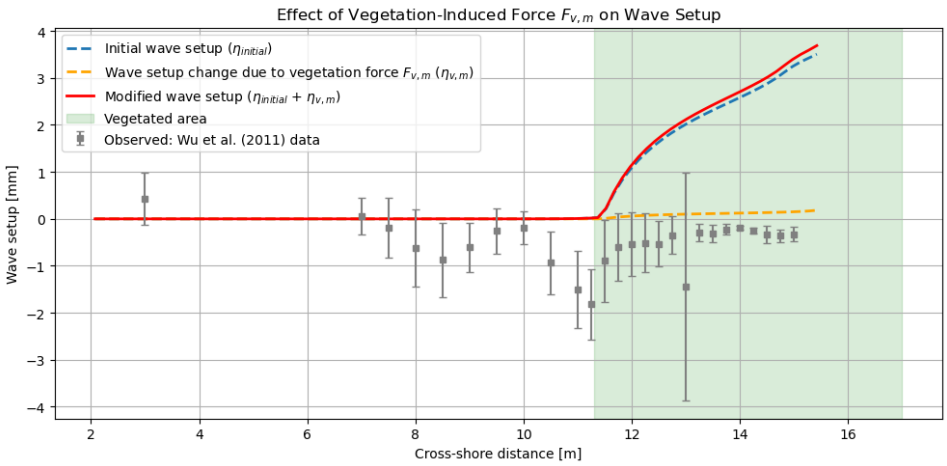

Figure B.4: Comparison of wave setup profiles with and without the effect of vegetation-induced force $F_{v,m}$. The initial wave setup η_{initial} (blue line) is adjusted using the computed contribution from $\eta_{v,m}$ due to $F_{v,m}$ (orange line). The red dashed line shows the modified water level after incorporating $F_{v,m}$, while the grey markers represent laboratory measurements in vegetated conditions from Wu et al. (2011).

B.3. Total water level results

Figure B.5 presents the total wave setup resulting from the combined effects of vegetation-induced drag forces. Three key observations can be drawn from this figure:

1. The nonlinear wave-induced vegetation drag force ($F_{v,w}$) has a substantial influence on the resulting wave setdown. This finding is consistent with previous studies, such as van Rooijen et al. (2016), which emphasize the importance of $F_{v,w}$ in altering wave-driven water levels.
2. In contrast, the contribution of the mean flow drag force ($F_{v,m}$) to the total setup is relatively minor. In this case, $F_{v,m}$ is computed using the undertow velocity, which is directed offshore and thus tends to reduce setup. Ideally, the mean flow component induced by infragravity (IG) wave motions should also be incorporated for a more complete representation. However, due to limitations in the model output, this component could not be resolved in the present analysis.
3. When both $F_{v,w}$ and $F_{v,m}$ are accounted for, the modified water level profile shows a closer agreement with the observed laboratory measurements, particularly due to the dominant influence of $F_{v,w}$ in reducing the wave setup. This improvement highlights the importance of including vegetation-wave interactions in wave setup predictions.

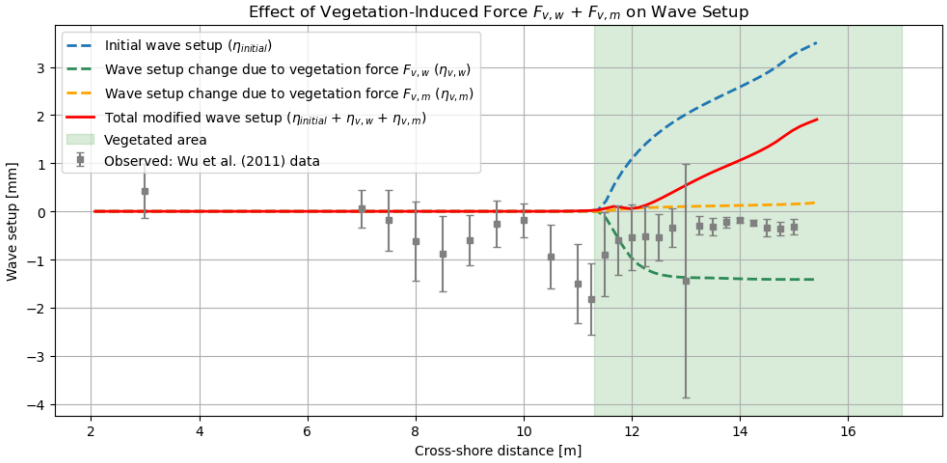

Figure B.5: Comparison of wave setup profiles showing the individual and combined effects of vegetation-induced drag forces. The initial wave setup η_{initial} (blue dashed line) is progressively modified by the contributions from the nonlinear wave-induced drag force $F_{v,w}$ (green dashed line, $\eta_{v,w}$) and the mean flow drag force $F_{v,m}$ (orange dashed line, $\eta_{v,m}$). The resulting total modified wave setup (solid red line) is the sum of all components. Experimental measurements from Wu et al. (2011) are included for comparison (grey markers with error bars).

C

Source code: Improvement implementation of vegetation force in SnapWave

This appendix presents the key subroutines implemented in the SnapWave source code to account for vegetation-induced wave force ($F_{v,w}$). The source code is written in Fortran, modifying the module of snapwave_solver.

Three versions of momeqveg are provided to compute the vegetation-induced nonlinear wave force $F_{v,w}$, and two versions of swvegnonlin to reconstruct the orbital velocity time series u_w (and, optionally, the free-surface oscillation η_w):

- momeqveg **v1** (Listing C.1): one-layer vegetation. This is the version used for the main results in this thesis; no vertical layering and no emergence over the wave cycle.
- momeqveg **v2** (Listing C.2): multi-layer vegetation without emergence. Each vertical section contributes according to its submerged thickness under still-water depth.
- momeqveg **v3** (Listing C.3): multi-layer vegetation with time-varying emergence, using $\eta_w(t)$ to compute the instantaneous submerged thickness per section.
- swvegnonlin **v1** (Listing C.4): reconstructs $u_w(t)$ from the wave-shape model; no computation of η_w.
- swvegnonlin **v2** (Listing C.5): as v1, but additionally returns $\eta_w(t)$ (etaw) for use in the emergence-enabled momeqveg v3.

Listing C.1: Subroutine momeqveg to compute $F_{v,w}$ in SnapWave. This version is used for this thesis result. Only applicable for one layer vegetation.

```
.....
.....
subroutine momeqveg(no_nodes, no_secveg, veg_ah, veg_bstems, veg_Nstems, veg_Cd, depth, rho,
    H, Trep, unl, Fvw)
    ! INput: no_nodes, no_secveg, veg_ah(k,:), veg_bstems(k,:), veg_Nstems(k,:), veg_Cd(k,:),
        depth(k), rho, H(k), Tp(k), unl(k,:), Fvw(k)
    !
    implicit none
    !
    ! Inputs
    integer, intent(in) :: no_nodes, no_secveg
    real*4, intent(in) :: depth ,rho, H, Trep
    real*4, dimension(no_secveg), intent(in) :: veg_ah, veg_bstems, veg_Nstems, veg_Cd
    real*4, dimension(50), intent(in) :: unl
    !
    ! Output
    real*4, intent(out) :: Fvw
```

```
    !
    ! Local variables
    integer :: m, t
    real*4 :: dt, hvegeff, Fvgnlt, integral
    real*4 :: Cd, b, N
    !
    !write(*,*)'Started momeqveg'

    ! Initialize output force
    !
    Fvw = 0.0
    !
    ! Time step within wave period
    !
    dt = Trep / 50.0
    !
    ! Loop over vertical vegetation sections
    do m = 1 , no_secveg
        ! Effective submerged height of vegetation section
        hvegeff = min(veg_ah(m), depth)
        ! Read vegetation parameters
        Cd = veg_Cd(m)
        b = veg_bstems(m)
        N = veg_Nstems(m)
        ! Integrate vegetation drag over wave period using unl
        integral = 0.0
        do t = 1, 50 !50=PPWL
            integral = integral + (0.5 * Cd * b * N * hvegeff * unl(t) * abs(unl(t) ) ) * dt
        enddo
        ! Convert to force per unit mass and sum
        Fvgnlt = -integral / depth / Trep !> units match with F(k) m/s2

        Fvw = Fvw + Fvgnlt
    enddo
    !write(*,*)'Ended momeqveg'

end subroutine momeqveg
```

Listing C.2: Subroutine `momeqveg` to compute $F_{v,w}$ in `SnapWave`. This adapted version is applicable for layering vegetation, without emergence effect.

```
.....
.....
subroutine momeqveg(no_nodes, no_secveg, veg_ah, veg_bstems, veg_Nstems, veg_Cd, depth, rho,
    H, Trep, unl, Fvw)
    ! INput: no_nodes, no_secveg, veg_ah(k,:), veg_bstems(k,:), veg_Nstems(k,:), veg_Cd(k,:),
         depth(k), rho, H(k), Tp(k), unl(k,:), Fvw(k)
    !
    implicit none
    !
    ! Inputs
    integer, intent(in) :: no_nodes, no_secveg
    real*4, intent(in) :: depth ,rho, H, Trep
    real*4, dimension(no_secveg), intent(in) :: veg_ah, veg_bstems, veg_Nstems, veg_Cd
    real*4, dimension(50), intent(in) :: unl
    !
    ! Output
    real*4, intent(out) :: Fvw
    !
    ! Local variables
    integer :: m, t
    real*4 :: dt, hvegeff, Fvgnlt, integral
    real*4 :: aht, ahtold
    real*4 :: Cd, b, N
    !
    !write(*,*)'Started momeqveg'

    ! Initialize output force
    !
    Fvw = 0.0
    !
```

```
    ! Time step within wave period
    !
    dt = Trep / 50.0
    !
    ahtold = 0.0
    ! Loop over vertical vegetation sections
    do m = 1 , no_secveg
        aht = veg_ah(m)
        ! Effective submerged height of vegetation section
        hvegeff = max(depth - ahtold, 0.0)
        ! Read vegetation parameters
        Cd = veg_Cd(m)
        b = veg_bstems(m)
        N = veg_Nstems(m)
        ! Integrate vegetation drag over wave period using unl
        integral = 0.0
        do t = 1, 50 !50=PPWL
            integral = integral + (0.5 * Cd * b * N * min(hvegeff, aht - ahtold) * unl(t) *
                abs(unl(t) ) ) * dt
        enddo
        ! Convert to force per unit mass and sum
        Fvgnlt = -integral / depth / Trep !> units match with F(k) m/s2

        Fvw = Fvw + Fvgnlt

        ahtold = aht
    enddo
    !write(*,*)'Ended momeqveg'

end subroutine momeqveg
```

Listing C.3: Subroutine `momeqveg` to compute $F_{v,w}$ in `SnapWave`. This adapted version is applicable for layering vegetation with emergence effect.

```
.....
.....
subroutine momeqveg(no_nodes, no_secveg, veg_ah, veg_bstems, veg_Nstems, veg_Cd, depth, rho,
    H, Trep, unl, etaw, Fvw)
    ! INput: no_nodes, no_secveg, veg_ah(k,:), veg_bstems(k,:), veg_Nstems(k,:), veg_Cd(k,:),
         depth(k), rho, H(k), Tp(k), unl(k,:), Fvw(k)
    !
    implicit none
    !
    ! Inputs
    integer, intent(in) :: no_nodes, no_secveg
    real*4, intent(in) :: depth ,rho, H, Trep
    real*4, dimension(no_secveg), intent(in) :: veg_ah, veg_bstems, veg_Nstems, veg_Cd !
        veg_ah = TOP of each layer wrt bed (cumulative)
    real*4, dimension(50), intent(in) :: unl, etaw
    !
    ! Output
    real*4, intent(out) :: Fvw
    !
    ! Local variables
    integer :: m, t
    real*4 :: dt, Fvgnlt, integral
    real*4 :: Cd, b, N
    real*4 :: aht, ahtold
    real*4 , dimension(50) :: hvegeff
    !real*4 :: etaw_val
    !
    !write(*,*)'Started momeqveg'

    ! Initialize output force
    !
    Fvw = 0.0
    !
    ! Time step within wave period
    !
    dt = Trep / 50.0
    !
```

```
    ! Loop over vertical vegetation sections
    ahtold = 0.0
    do m = 1 , no_secveg
        aht = veg_ah(m)
        ! Effective submerged height of vegetation section
        !hvegeff = min(veg_ah(m), depth)
        ! Read vegetation parameters
        Cd = veg_Cd(m)
        b = veg_bstems(m)
        N = veg_Nstems(m)

        write(*,*) "shape of etaw =", shape(etaw)
        ! effective vegetation height over wave cycle
        do t = 1, 50
            hvegeff(t) = max( etaw(t) + depth - ahtold , 0.0 )
            !etaw_val = etaw(t)
            !write(*,'(A,F12.5)') "etaw =", etaw_val
        enddo

        ! Integrate vegetation drag over wave period using unl
        integral = 0.0
        do t = 1, 50 !50=PPWL
            integral = integral + (0.5 * Cd * b * N * min(hvegeff(t), aht - ahtold) * unl(t)
                * abs(unl(t) ) ) * dt
        enddo
        ! Convert to force per unit mass and sum
        Fvgnlt = -integral / depth / Trep

        Fvw = Fvw + Fvgnlt

        ! save top of current section for next loop
        ahtold = aht

    enddo
    !write(*,*)'Ended momeqveg'

end subroutine momeqveg
```

Listing C.4: Subroutine `swvegnonlin` to reconstruct u_w using the wave shape model without computing `etaw` for emergence effect.

```
.....
.....
subroutine swvegnonlin(no_nodes, kwav, depth, H, g, Trep, unl)
    ! input= no_nodes, kwav, H, depth, g, Tp, unl(k,:)
    !
    ! Based on Deltares' XBeach SurfBeat' subroutine: swvegnonlin
    use snapwave_RFtable
    !
    implicit none
    !
    integer :: no_nodes, k
    integer :: irf, ih0, it0, jrf, ih1, it1
    integer , save :: nh , nt !TL: NOTE - NOT familiar with THIS_IMAGE 'save' statement, for
        now keep
    real*4 :: p ,q , f0 , f1 , f2 , f3
    real*4, save :: dh , dt
    real*4, dimension(no_nodes) :: kmr , Urs , phi , w1 , w2
    real*4, dimension(8) , save :: urf0
    real*4, dimension(50) , save :: urf2 , urf
    real*4, dimension(50 ,8), save :: cs , sn , urf1
    real*4, dimension(:), save , allocatable :: h0, t0
    real*4, dimension(no_nodes, 50),intent(out) :: unl ! NOTE - TL: we don't use 'etaw0' in
        the end?
    !
    real*4  :: pi = 4.*atan(1.0)
    real*4, intent(in) :: g
    real*4, dimension(:), intent(in) :: kwav, depth, H, Trep ! depth = the 'hh' of XBeach

    real*4, dimension(:,:,:), allocatable :: RFveg
    real*8, dimension(:), allocatable :: RFvegtmp
```

```
    !
    allocate(RFveg(11,18,20))
    !
    ! Compute net drag force due to wave skewness based on Rienecker & Fenton (1981)
    !
    write(*,*)'Started swvegnonlin'
    !
    ! Load RFtable:
    !
    call load_RFtable(RFveg)
    !
    ! Prepare interpolation of RF table
    if (.not. allocated(h0)) then
        allocate(h0(no_nodes))
        allocate(t0(no_nodes))
        dh = 0.03
        dt = 1.25
        nh = floor(0.54/ dh)
        nt = floor(25 / dt )
        do irf =1 ,8
            do jrf =1 ,50
                cs ( jrf , irf ) = cos (( jrf * 2 * pi / 50) * irf )
                sn ( jrf , irf ) = sin (( jrf * 2 * pi / 50) * irf )
            enddo
        enddo
    endif
    !
    !write(*,*)'Done with - Prepare interpolation of RF table)'
    h0 = min(nh * dh, max(dh, min(H, depth) / depth) )
    t0 = min(nt * dt, max(dt, Trep * sqrt (g / depth) ) )
    !
    ! Initialize
    urf0 = 0
    urf1 = 0
    urf2 = 0
    urf = 0
    w1 = 0
    w2 = 0
    phi = 0
    Urs = 0
    kmr = 0
    !
    ! Compute phase and weights for Ruessink wave shape
    kmr = min(max(kwav, 0.01), 100.0)
    Urs = H / (kmr * kmr * (depth **3) )
    phi = pi /2 * (1 - tanh (0.815/(Urs **0.672) ) )
    w1 = 1 - phi /( pi /2)
    w2 = 1 - w1
    !
    !write(*,*)'Done with - Compute phase and weights for Ruessink wave shape'

    ! Interpolate RF table and compute velocity profiles
    do k =1, no_nodes
        !
        ih0 = floor( h0(k) / dh)
        it0 = floor( t0(k) / dt)
        ih1 = min(ih0 + 1, nh)
        it1 = min(it0 + 1, nt)
        p = ( h0(k) - ih0 * dh) / dh
        q = ( t0(k) - it0 * dt) / dt
        f0 = (1 - p) * (1 - q)
        f1 = p * (1 - q)
        f2 = q * (1 - p)
        f3 = p * q
        !
        do irf = 1, 8
            urf0(irf) = f0 * RFveg(irf + 3, ih0, it0) + f1 * RFveg(irf + 3, ih1, it0) + f2 *
                RFveg(irf+3, ih0, it1) + f3 * RFveg(irf + 3, ih1, it1)
        enddo
        !
        do irf = 1, 8
```

```
            urf1(:, irf) = urf0(irf)
        enddo
        !
        urf1 = urf1 * (w1(k) * cs + w2(k) * sn )
        urf2 = sum(urf1, 2)
        unl(k,:) = urf2 * sqrt(g * depth(k) )
        !etaw0(k,:) = unl0 (i ,j ,:) * sqrt (max( depth(k ) ,0 ) / g ) #TL: not used in case of SnapWave
    enddo
    !
    write(*,*)'Ended swvegnonlin'

end subroutine swvegnonlin

end module snapwave_solver
```

Listing C.5: Subroutine `swvegnonlin` to reconstruct u_w using the wave shape model with computing `etaw` for emergence effect.

```
.....
.....
subroutine swvegnonlin(no_nodes, kwav, depth, H, g, Trep, unl, etaw)
    ! input= no_nodes, kwav, H, depth, g, Tp, unl(k,:)
    !
    ! Based on Deltares' XBeach SurfBeat' subroutine: swvegnonlin
    use snapwave_RFtable
    !
    implicit none
    !
    integer :: no_nodes, k
    integer :: irf, ih0, it0, jrf, ih1, it1
    integer , save :: nh , nt !TL: NOTE - NOT familiar with THIS_IMAGE 'save' statement, for now keep
    real*4 :: p ,q , f0 , f1 , f2 , f3
    real*4, save :: dh , dt
    real*4, dimension(no_nodes) :: kmr , Urs , phi , w1 , w2
    real*4, dimension(8) , save :: urf0
    real*4, dimension(50) , save :: urf2 , urf
    real*4, dimension(50 ,8), save :: cs , sn , urf1
    real*4, dimension(:), save , allocatable :: h0, t0
    real*4, dimension(no_nodes, 50),intent(out) :: unl ! NOTE - TL: we don't use 'etaw0' in the end?
    real*4, dimension(no_nodes, 50), intent(out) :: etaw   ! <--- NEW
    !
    real*4  :: pi = 4.*atan(1.0)
    real*4, intent(in) :: g
    real*4, dimension(:), intent(in) :: kwav, depth, H, Trep ! depth = the 'hh' of XBeach

    real*4, dimension(:,:,:), allocatable :: RFveg
    real*8, dimension(:), allocatable :: RFvegtmp
    !
    allocate(RFveg(11,18,20))
    !
    ! Compute net drag force due to wave skewness based on Rienecker & Fenton (1981)
    !
    write(*,*)'Started swvegnonlin'
    !
    ! Load RFtable:
    !
    call load_RFtable(RFveg)
    !
    ! Prepare interpolation of RF table
    if (.not. allocated(h0)) then
        allocate(h0(no_nodes))
        allocate(t0(no_nodes))
        dh = 0.03
        dt = 1.25
        nh = floor(0.54/ dh)
        nt = floor(25 / dt )
        do irf =1 ,8
            do jrf =1 ,50
```

```
                cs ( jrf , irf ) = cos (( jrf * 2 * pi / 50) * irf )
                sn ( jrf , irf ) = sin (( jrf * 2 * pi / 50) * irf )
            enddo
        enddo
    endif
    !
    !write(*,*)'Done with - Prepare interpolation of RF table)'
    h0 = min(nh * dh, max(dh, min(H, depth) / depth) )
    t0 = min(nt * dt, max(dt, Trep * sqrt (g / depth) ) )
    !
    ! Initialize
    urf0 = 0
    urf1 = 0
    urf2 = 0
    urf = 0
    w1 = 0
    w2 = 0
    phi = 0
    Urs = 0
    kmr = 0
    !
    ! Compute phase and weights for Ruessink wave shape
    kmr = min(max(kwav, 0.01), 100.0)
    Urs = H / (kmr * kmr * (depth **3) )
    phi = pi /2 * (1 - tanh (0.815/(Urs **0.672) ) )
    w1 = 1 - phi /( pi /2)
    w2 = 1 - w1
    !
    !write(*,*)'Done with - Compute phase and weights for Ruessink wave shape'

    ! Interpolate RF table and compute velocity profiles
    do k =1, no_nodes
        !
        ih0 = floor( h0(k) / dh)
        it0 = floor( t0(k) / dt)
        ih1 = min(ih0 + 1, nh)
        it1 = min(it0 + 1, nt)
        p = ( h0(k) - ih0 * dh) / dh
        q = ( t0(k) - it0 * dt) / dt
        f0 = (1 - p) * (1 - q)
        f1 = p * (1 - q)
        f2 = q * (1 - p)
        f3 = p * q
        !
        do irf = 1, 8
            urf0(irf) = f0 * RFveg(irf + 3, ih0, it0) + f1 * RFveg(irf + 3, ih1, it0) + f2 *
                RFveg(irf+3, ih0, it1) + f3 * RFveg(irf + 3, ih1, it1)
        enddo
        !
        do irf = 1, 8
            urf1(:, irf) = urf0(irf)
        enddo
        !
        urf1 = urf1 * (w1(k) * cs + w2(k) * sn )
        urf2 = sum(urf1, 2)
        unl(k,:) = urf2 * sqrt(g * depth(k) )
        etaw(k,:) = unl (k,:) * sqrt (max( depth(k ), 0.0 ) / g ) !<--- NEW: free-surface
            oscillation [m]
    enddo
    !
    write(*,*)'Ended swvegnonlin'

end subroutine swvegnonlin
```

D

Supplementary results

This appendix compiles (i) per–scenario cross-shore comparisons and (ii) statistical performance skill plots for the vegetated cases. Figure D.1 shows the full set of six scenario pairs (S1–S12) for significant wave height and mean water level, including the `SFINCS-SnapWave` baseline, the improved model with $F_{v,w}$, and the improved model including the emergence effect. Figure D.2 summarizes performance against the laboratory gauges over all vegetated scenarios, with 1:1 reference lines and legends reporting the scatter index and bias for each model configuration.

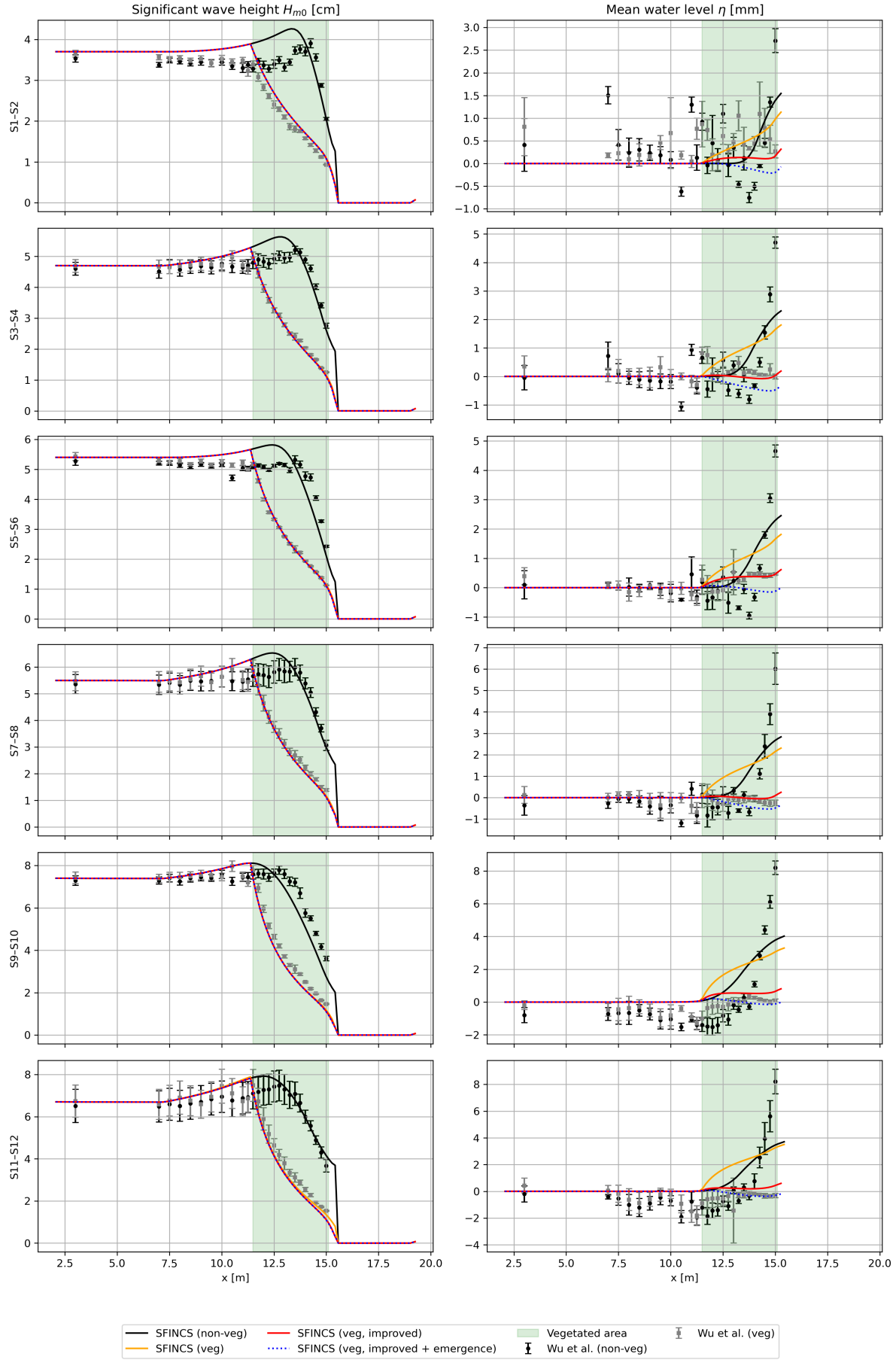

Figure D.1: Cross-shore evolution for all six scenario pairs (rows: S1–S2, S3–S4, S5–S6, S7–S8, S9–S10, S11–S12). Left column: significant wave height H_{m0} [cm]; right column: mean water level η [mm]. Lines: `SFINCS-SnapWave` non-vegetated (black), vegetated baseline (orange), vegetated improved with $F_w + F_{v,w}$ (red), and vegetated improved with emergence (blue, dotted). Symbols: Wu et al. (2011) non-vegetated (black circles) and vegetated (grey squares). The vegetated zone is shaded green.

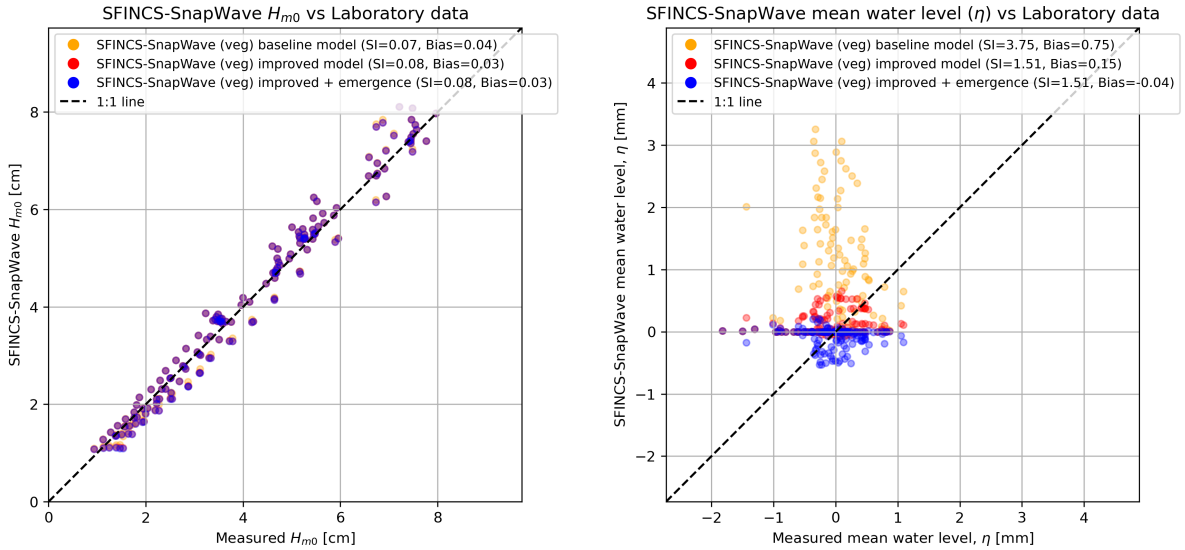

Figure D.2: Model skill for vegetated scenarios (S2, S4, S6, S8, S10, S12). Left: H_{m0} [cm]; right: mean water level η [mm]. Colors: baseline vegetated model (orange), improved $F_w+F_{v,w}$ (red), and improved $F_w+F_{v,w}$ with emergence (blue). The dashed line is the 1:1 reference; legends report the scatter index (SI) and bias for each series.

E

Model application

After evaluating and improving the performance of `SFINCS-SnapWave` in capturing more accurate water levels with vegetation presence, the model simulation can be conducted to further explore the influence of mangroves on total water levels due to the combination of waves and storm surges forcing. In this section, the potential application of the model is presented. Here, the global hydrodynamic data used is the one that was presented in Chapter 2.

E.1. Global data and model applicability

Global datasets allow us to identify where such events are most likely to occur, as presented in Chapter 2, and could be useful to develop representative simulation scenarios. Using consistent large-scale datasets ensures that simulations are grounded in physically realistic conditions and globally applicable. This section demonstrates the applicability of global data in developing a simulation framework model that can be used to examine the role of mangrove in storm surge-wave combined forcing.

Hydrodynamic global data processing

The hydrodynamic dataset used for this study refers to the updated version of offshore hydrodynamic input at mangrove coasts corresponding to van Zelst et al. (2021). The dataset consists of offshore significant wave height (H_s) and its peak periods (T_p), as well as the extreme water level above Mean Sea Level (MSL) resulting from the combination of storm surge and tide (storm tide) for corresponding nine return periods (2, 5, 10, 25, 100, 250, 500, 1000 years). This dataset originates from ERA-Interim offshore wave data and the Global Tide and Surge Reanalysis (GTSR). The return period that will be used for the data processing will be 100 years for all datasets, to balance the physical relevance and capture impactful extreme events such as tropical cyclones.

Due to the known limitations of the GTSR dataset in representing tropical cyclone-induced extremes (Sanne Muis et al. 2016), we adopt an improved dataset for the storm tide. COAST-RP (Coastal Dataset of Storm Tide Return Periods) values are used for the storm tide data, which better reflect the impact in tropical cyclone regions (Dullaart, S. Muis, Bloemendaal, et al. 2021). Furthermore, COAST-HG (Coastal Dataset of Storm Tide Hydrographs) are used for extracting the duration of the storm surge (Dullaart, S. Muis, Moel, et al. 2023). Table E.1 shows the summary of the variables and corresponding data source that will be used, and Figure E.1 illustrates the data processing flowchart.

Transect selection

Our primary dataset, although already specific to global mangrove regions, comprises a large number of transects (63926 transects). In order to better represent our modelling setup approach and our study interest in compound flooding, the dataset is filtered by selecting only the representative transects. There are two steps of the transect filtering: based on the mangrove typology and based on the wave-surge extreme dependency.

First, the dataset is filtered by the global mangrove biophysical typology, using the global data by Worthington et al. (2020). The data comprises the class of global typology of mangroves, such as open

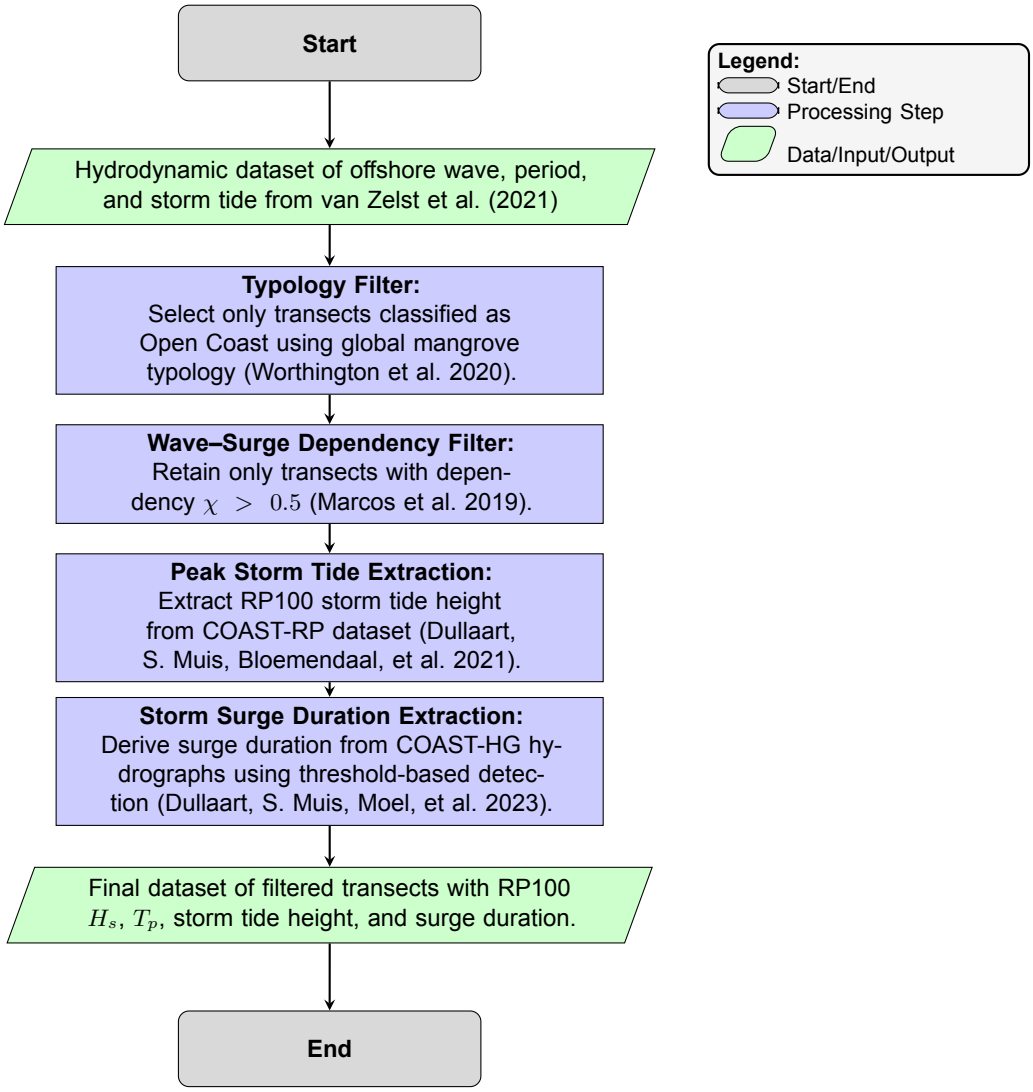

Figure E.1: Workflow diagram showing the data processing steps from global hydrodynamic datasets to the final filtered transects used in this study.

coast, delta, estuary, and lagoon. In this study, our primary dataset will be filtered to select only the open coast typology, allowing our 1D modelling setup to be better represented. The other typologies are expected to have big alterations of offshore hydrodynamic data due to their local condition (topography, bathymetry, sheltered area), which makes it more challenging to find the representative values. In this first filter, the dataset transect number was reduced to 9439 transects. The reduction in transect number results from a conservative filter that retains only transects directly intersecting ”OpenCoast” polygons, ensuring accurate classification and consistent typology for reliable analysis.

Second, the dataset is further filtered based on the dependency between waves and storm surge extremes, which indicates a higher likelihood of wave-surge compound flooding happening in the region. Marcos et al. (2019) provides global data on the dependency between waves and storm surges that is quantified by χ, a metric indicating the strength of dependence. χ values range from 0 to 1, with values closer to 1 indicating higher dependency (stronger likelihood of occurrence). In this study, a value of χ greater than 0.5 will be our threshold for representing their dependence. A threshold of $\chi > 0.5$ implies that there is at least a 50% chance that an extreme in one variable (e.g., storm surge) is accompanied by an extreme in the other (e.g., wave height), which is a meaningful indicator of compound flood risk. Figure 2.2 illustrates the result of the transect filtering process.

Variable	Description	Data Source
Significant wave height and peak period (H_s, T_p)	Offshore significant wave height and peak period for various return periods	ERA-Interim (processed by van Zelst et al., 2021)
Storm tide height	Extreme water level above MSL due to tide + surge at return period 100 years	COAST-RP (Dullaart, S. Muis, Bloemendaal, et al. 2021)
Storm tide duration	Duration of elevated water level above threshold around storm event	COAST-HG (Dullaart, S. Muis, Moel, et al. 2023)

Table E.1: Summary of hydrodynamic variables and their data sources

Storm tide data extraction

The COAST-RP (Dullaart, S. Muis, Bloemendaal, et al. 2021) and COAST-HG (Dullaart, S. Muis, Moel, et al. 2023) datasets are used to obtain the storm tide peak and duration data for all filtered transects. The peak water levels are taken from the COAST-RP dataset using the 100-year return period. To determine the duration, the average storm tide time series from COAST-HG is analysed by identifying when the water level rises above (upward crossing) and falls below (downward crossing) a threshold, which is based on the peak of the tide reference. Figure E.2 shows examples of the extracted storm tide durations for three representative transects.

Final datasets

After the full filtering process, the final dataset consists of representative transects located along open coasts with high wave–surge dependency ($\chi > 0.5$). For each transect, key hydrodynamic variables with a return period of 100 years are extracted: the significant wave height (H_s), peak wave period (T_p), storm tide height, and storm surge duration. These parameters form the basis for scenario generation in the next modelling simulation.

Figure E.3 shows the distribution of each variable across all selected transects, visualised using smoothed density estimates (KDE) and histograms. These distributions show the variability of forcing conditions globally in the filtered areas.

Simulations

Using the final datasets of filtered global hydrodynamic data in the mangrove environment, the simulation scenarios enable targeted simulations to explore how mangroves can mitigate extreme water levels in realistic wave-surge events. It includes wave-only scenarios varying bed slope and vegetation extent, surge-only scenarios varying surge height, duration, and vegetation extent, and combined wave-surge scenarios adjusting both surge and vegetation extent. Water level is evaluated behind the mangrove regions. Other parameter selections, such as bed slopes, mangrove width, and vegetation characteristics, can be found in Chapter 2. Figure E.4 illustrates the model setup to be applied in this proposed simulation. A detailed explanation of the scenarios is provided in the next section.

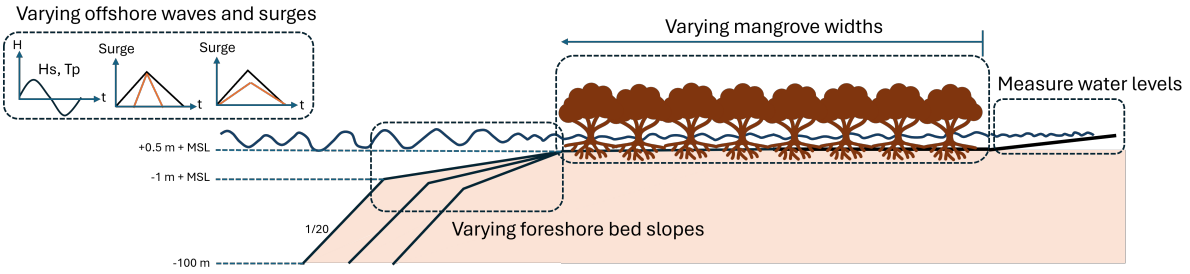

Figure E.4: Illustration of the model setup for simulation scenarios. Inspired by van Wesenbeeck, van Zelst, et al. (2025) study.

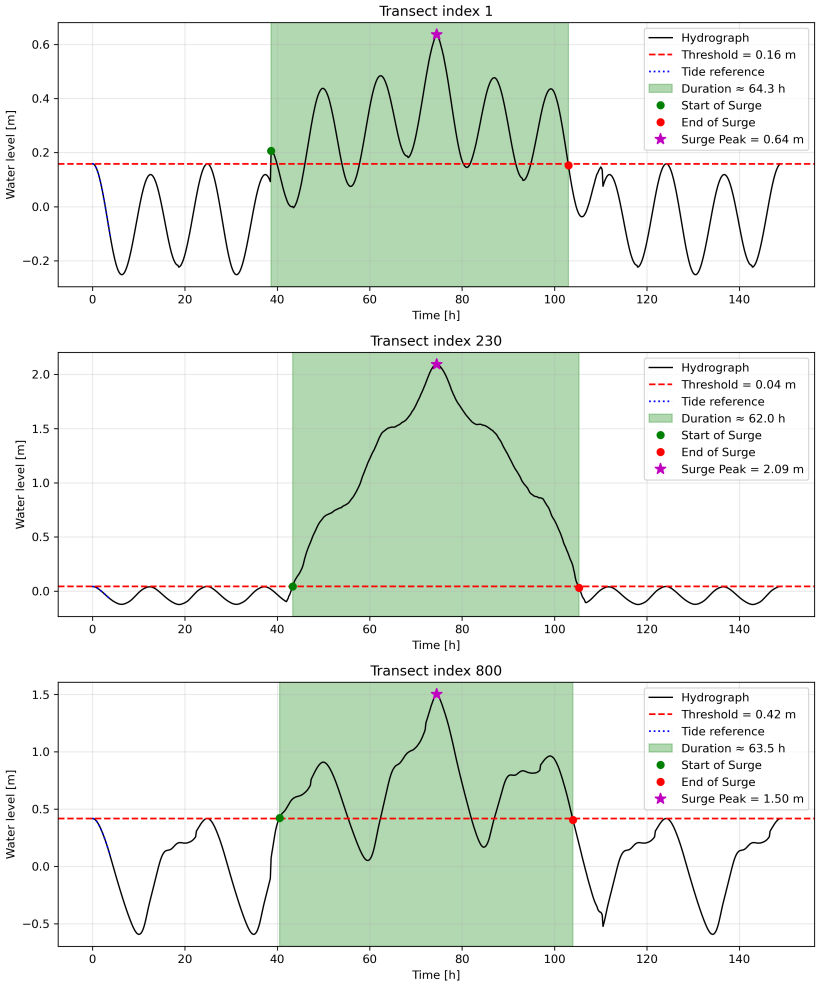

Figure E.2: Example hydrographs illustrating the extraction of storm tide characteristics at three representative transects. The coloured window highlights the surge duration (green shading), while the magenta star marks the surge peak and the dashed red line denotes the tide-based threshold used for detection.

E.2. Scenarios

To investigate the influence of mangrove presence on total water levels under the combined effects of waves and storm tide, a series of one-dimensional simulation scenarios is developed. These scenarios are grouped into five series. The first four series isolate the effects of waves and storm tide separately, while the fifth series explores their combined impact.

E.2.1. Series 1: Variation of wave heights (wave-only)

In this series, the influence of mangroves on wave setup (which contributes to total water levels) is assessed by varying the wave heights (H_s) and their peak periods (T_p), along with the mangrove width. This series aims to investigate the sensitivity of various wave characteristics to different mangrove extents. To represent realistic wave conditions, the offshore hydrodynamic dataset processed in the previous section is used. The K-means clustering method is applied to the H_s and T_p values to identify five representative wave conditions, with the cluster centroids selected as input scenarios. Figure E.5 shows the scatter plot of significant wave height (H_s) and peak wave period (T_p) from the processed dataset. On the other hand, the mangrove characteristics will be decided based on literature data from Chapter 2. To explore the effect of mangrove width, five uniform values are chosen: 0, 100, 250, 400, and 500 meters.

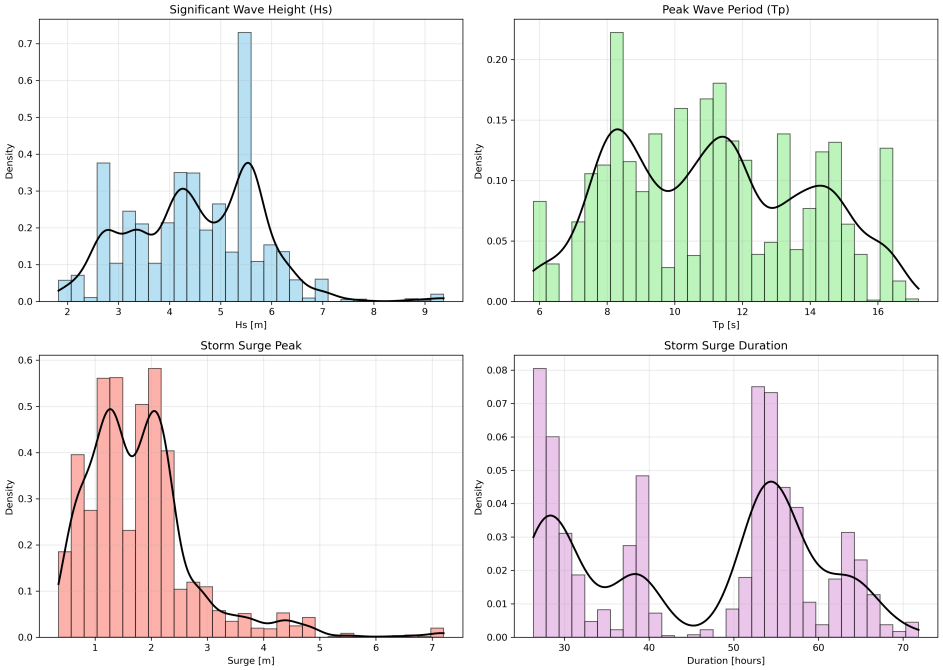

Figure E.3: Distribution of final dataset variables across all filtered transects. Each panel shows the kernel density estimate (KDE) and histogram for: (a) significant wave height (H_s), (b) peak wave period (T_p), (c) storm tide height, and (d) storm surge duration.

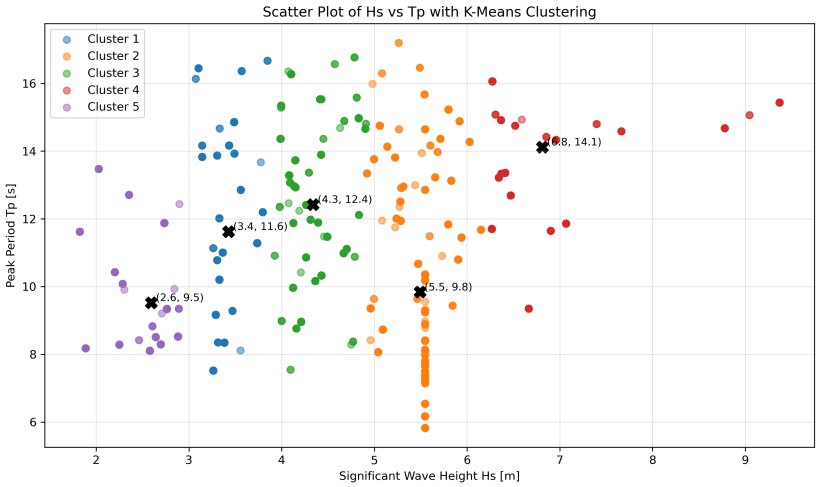

Figure E.5: Scatter plot of H_s vs. T_p from the processed dataset. The black x markers denote the five selected centroids based on K-means clustering, representing the most representative wave conditions for scenario design.

To provide a conceptual overview of the expected results, Table E.2 presents an expectation matrix based on the combination of five wave conditions and five mangrove widths. The highest wave setup is expected for the largest waves without mangroves, while the lowest setup is expected for the smallest waves combined with the widest mangrove extent.

Table E.2: Expectation matrix for Series 1 scenarios. The highest wave setup is expected for the largest waves and no mangroves, while the lowest setup is expected for the smallest waves and the widest mangroves.

Wave ↓		**Mangrove width [m] →**				
H_s **[m]**	T_p **[s]**	**0**	**100**	**250**	**400**	**500**
6.8	14.1	**Highest**				
5.5	9.8					
4.3	12.4					
3.4	11.6					
2.6	9.5					**Lowest**

E.2.2. Series 2: Variation of bed slopes (wave-only)

This series investigates the influence of bed slope steepness on wave setup across different mangrove extents. By varying both the bed slope and mangrove width, the scenarios aim to explore how the interaction between topography and vegetation affects wave attenuation. Five representative bed slopes ranging from steep (1/100) to gentle (1/1000) are selected based on values found in Chapter 2, along with uniform mangrove widths of 0, 100, 250, 400, and 500 meters. The wave characteristics imposed in this series are fixed to $H_S = 5.5$ meters and $T_p = 9.8$ seconds (corresponding to one of the representative clusters in Series 1).

The expected outcomes are summarised in Table E.3, where the steepest slope without mangroves is expected to produce the highest setup, and the gentlest slope with the widest mangroves is expected to yield the lowest.

Table E.3: Expectation matrix for Series 2 scenarios. The steepest bed slope with no mangroves is expected to give the highest wave setup, while the gentlest slope with the widest mangrove belt should yield the lowest setup.

Bed slopes ↓	**Mangrove width [m] →**				
	0	**100**	**250**	**400**	**500**
1/100	**Highest**				
1/250					
1/500					
1/750					
1/1000					**Lowest**

E.2.3. Series 3: Variation of storm-tide peak amplitude (storm-tide-only)

This series isolates the effect of storm-tide peak height on wave setup while keeping the surge duration constant at 40 h. Five representative surge peaks (1, 2, 3, 4, 5 m) are chosen from the global dataset by applying K-means clustering to events within the fixed-duration window. Figure E.6 shows the distribution of surge peaks versus duration, with the selected centroids marked by black x symbols. Each peak height is then combined with five mangrove widths (0–500 m) to quantify attenuation across a realistic range of vegetated foreshores. The qualitative expectations are summarised in Table E.4.

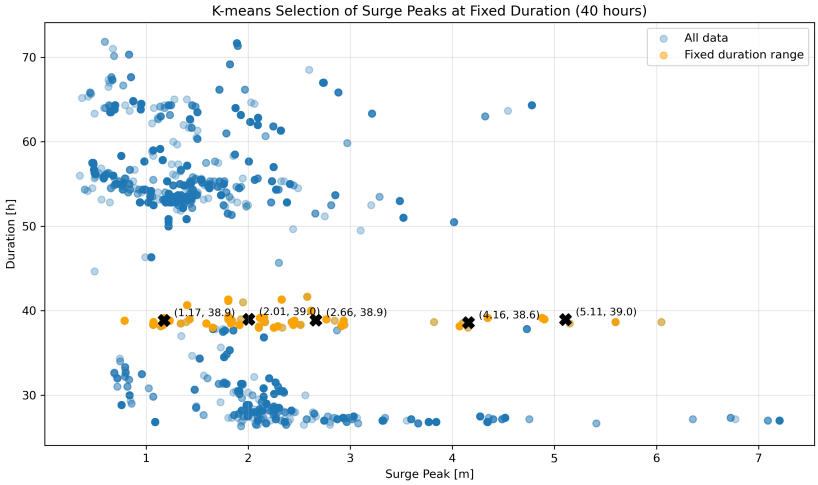

Figure E.6: Scatter plot of surge peak versus duration (40 ± 2 h window). Black x markers denote the five representative surge peaks selected with K-means clustering.

Table E.4: Expectation matrix for Series 3. The largest surge peak with no mangroves is expected to give the **highest** setup, whereas the smallest peak with the widest mangrove belt should give the **lowest**.

Surge peak [m] ↓	**Mangrove width [m]** →				
	0	**100**	**250**	**400**	**500**
5.0	**Highest**				
4.0					
3.0					
2.0					
1.0					**Lowest**

E.2.4. Series 4: Variation of storm duration (storm tide-only)

This series explores how the duration of a storm surge affects wave setup, under the assumption of a fixed surge peak height. A constant surge amplitude of 2 m is used, and five representative surge durations (30, 35, 40, 55, and 60 hours) are selected from the global dataset using K-means clustering. Figure E.7 shows the selection process in a scatter plot of surge peak versus duration, where the black x markers indicate the chosen centroids. The effect of varying mangrove widths (0 to 500 meters) is also examined in combination with the different durations. Table E.5 summarises the expected influence on wave setup.

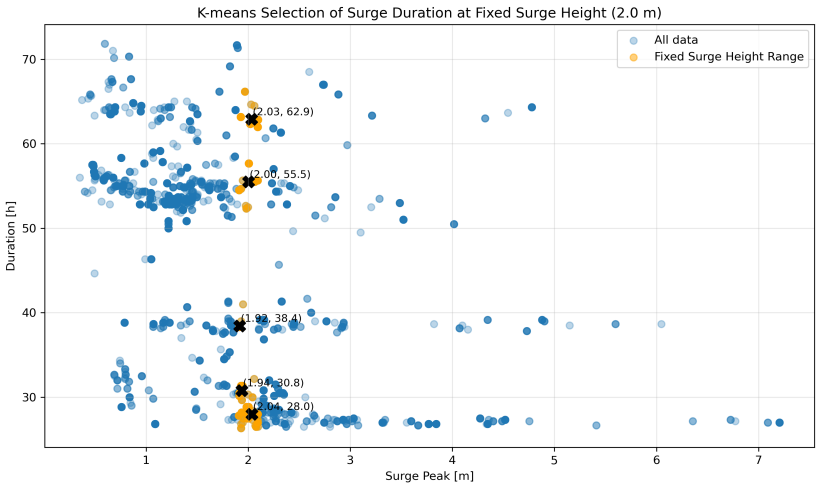

Figure E.7: Scatter plot of storm duration versus surge height for fixed surge amplitude (2 m). Black x markers indicate five representative durations selected using K-means clustering.

Table E.5: Expectation matrix for Series 4 scenarios. Highest setup is expected for the longest surge with no mangroves, while the lowest setup is expected for the shortest surge with the widest mangroves.

Duration [h] ↓	**Mangrove width [m]** →				
	0	**100**	**250**	**400**	**500**
60	**Highest**				
55					
40					
35					
30					**Lowest**

E.2.5. Series 5: Combined variation of surge peak and wave heights

This series investigates the combined effect of storm surge and wave forcing on wave setup, as well as the mitigating role of mangroves under compound conditions. The wave conditions are fixed at $H_s = 5.5$ m and $T_p = 9.8$ s, while the surge duration is kept constant at 40 hours. The main variable of interest is the relative intensity of the surge compared to the wave height, represented as the surge-to-wave ratio (Surge$/H_s$). Five representative values (0, 0.25, 0.5, 0.75, and 1.0) are selected based on the global dataset around a fixed wave height ($H_s \approx 5.0$ m). Figure E.8 shows the scatter plot of the surge-to-wave ratio and the range of the values. The expected outcome pattern is summarised in Table E.6.

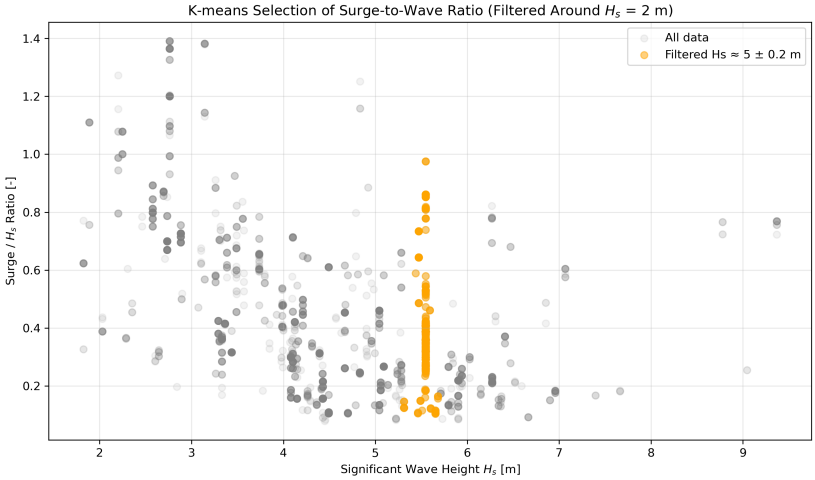

Figure E.8: Scatter plot of Surge$/H_s$ values for $H_s \approx 5.0 \pm 0.2$ m.

Table E.6: Expectation matrix for Series 5 scenarios. Highest setup is expected for the largest surge-to-wave ratio with no mangroves, while the lowest setup is expected for the smallest surge-to-wave ratio with the widest mangroves.

Surge/H_s ↓	**Mangrove width [m] →**				
	0	**100**	**250**	**400**	**500**
1.0	**Highest**				
0.75					
0.50					
0.25					
0.0					**Lowest**